Energetic Particle Generation in Ultra-Intense Laser-Plasma Interactions

Hideaki Habara

February 3, 2000

preface

This thesis is submitted for the degree of Ph.D. at Osaka University. The research was conducted at the Institute of Laser Engineering(ILE) in the associate course of science faculty in graduate school, Osaka University. The objective of this thesis is study of energetic particle generation in ultra-intense laser plasma interactions.

Three categories are emphasized through experiments.

(1) Generation of short pulse ultra-intense laser light with a chirped pulse amplification (CPA) technique using a glass laser.

(2) Heating property with high density energetic electrons in ultra-intense laser-plasma interactions.

(3) Generation of high density energetic ions in ultra-intense laser-plasma interactions.

This thesis is composed of 8 chapters.

Chapter 1 describes the background and the objective of this research.

Chapter 2 presents the generation of the short pulse ultra-intense laser light. A 40 TW peak power laser is developed using the Ti:Sapphire laser coupled with Nd:glass amplifiers in the CPA technique.

Chapter 3 shows compressed pulse shaping with an incident spectrum control. The spectral controls are applied for prepulse generation, pedestal reduction and pulse width shortening in the compressed pulse.

Chapter 4 describes about the heating of a solid with high density energetic electrons generated in ultra-intense laser-plasma interactions.

Chapter 5 is heating of a compressed plasmas by the long pulse laser with high density energetic electrons in ultra-intense laser-plasma interactions.

Chapter 6 shows generation of high density energetic ions in ultra-intense laser-plasma interactions with neutron spectroscopy.

Chapter 7 describes about generation of unstable nucleus resulting from a Li-D and B-D fusion reaction in ultra-intense laser-plasma interactions.

Chapter 8 is summary of the research.

Contents

1 Introduction **7**

2 Development of Ultra-Intense Laser **13**
2.1 Introduction . . . 13
2.1.1 Chirped pulse amplification (CPA) method . . . 13
2.2 Development of short pulse ultra intense laser . . . 14
2.3 Frontend system . . . 18
2.3.1 Ti:sapphire oscillator . . . 18
2.3.2 Pulse stretcher . . . 19
2.3.3 Regenerative amplifier . . . 23
2.4 Glass amplifier . . . 24
2.4.1 GMII glass amplifier . . . 25
2.4.2 Laser amplification for the chirp pulse . . . 25
2.4.3 Gain narrowing in the glass amplifier . . . 26
2.4.4 Self phase modulation . . . 27
2.5 Pulse compression . . . 30
2.5.1 Estimating mismatch between grating pair . . . 30
2.5.2 The compressed pulse shape in pulse compressor . . . 31
2.6 Laser focusing . . . 31
2.7 Summary . . . 34

3 Pulse Shaping with Spectral Control **37**
3.1 Introduction . . . 37
3.2 Pulse shaping in a CPA method with glass amplifiers . . . 38
3.3 Experiments for pulse shaping . . . 38
3.4 Prepulse control . . . 39
3.5 Pedestal control . . . 43
3.6 Shortening of the pulse duration . . . 46
3.7 Summary . . . 52

4 Solid-dense plasma heating by high energy density electrons **55**
4.1 Introduction . . . 55
4.2 Plasma heating by the fast electrons . . . 56
4.2.1 Experiment setup . . . 56
4.2.2 Experimental results . . . 58

4.3 Propagation of fast electrons in dense plasmas 61
4.4 Summary 64

5 Compressed Plasma Heating by High Energy Electrons 67
5.1 Introduction 67
5.2 Guided conical compression of plasma 67
5.3 Compressed plasma heating 69
5.4 Summary 74

6 Neutron Spectroscopy for Ion Acceleration Mechanism 77
6.1 Introduction 77
6.2 Ion acceleration mechanism 77
6.3 3D monte-carlo simulation 78
6.4 Experiment 79
6.5 Laser Polarization dependence 81
6.6 Laser Intensity dependence 87
6.7 Prepulse Level dependence 89
6.8 Summary 92

7 Nuclear Physics in ultra intense laser interactions 95
7.1 Introduction 95
7.2 Nuclear fusion reaction using Li and B 95
7.2.1 Experiment 96
7.3 Generation of Perfectly-Ionization unstable EC nuclei 97
7.4 Summary 98

8 Summary 101

A Fast Ignitor 103

B Electron acceleration in ultra-intense laser-plasma interactions 107
B.1 Electron acceleration mechanism 107
B.2 Electron acceleration direction 108

Chapter 1

Introduction

Laser, which is one of the most grateful inventions in 20th century, has been giving a great deal of contributions on science and technology with the laser progress. The first successful laser action was achieved in 1960 by Maiman [1], using a crystal of ruby as a laser material. The power during the output pulse was nearly 10kW, which was million times larger than that of the sunlight at the earth's surface. The laser power has been increased in the laser progress to enhance the laser energy and to reduce the pulse duration. In the laser energy, Nd:glass lasers which are used as a driving force in inertial confinement fusion (ICF) research enable a high energy laser (∼100kJ), corresponding to TW ($10^{12}W$) level, in a master oscillator power amplifier (MOPA) system [2]. Now the laser system based on these technology and delivering an overall output energy of ∼1MJ are built in the United States (National Ignition Facility (NIF), Livermore) or in France (Megajoule project, Limeil).

On the other hand, the pulse duration has been shortened with an improvement of mode locking and Q-switching method. The continuously pumped mode-locked dye-lasers developed in early 1970s made possible the production of sub-picosecond pulses for the first time. In 1981, the first production of optical pulses briefer than 100 fs with a newly developed colliding-pulse ring dye laser. Furthermore, recent progress of a new solid laser utilizing "Kerr-lens mode locking" [3, 4] such as Ti:sapphire enables an ultra short pulse in less than ten fs (down to 10^{-14}s) [5].

Coupling these technologies, chirped pulse amplification (CPA) method [6] designed in 1985 enables to generate efficiently ultra highly peak power over TW (10^{12}W) [7, 8] by stretching a pulse temporally and later recompressing the amplified pulse. At the laser intensity over 10^{19}W/cm^2 by focusing to be several μm spot, the electric field can be over 8.6×10^{12}V/m, which become larger than the Coulomb field that binds atomic electrons in Bohr radius. Other feature of CPA laser is the high energy density and resulting highly light pressure of the pulse. The energy density of the pulse is over 3×10^9J/cm^3, corresponding to a 3.1keV (∼4×10^7K) blackbody and an equivalent light pressure of 3×10^9atm at the intensity of 10^{19}W/cm^2.

These ultra-intense lasers have been giving strongly influence on study for laser-plasma interactions. Figure 1.1 [7] shows electron quiver energy and accessible phenomena as a function of laser intensities. At the laser intensities over 10^{18}W/cm^2, Lorentz factor γ ($=1/\sqrt{1-v_e^2/c^2}$) becomes over 2 in MeV range of the quiver energy, resulting in not negligible in relativistic effect in plasmas. Furthermore, the phenomena of QED such as

a pair-production will become important in the laser absorption for plasmas at the laser intensities over 10^{20}W/cm^2.

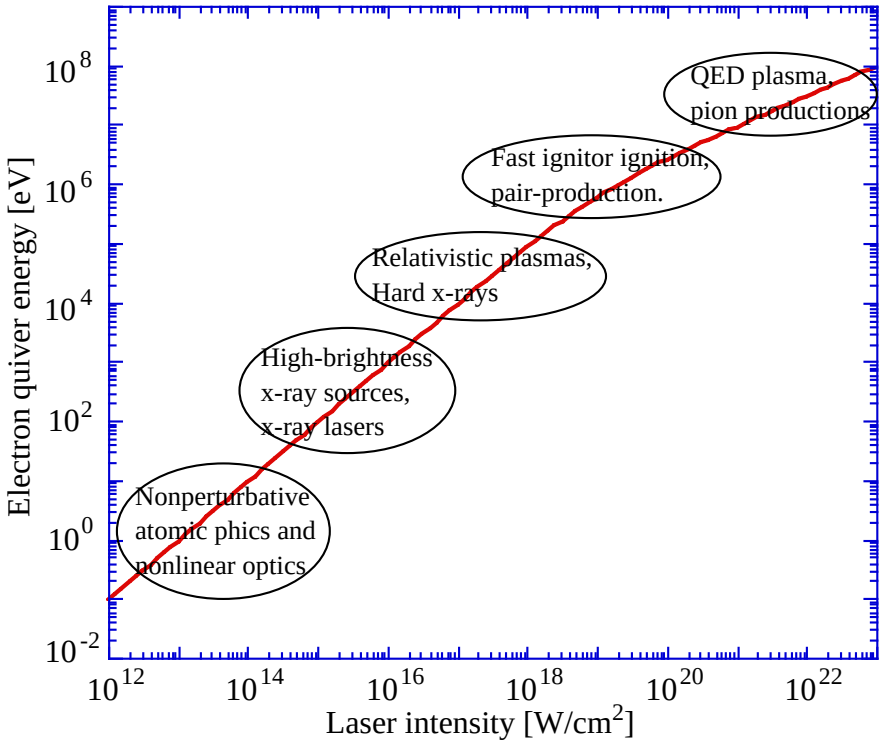

Figure 1.1: Electron quiver energy and accessible phenomena as a function of laser intensities.

In interactions of these ultra-intense lasers with plasmas, the strong field will accelerate electrons and ions in plasmas to MeV range [9, 10] with highly density. If the density is near solid density, the particle numbers per second are over 10^{26}, which are enormous larger than that of synchrotron ($\sim 10^{13}$) or linear accelerator ($\sim 10^{15}$). However, acceleration mechanisms and current densities of the particles are not clear. In addition, a propagation of the high energy density particles and its interactions in plasmas have not been understood yet.

Study of generation and transport of the high energy density particles can also contribute not only to understand ultra-intense laser-plasma interactions but also to apply for various field, for example, nuclear physics, atomic physics and astrophysics. Furthermore, short pulse and high brightness hard X-rays and γ rays generated by the energetic particles are also expected to apply for radiation chemistry, biology, medicine and so on.

Fast ignitor scheme in ICF research is also one of the great applications of the high-density energy electrons and ions with ultra-intense laser lights. The detail of fast ignitor scheme is described in appendix A. In this scheme, the high density energetic particles heat up and ignite a high-density fuel core plasma instantaneously. Generation of the high density energy particle and its transport are significantly important for the fast ignitor.

From this viewpoint, I have studied generation of energetic particles and their transport

in ultra-intense laser-plasma interactions.

In the second chapter, I described a development of a CPA ultra-intense short pulse laser system to obtain an ultra-intense laser field. Self-phase modulation of the intense laser light in laser optics and influence of discrepancy from the ideal condition at the pulse compressor on the focused laser intensity are estimated.

The third chapter is mentioned about compressed pulse shaping with spectral control in the system. A prepulse control, a pedestal reduction and a shortening of the pulse duration in the compressed pulse were demonstrated by the spectral control utilizing a spectral dispersion in a pulse stretcher.

The forth chapter shows a highly density fast electron generation and its heating in a solid density plasma in ultra-intense laser plasma interactions. The heating property of plasma with the high-density hot electrons is influenced by an absorption mechanism, indicating that the density of hot electrons nonlinearly change the heating process.

The fifth chapter shows the first demonstration of a highly compressed plasma heating by hot electrons. High-density hot electrons generated by short-pulse intense laser heat the compressed plasma generated by high-energy long pulse laser light in a conical shape target.

The sixth chapter describes the ion acceleration mechanism in ultra-intense laser-plasma interactions. Ion distributions in a solid target were measured with neutron spectroscopy changing the laser polarization, the intensity and the prepulse level. All the results, which were compared with 2-dimensional particle-in-cell simulations, indicated the ions are accelerated by an electrostatic field generated by a charge displacement between ions and electrons toward the rear target normal.

The seventh chapter shows one of the applications for the energetic ions generated in ultra-intense laser plasma interactions. A generation of unstable nucleus in D-Li or D-B nuclear fusion reaction was demonstrated with neutron spectroscopy.

The last is conclusion and summery of this thesis.

Reference

[1] T. H. Maiman, Nature **187**, 493 (1960).

[2] W. Koechner, *Solid-State Laser Engineering*, 4th ed. (Springer, Berlin, 1996), Chap. 4.

[3] *Ultrafast phenomena VII:proceedings of the International Conference*, (Springer-Verlag, New York), 75 (1990).

[4] D. E. Spence, P. N. Kean and W. Sibbett, Opt. Lett. **16**, 42 (1991).

[5] J. Zhou et al., Opt. Lett. **19**, 1149 (1994).

[6] D. Strickland and G. Mourou, Opt. Comm. **56**, 219 (1985).

[7] M. D. Perry and G. Mourou, science **264**, 917 (1994).

[8] B. C. Stuart, M. D. Perry, J. Miller, G. Tietbohl, S. Herman, J. A. Britten, C. Brown, D. Pennington, V. Yanovsky, and K. Wharton, Opt. Lett. **22**, 242 (1997).

[9] G. Malka and J. L. Miquel, Phys. Rev. Lett. **77**, 75 (1996).

[10] A. P. Fews, P. A. Norreys, F. N. Beg, A. R. Bell, A. E. Dangor, C. N. Danson, P. Lee and S. J. Rose, Phys. Rev. Lett. **73**, 1801 (1994).

Chapter 2

Development of Ultra-Intense Laser

2.1 Introduction

Chirped pulse amplification (CPA) [1] method in laser technology enables to increase an output laser power. The peak power is now easily achieved to be over TW (10^{12} Watt) with pulse duration of less 1ps. Before the development of the CPA method, glass laser was widely used as a high power laser (e.g. 1kJ/1ns/1TW). However, the laser power of these conventional systems was limited by saturation in the laser amplification and a damage on the optical component such as amplifier glasses and optical windows. The CPA method overcomes this limitation to increase the power with reduction of the energy density of the pulse by stretching the pulse duration in the amplifications.

The first CPA technique was applied to a large-scale, high energy Nd:glass system and generated efficiently ultra highly peak power such a TW level [1]. The recent progress of a solid state lasers such as Ti:sapphire laser with Kerr-lens mode locking method [2, 3] has realized the peak power over 100TW [4] coupled with glass laser system. Furthermore, PW (10^{15} Watt) output lasers plan to construct around the world. These high power CPA laser are expected to give a great deal of contributions on various fields of science, such as plasma physics, laboratory astrophysics and so on. These intense laser lights are also important from the viewpoint of a high-energy particle source in ultra-intense laser-plasma interactions.

In order to study generation of high-density energetic particles, I developed a short pulse ultra intense laser with CPA technique using Nd:glass amplifiers coupled with a Ti:sapphire oscillator. In this chapter, I describe the development of this CPA laser to obtain a focal intensity of 10^{19}W/cm^2, corresponding to an electron quiver energy of MeV range oscillated by the laser electric field in plasmas.

2.1.1 Chirped pulse amplification (CPA) method

Pulse duration of laser light is determined by a spectral width of the pulse under the Fourier-transform limitation. Therefore, to obtain a shorter pulse duration requires the broader spectral width. In the CPA method as shown in Fig.2.1, a fourier-limited ultra-short pulse from an oscillator is temporally stretched (chirping) in a pulse stretcher. The peak power and the energy density of the chirped pulse become lower than that of the

original pulse, resulting to avoid a damage to the laser optics and enable to amplify the pulse at higher energy up to the damage threshold of the optics. Finally, an ultra intense pulse can be obtained by temporal compression of the amplified pulse to be fourier-limit compensating the chirp in a pulse compressor.

At the beginning stage of the CPA history, the chirped pulse was obtained by a single-mode optical fiber using a sub-ns modelock Nd:YLF or Nd:YAG oscillator [5] to broaden the spectral width. However, the chirp from optical fiber is nonlinear and the pulse compression can't perfectly compensate the chirp with a grating pair, resulting in generation of a pedestal before and after the main pulse. This pedestal creates pre-formed plasma at a target surface before arrival of the main pulse. Laser-plasma interactions will be changed with a volume or a shape of the pre-formed plasma.

A new method improving the defect was proposed to stretch a sub-ps glass laser light temporally to ns-order using a grating pair. The grating pair enables to generate the linear chirp and to compensate the chirp easily in compressor gratings. For example, 35TW peak intensity was obtained [6] using 600 fs light from Nd:LMA laser coupled with additive modelock method [7] as a sup-ps light oscillator.

Recent progress of a solid state laser with Kerr-lens mode locking method, such as Ti:sapphire laser, has realized broadband ultra short pulse laser, typically less than a tens fs [8, 9]. Ti:sapphire laser is superior in the point of stability, highly repetition rate, average power, and broadband gain cross section and variable oscillation wavelength, compared with typical broadband laser such as dye- or excimer-laser. CPA laser coupled with the new solid laser now becomes a mainstream of the ultra-intense short-pulse laser and its power will be reached over PW.

2.2 Development of short pulse ultra intense laser

I developed an ultra-intense CPA short-pulse laser using Nd:glass amplifiers coupled with Ti:sapphire frontend system to obtain an intensities over 10^{19}W/cm^2. Figure 2.2 shows a diagram of the CPA laser system.

In this system, the Ti:sapphire oscillator generates an ultra short pulse which energy is about nJ. This pulse is stretched temporally to 1000 times longer in the pulse stretcher. The chirped pulse is amplified in the Ti:sapphire regenerative amplifier and the Nd:glass amplifiers to 20J. Finally, the pulse is compressed to Fourier limit with a grating pair in the pulse compressor equivalent to the 40TW peak power. Focusing the high power laser to be $20\mu m$ diameter, the focal intensities over 10^{19}W/cm^2 can be obtained at the focal point. Figure 2.3 shows a constitution of the CPA laser system.

This system is consisted of (a) Ti:sapphire oscillator, (b) pulse stretcher, (c) Ti:sapphire regenerative amplifier, (d) Nd:glass amplifier, (e) 4 gratings pulse compressor, and (f) f/3 off-axis parabolic focal mirror. The Nd:glass amplifiers in GEKKO-Module II (GMII) system at Institute of Laser Engineering (ILE) is consisted of spatial filter, rod amplifier, disk amplifier, faraday rotator and optical shutter. The GMII glass amplifier system has three arms; X-, Y- and Z-chain. In the system, X- and Y-chain are used for the chirp pulse amplification. For a convenience, I described about the system divided by four sections: the first section shows the frontend system, which includes oscillator, pulse stretcher and

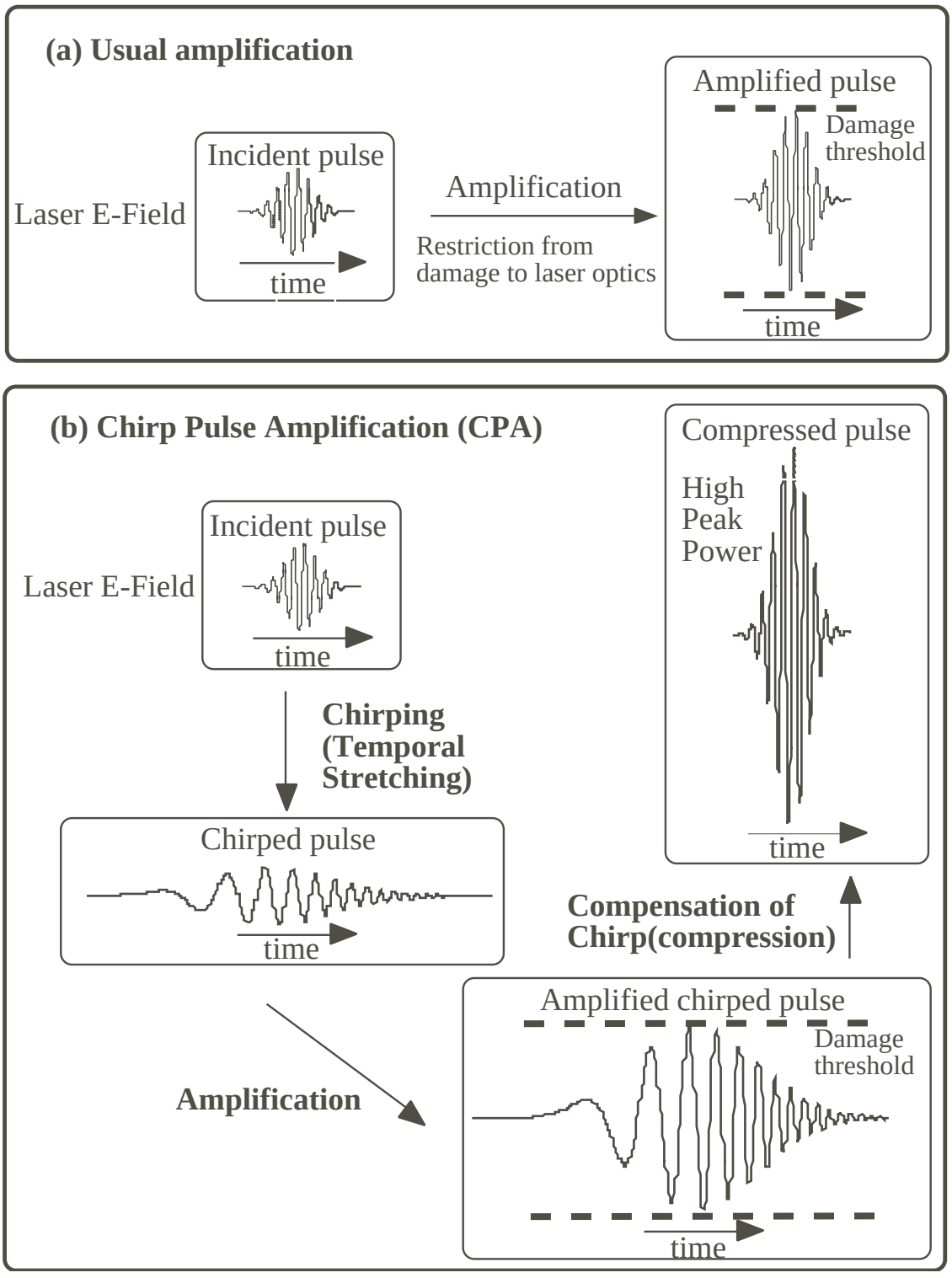

Figure 2.1: (a) Usual amplification method. The amplified gain is restricted from a damage to the laser optics such as amplifier glasses. (b) Chirped pulse amplification (CPA). An incident pulse is stretched temporally to reduce the energy density of the pulse, resulting to enable to amplify the pulse at higher energy. Finally, the amplified pulse is compressed temporally to obtain a high peak power.

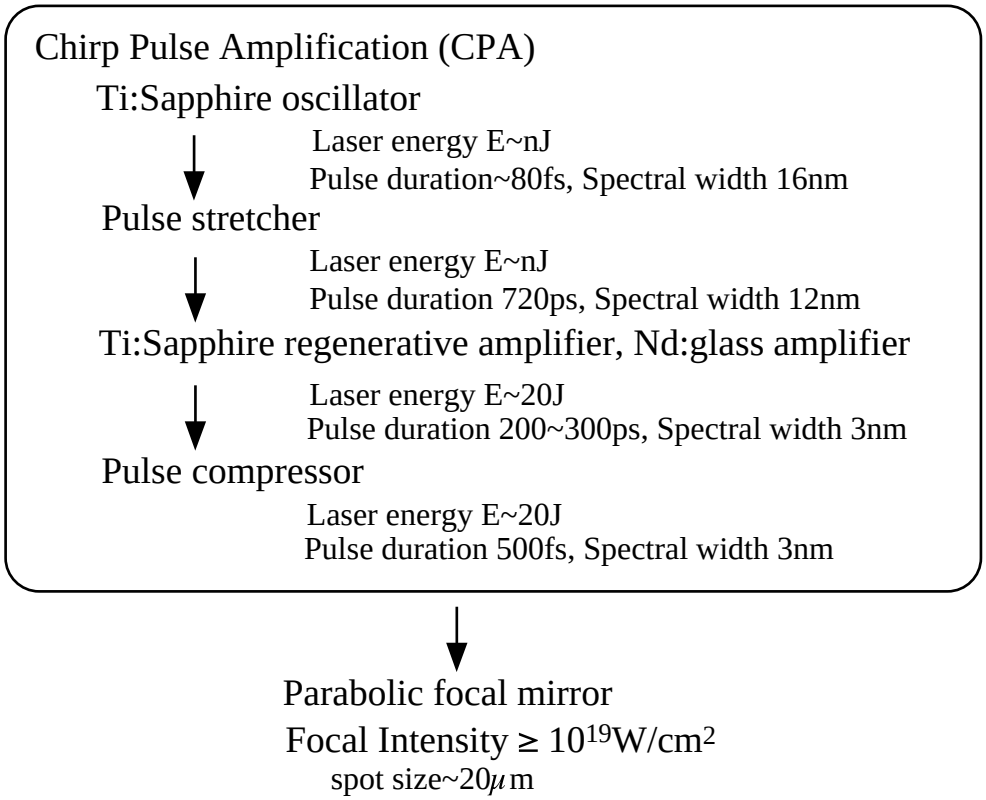

Figure 2.2: The CPA system diagram.

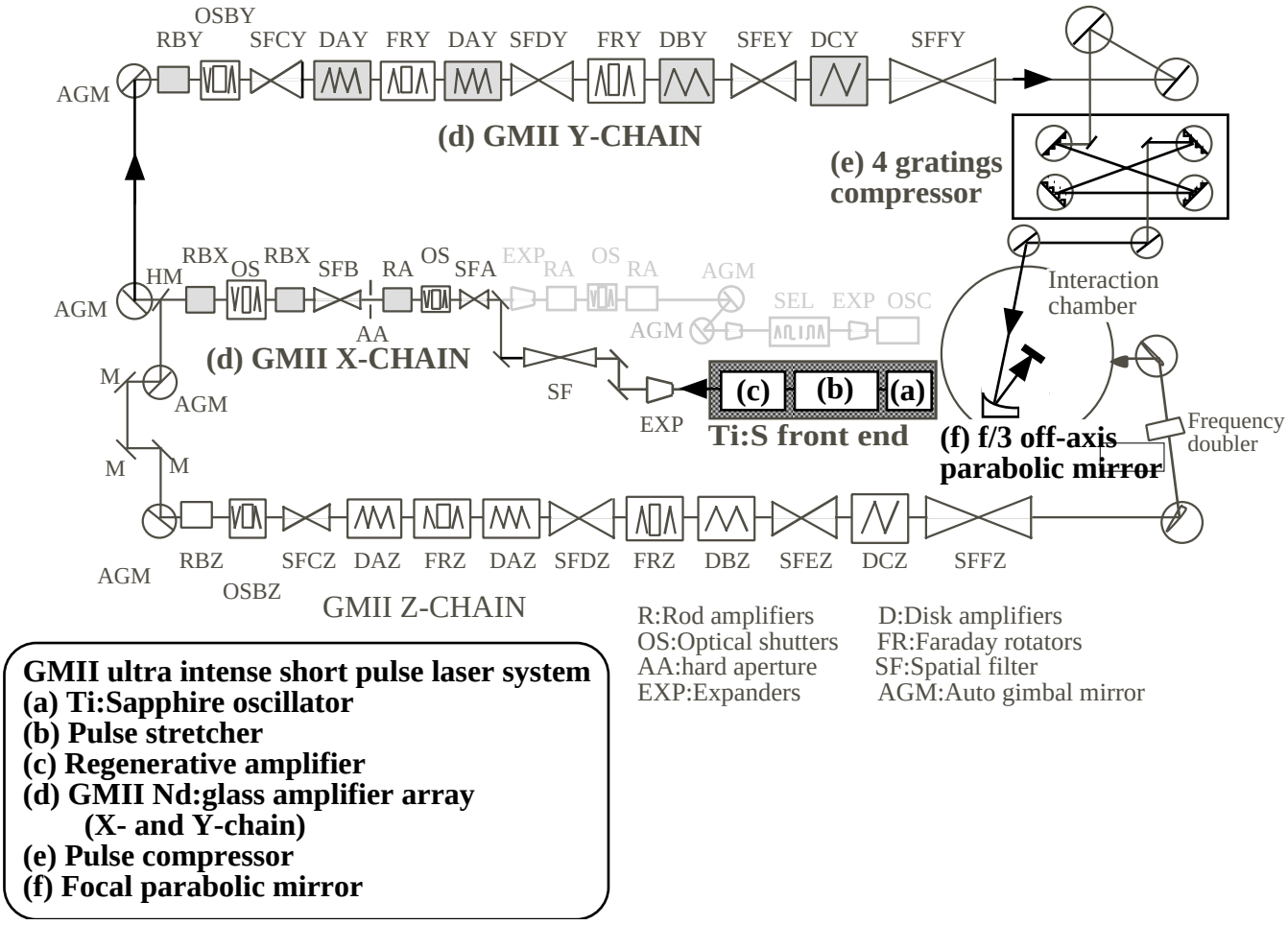

Figure 2.3: Constitution of the short pulse ultra intense laser system

regenerative amplifier. The second is about laser amplification with a spectral response of the glass amplifier and a self phase modulation from nonlinear reflectivity of the glass. The third part is described about pulse compression using a grating pair. The last section shows about laser focusing corresponding to the laser intensity.

2.3 Frontend system

The frontend system is purposed to generate a chirp pulse and pre-amplify the pulse before the glass amplifier. The frontend system is consisted of Ti:sapphire oscillator, pulse stretcher and Ti:sapphire regenerative amplifier as shown in Figure 2.4.

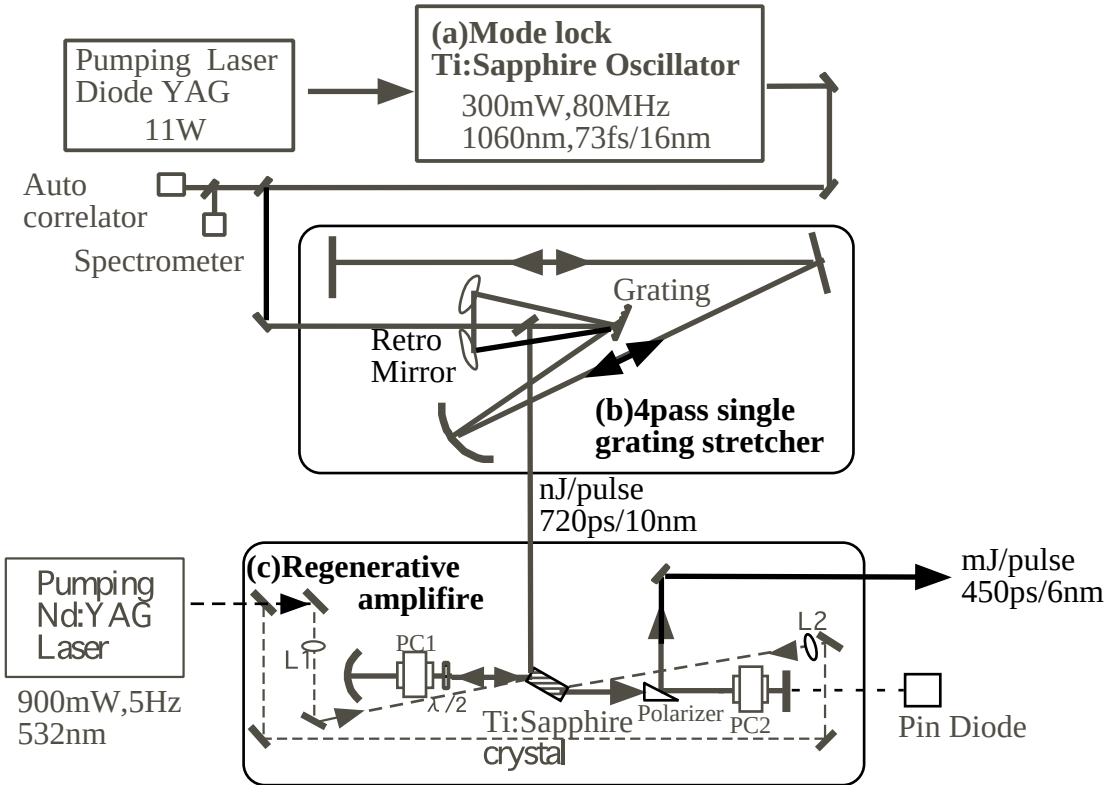

Figure 2.4: A layout of the frontend system. (a)Ti:sapphire oscillator. (b)Pulse stretcher. (c)Ti:sapphire regenerative amplifier.

2.3.1 Ti:sapphire oscillator

The Ti:sapphire oscillator (Tsunami 3960-L2X, Spectra Physics), which is pumped by a laserdiode (Millennia X's, Spectra Physics) with 10.0W light, generates 80MHz ultra-short pulses. Oscillation wavelength at the oscillator is variable by using a prism in the oscillator. In this system, the center wavelength of light at end of the frontend must be set at 1053nm which is center wavelength of gain cross section of the glass amplifier at GMII. Figure 2.5 shows gain spectrum of the Ti:sapphire crystal.

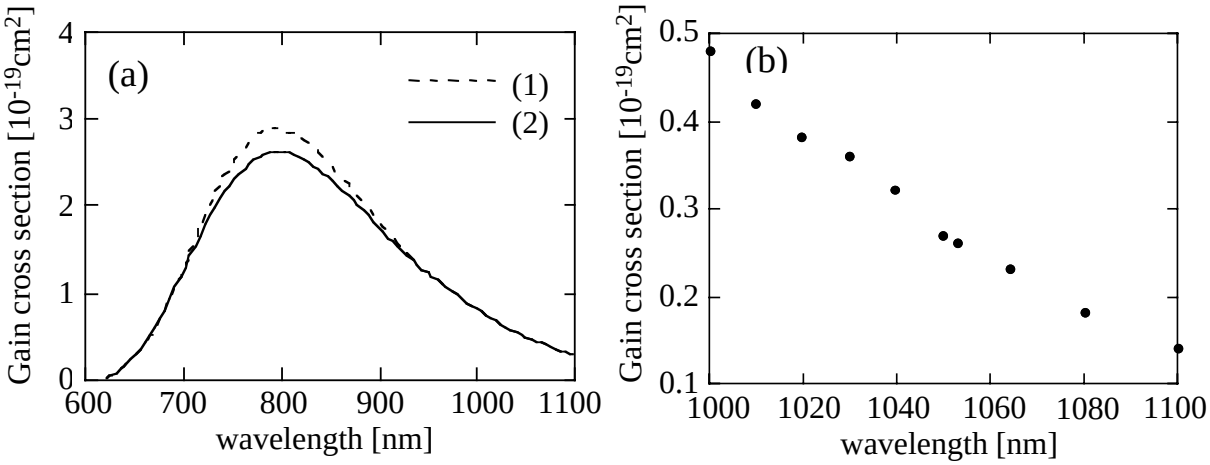

Figure 2.5: The cross section of the stimulated emission of the Ti:sapphire crystal. (a) The cross section ranging at 600-1100nm (Solid line [10], dotted line [11]). (b) The cross section data ranging at 1000-1100nm [12].

The cross section at $1.053\mu m$ is about as small as 10% of that of at 0.8μm and the gain decrease with the wavelength at $1.053\mu m$. Therefore, the center wavelength of the pulse in regenerative amplifier moves to lower wavelength after the amplification. Taking account of the spectral response in the regenerative amplifier, the oscillation wavelength was set at 1060nm. This center wavelength determines a laser energy of 3.8×10^{-9} J/pulse, a pulse duration of 72fs and a spectral width of 16nm as shown in Figs.2.6.

A product of the spectrum width in frequency and the pulse duration is 0.3148, resulting in good agreement with that of Fourier limit of the soliton shape pulse given by 0.315.

2.3.2 Pulse stretcher

The pulses from the oscillator are stretched temporally in the pulse stretcher. The temporal stretching is realized to utilize a spectral dispersion at a grating. This spectral dispersion is given by

$$sin\theta + sin\varphi = \frac{\lambda}{d}, \tag{2.1}$$

where θ is the incident angle to the grating, φ the reflection angle and d the grooves of the grating. This relation is called first order spectral dispersion. If the grating pair placed parallel or anti-parallel as shown in Figs. 2.7(a) or (b), the time delay is generated among each wavelength due to differences of path length (Figs.2.7(c)). Usually, anti-paralleled grating pair is used for pulse stretching, and paralleled grating pair is for pulse compression.

However, the temporal chirped laser is also broaden spatially in the spectral dispersion,

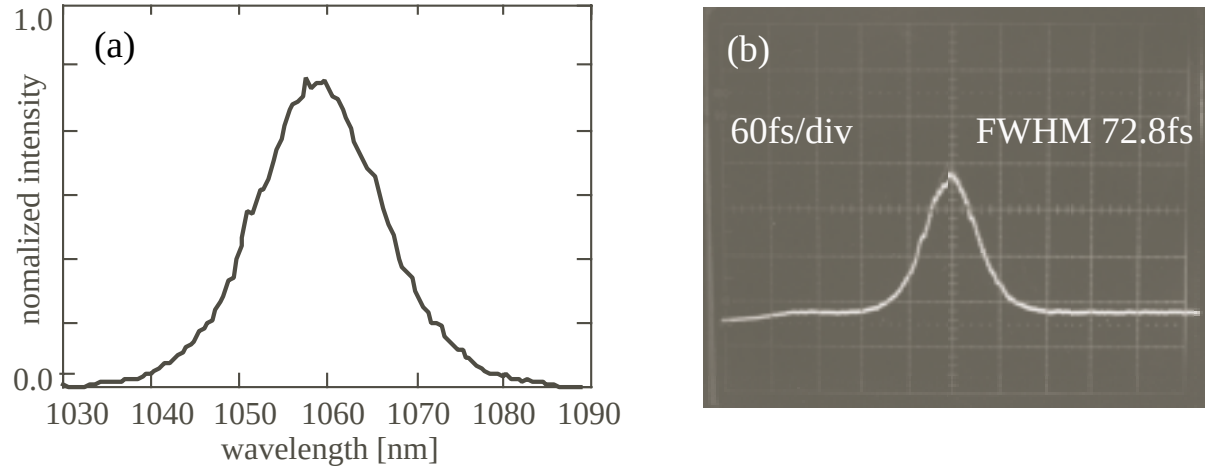

Figure 2.6: Pulse shape and spectrum from the oscillator. (a) Spectrum with the spectral width of 16nm. (b) Pulse shape with the pulse duration of 72fs.

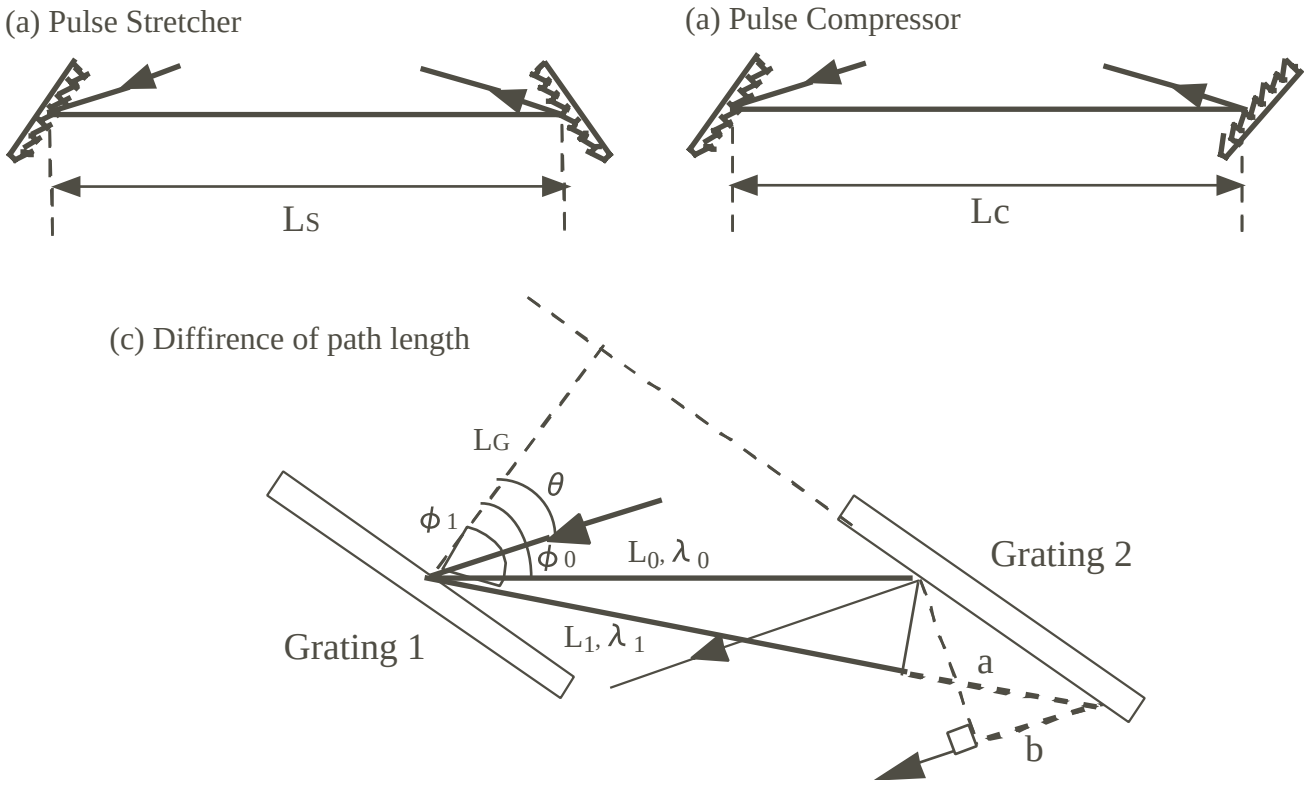

Figure 2.7: (a)Pulse stretcher. (b) Pulse compressor. (c)Difference of path length between λ_0 and λ_1 light.

resulting in generating spatial chirping. To compensate the spatial chirping, a retro mirror is used usually as shown in Fig.2.8 to return the light on the same path.

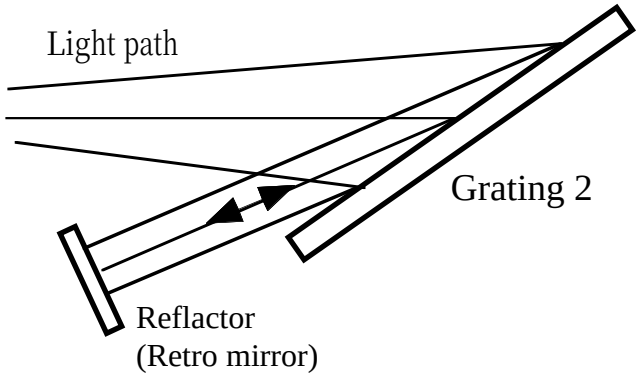

Figure 2.8: Retro mirror to compensate the spatial chirping in the spectral dispersion.

To estimate a chirped pulse width, I calculated a time delay between the light at the wavelength of λ_0 and λ_1. Assuming the deflection angle of each wavelength as φ_0 and φ_1, the dispersion relation to the incident angle θ is given by

$$sin\theta + sin\varphi_i = \frac{\lambda_i}{d}, (i = 0, 1). \tag{2.2}$$

If the path length between grating pair for each wavelength is given by L_0 and L_1 as shown in Figs.2.7(c), difference of the path length is equivalent to $a(= L_0 - L_1) + b$. Therefore, the time delay is given by

$$\tau = \mp\frac{L_1}{c}\left[\frac{cos\varphi_1}{cos\varphi_0}(sin\varphi_0 sin\theta + 1) - (sin\varphi_1 sin\theta + 1)\right], \tag{2.3}$$

where plus of the right hand in the equation is the time delay for compressor, minus that for the stretcher.

Using the time delay, an electric field of the chirped pulse is given by

$$\begin{aligned} \mathbf{E}(t) &= E_0 exp(-i\omega[t - (\tau_{stretcher} - \tau_{compressor})]), & (2.4)\\ &= E_0 e^{-i\omega t} exp(i(\phi_{stretcher}(\omega) - \phi_{compressor}(\omega))), \\ where \quad \phi(\omega) &= \tau\omega. & (2.5) \end{aligned}$$

At an ideal CPA , the phase generated in the pulse stretcher must be canceled by that in the pulse compressor to all laser frequency, giving

$$\phi_{total} = \phi_{stretcher}(\omega) - \phi_{compressor}(\omega) = 0. \tag{2.6}$$

In the system, the pulse stretcher is consisted of a single grating and retro mirrors as a four-pass one-grating type stretcher as shown in Fig. 2.9 to be compact.

The groove of the grating d is 1200 l/mm, the incident angle to the grating θ is 27.8 deg., and grating distance L (=2f-2z, f is the focal length of the concave mirror M1, z the

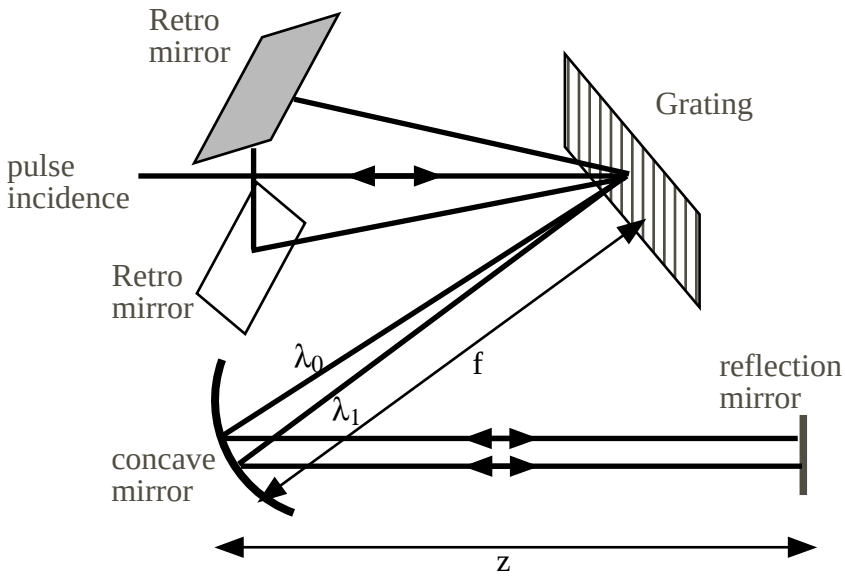

Figure 2.9: 4 pass - 1 grating type pulse stretcher.

distance between grating and the concave mirror) is 2.36m. The calculated chirping in the pulse stretcher from the equation 2.3 is 710ps/10nm. The spectral width is limited in 10nm by clipping the spectrum due to reflection mirror size in the pulse stretcher as shown in Figs2.10(a). Figs.2.10(b) shows the pulse shape from the pulse stretcher with 720ps pulse duration, resulting in good agreement with the calculation.

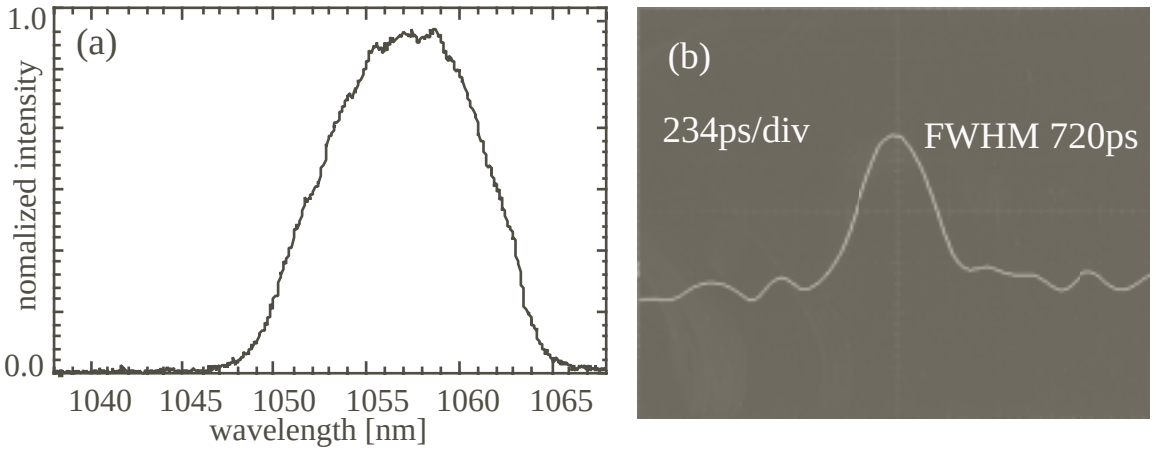

Figure 2.10: Pulse shape and spectrum out of the pulse stretcher. (a) Spectrum with the spectral width of 10nm. (b) Pulse shape with the chirped pulse duration of 720ps.

2.3.3 Regenerative amplifier

To obtain a total laser energy of 20J, the chirped pulse must be amplified from nJ to mJ level before the injection to glass amplifiers. For this purpose, the regenerative amplifier is used in the system as a pre-amplifier. Figure 2.11 shows a concept of the regenerative amplifier. A seed pulse is injected into the cavity by optical switching to rotate the laser polarization. The pulse is amplified at the laser medium for the round trips in the cavity and extracted from there by the other switching.

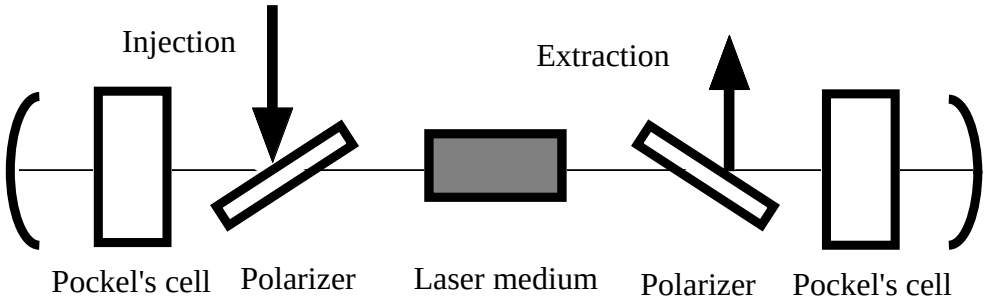

Figure 2.11: Concept of Regenerative amplifier. A seed pulse injected into the cavity by optical switching to rotate the laser polarization is amplified at the laser medium for the round trips in the cavity and extracted from there by the other switching

In general, regenerative amplifier has advantages on the efficiently energy extraction and the quality of beam profile. On the other hand, the disadvantages are optical damages in the cavity due to high energy density of the pulse and reduction of spectral width through the amplification (gain narrowing). This disadvantages are settled to use a large-diameter laser medium with broad band width of gain cross section such as Ti:sapphire crystal in the regenerative amplifier. Figure 2.12 shows the configuration of the regenerative amplifier used in the system. The Ti:sapphire crystal is pumped by frequency-doubled light (0.53μm) of Nd:YAG laser (GCR-270, Spectra Physics) at an energy of 190mJ with a repetition rate of 5Hz. The YAG pumping light is divided in two pass and focused on both ends of the Ti:sapphire crystal. The focal spot of the YAG laser on the crystal surface is an elliptic shape with a long-diameter of 4mm and a short-diameter of 1.5mm. The flounce at the end of the crystal is 4J/cm^2 on the each side. The Ti:sapphire crystal is 0.15wt% Ti-doped one inch diameter and has a size with 2.45cm length. Both ends of the crystal are cut with a Brewster angle and p-polarization light can pass into the crystal in the 95cm-distanse cavity.

The seed pulses from the pulse stretcher with s-polarization are rotated at 180° propagating twice in $\lambda/2$ plate before the pulses arrive to Ti:sapphire crystal, resulting in exclusion from the cavity at the crystal. One of seed pulses is rotated by the Pockel's cell 1 as shown in Fig.2.12 to p-polarization, therefore, the pulse can propagate into the cavity. Temporal response of the Pockel's cell is about 2ns, which is enough shorter to inject only one pulse than the pulse interval of the 80MHz seed pulses. The amplified pulse is extracted at the polarizor rotating the polarization of the pulse to s-polarization by the Pockel's cell 2. The polarization out of the regenerative amplifier is p-polarization

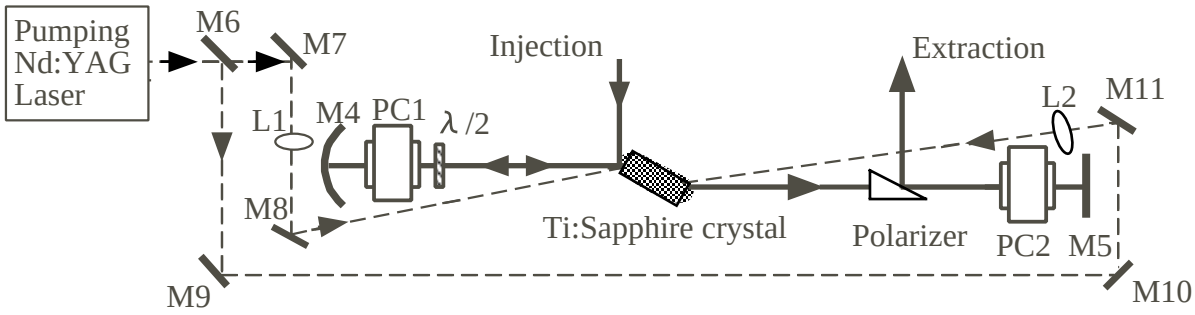

Figure 2.12: Configuration of the regenerative amplifier. M1 and M2 are the cavity mirrors, L1 and L2 the lenses, and P.C.1 and 2 the Pockel's cells.

by rotating the Pockel's cell 3 and $\lambda/4$ plate to reduce pre- and post-pulses.

The amplified energy and spectrum shape are estimated with the laser amplification simulation on the basis of equations described later in section 2.4 taking account of the spectral response in the regenerative amplifier. The total spectral response in the regenerative amplifier is estimated from the amplified spectrum of the ASE (amplified spontaneous emission) in the regenerative amplifier including a spectral response of the cavity and the gain spectrum of the Ti:sapphire. As shown in Fig.2.5, the cross section around at $1.053\mu m$ decreases with the increase in the wavelength. Therefore, the center wavelength of the pulse moves to lower wavelength after the amplification in the regenerative amplifier. From the results in the amplification simulation, the center wavelength of the seed pulse must be made at 1.060μm to be the output pulse at 1.053μm center wavelength in the regenerative amplifier.

Figure 2.13(a) shows the spectral shape from the regenerative amplifier. The dotted line in Fig.2.13(a) shows the simulation result of the amplified pulse spectrum, resulting in good agreement with the experimental results as shown by solid line with a 6.0nm spectral width. Figs.2.13(b) shows a pulse shape from the regenerative amplifier with a pulse duration of 450ps. The maximum energy of the amplified pulse in the simulation results is about 1mJ, resulting in also good agreement with the experimental results of 0.7-1.5mJ.

2.4 Glass amplifier

In the Nd:glass amplifier, a pulse from the frontend with an energy of 1mJ, a spectral width of 6nm and a pulse duration of 450ps is amplified to be a few tens Joule. The glass amplifier enable to be largely the medium scale, resulting in the extraction of high energy efficiently. However, the disadvantages are narrow band of the gain spectrum compared with Ti:sapphire, which cause to strongly gain narrowing and self-phase modulation (SPM) in the laser amplification due to a high energy density of the pulse. In this section, characteristic of the glass amplifier is described to optimize the chirped pulse amplification.

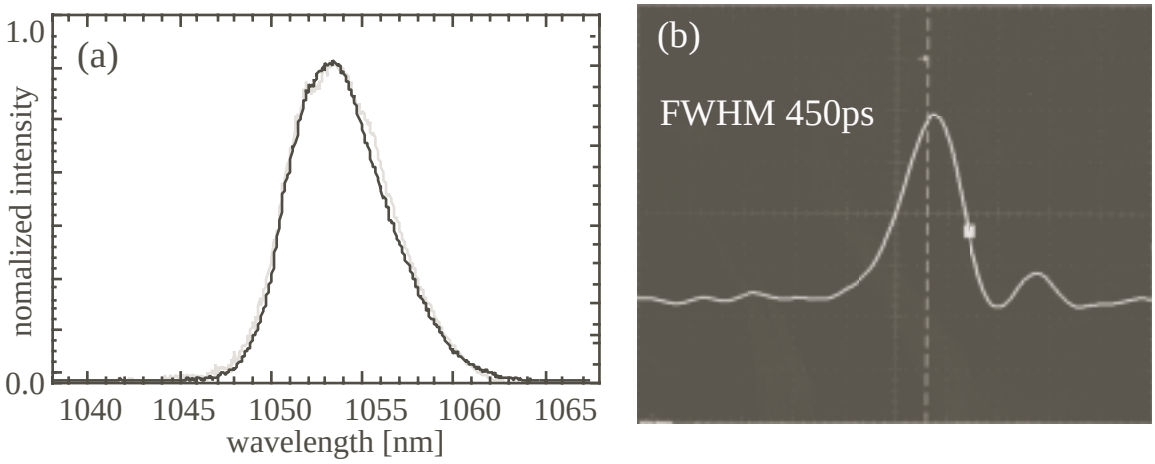

Figure 2.13: A pulse shape and a spectrum from the regenerative amplifier. (a) The experiment (solid line) and the calculated (dotted line) spectrum with a spectral width of 6nm. (b) The pulse shape with a pulse duration of 450ps.

2.4.1 GMII glass amplifier

The GMII amplifier uses LHG-8 (HOYA) Nd-doped phosphate glasses. Figure 2.14 shows a fluorescence spectrum of the LHG-8. The spectral width of the LHG-8 is 21.76nm at the center wavelength of 1053nm. The stimulated cross section at the center wavelength is $4.0 \times 10^{-20}\mathrm{cm}^2$. The lifetime of the upper level is 338μs, then decay of the population at upper level due to spontaneous emission during the laser amplification is negligible.

2.4.2 Laser amplification for the chirp pulse

When the laser propagates in nonlinear medium, 2nd-order nonlinear Schrödinger equation is given

$$i\frac{\partial \mathbf{E}}{\partial z} = i\frac{\alpha(\omega)}{2}\mathbf{E} + \frac{1}{2}\beta_2(\omega)\frac{\partial^2 \mathbf{E}}{\partial z^2} - \frac{1}{6}\beta_3(\omega)\frac{\partial^3 \mathbf{E}}{\partial z^3} - \gamma|E|^2\mathbf{E}, \tag{2.7}$$

where $\alpha(\omega)$ is the gain coefficient, $\beta_2(\omega)$ the group velocity dispersion in medium, $\beta_3(\omega)$ the group delay dispersion in medium and γ the nonlinear reflectivity index, given by $\gamma = \eta_2\omega_0/c$. Usually, a chirping due to the group-velocity dispersion and group-delay dispersion in the laser medium is much smaller than the chirping from the spectral dispersion at the grating, therefore the second and the third term of the right side of the equation can be negligible for the chirp pulse. When the electric field of the initial chirp pulse is given as $\mathbf{E} = E(z,\omega)exp(-i\phi_{chirp}(\omega))$, the electric field of the amplified pulse is given

$$E(z,\omega) = E(0,\omega)e^{\left(\frac{\alpha(\omega)z}{2}\right)}e^{i(\phi_{chirp}(\omega)+B(z))}, \tag{2.8}$$

$$where \quad B(z) = \int \gamma|E|^2 dz, \tag{2.9}$$

$$= \frac{2\pi}{\lambda}\int \eta_2|E|^2 dz. \tag{2.10}$$

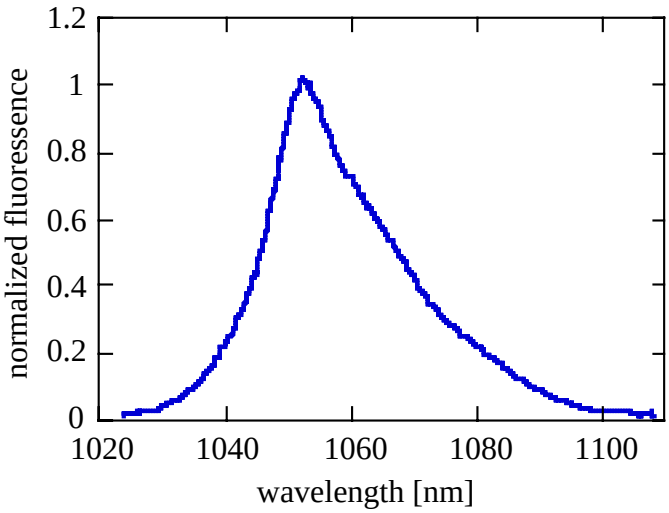

Figure 2.14: Fluorescence spectrum of the Phosphate glass LHG-8

Usually, the B in equation 2.10 is called "B-integral" as a value of degrees for the self-phase modulation(SPM). The B integral is also defined using the laser intensity $I = \frac{1}{2}\epsilon_0 c\mathbf{E}\mathbf{E}^*$, giving

$$B = \frac{2\pi}{\lambda}\int_0^L \gamma I(z)dz \qquad [rad], \tag{2.11}$$

$$\gamma = \frac{40\pi}{c\eta_0}\eta_2 \qquad [m^2/W], \tag{2.12}$$

where γ is the nonlinear refractive index coefficient, η_0 the reflective index and η_2 the nonlinear reflective index. If the laser intensity is low (I ¡¡ $1/\gamma$), the nonlinear term of the equation 2.10 can be negligible.

2.4.3 Gain narrowing in the glass amplifier

The pulse shape of the light without the phase modulation is determined by Fourier transform of the spectral shape. This means the amplified pulse spectrum shape determines the compressed pulse shape in the ideal CPA method. However, the gain spectrum of the glass amplifier is usually narrower than that of Ti:sapphire, resulting in gain narrowing in the glass amplification and giving a limitation on the shortening of the pulse duration.

To estimate the gain narrowing in the GMII amplifier, spectral response of the GMII amplifier was obtained by measurements of the spectral shape after the amplification using a spectrometer. Black solid lines in Figure 2.15 show the experimental spectra at different laser energies; (a)incident pulse spectrum with an energy of 2.75mJ and a spectral width 10.1nm, (b)amplified pulse spectrum with an energy of 350mJ and a spectral width of 5.38nm, (c)amplified pulse spectrum with an energy of 4.45J and a spectral width of 4.45nm,

and (d)amplified pulse spectrum with an energies of 18.44J and a spectral width of 3.7nm. It is clearly shows that the gain narrowing grows with the amplified laser energy.

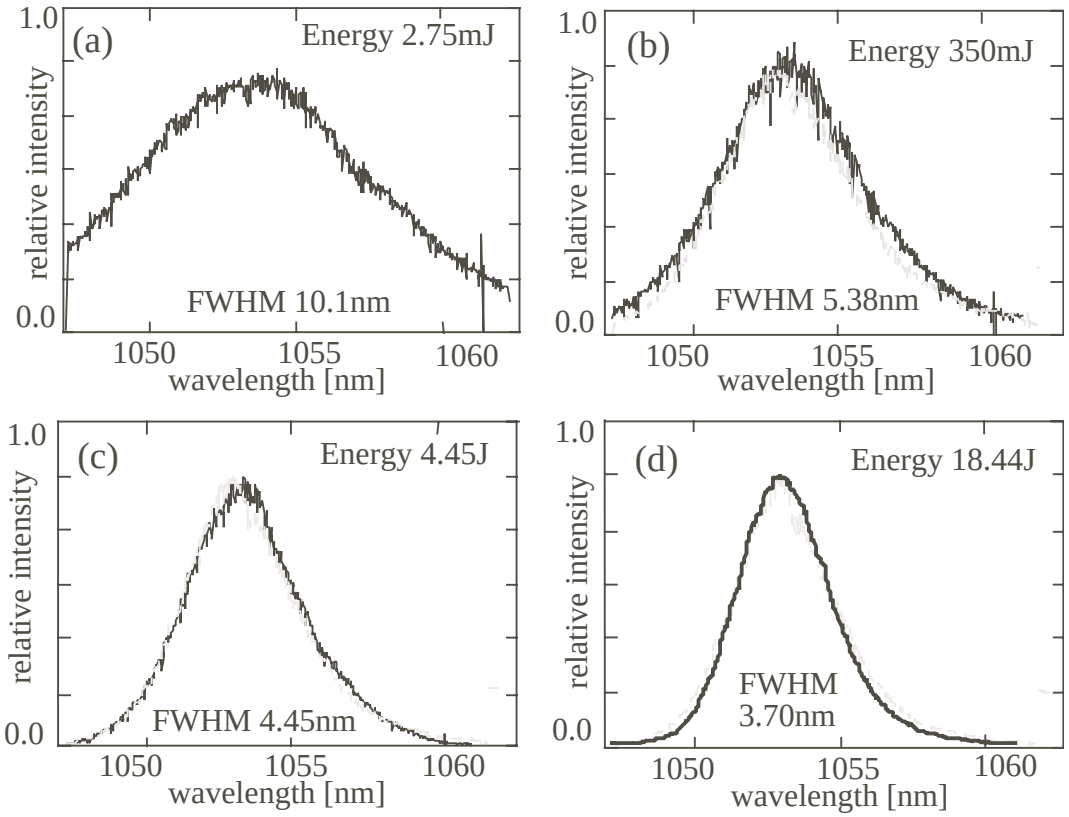

Figure 2.15: Amplified pulse spectra. Black solid line is the experiment, and gray solid line is the simulation result. Each laser energy is (a) 2.75mJ, (b) 350mJ, (c) 4.45J, and (d)18.44J.

The amplified spectrum is calculated by laser amplifier simulation based on equation 2.8 with fluorescence spectrum as shown in Fig.2.14. The calculated spectra of each amplified energy is also shown as gray solid line in Fig.2.15. The calculation is in good agreement with the experiments.

Figure 2.16 shows the summary of the spectral width (FWHM) as a function of the laser energy for the experiments(circles) and calculations(solid line). The dotted line in Fig.2.16 shows the estimated pulse duration from the calculation, indicating in the compressed pulse duration of 500fs at the 20J amplification in the system.

2.4.4 Self phase modulation

As intense laser light propagates into a optical medium, phase of the light is temporally and spatially modulated due to the nonlinear reflectivity of the medium. These self-phase modulations affect the performance of the pulse compression and the laser focusing. A

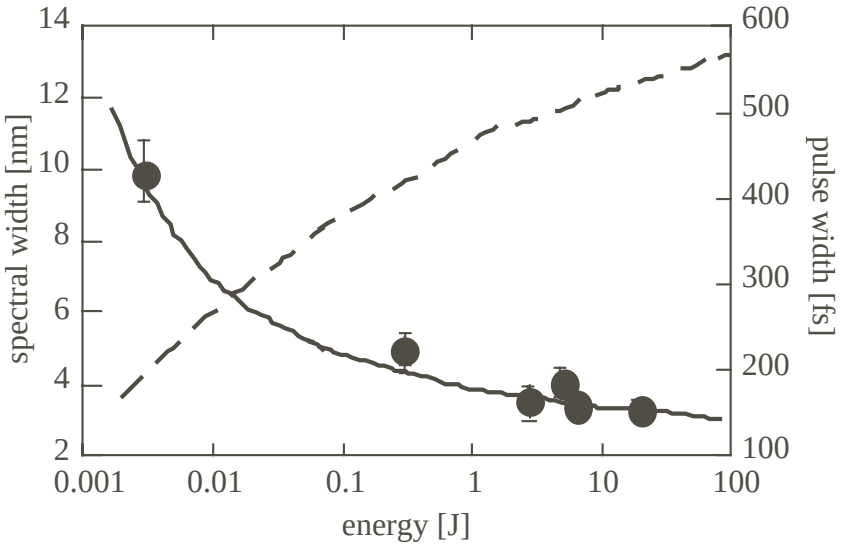

Figure 2.16: Summary of gain narrowing and compressed pulse duration. The Solid line is the calculated spectral width with the laser energies. Filled circle is the experimental results of the spectral width. Dashed line is the pulse duration of the calculated compressed pulse.

magnitude of the self-phase modulation is represented by B-integral value as shown in section 2.4.

The influence of B integral value on the compressed pulse shape and focal intensities are shown in Fig.2.17. Figure 2.17(a) shows the compressed pulse shape with various additional phase from B-integral value changing 0 to 5 rad. In the results, over 2 rad of B integral value affects significantly on the compressed pulse shape. On the other hand, Fig.2.17(b) shows the focal spot size (solid line) and the relevant focal intensity (dotted line) changing the B-integral from o to 5 rad, as laser peak power is fixed at 30TW. The result shows the laser intensity become a half of the maximum at the B integral value of 2.5 rad. In the results, the B-integral value must be lower than 2 rad. to avoid significant effect on the compressed pulse shape and laser intensity.

The B-integral value in the GMII system is calculated by using the amplification simulation code as shown in section 2.4. Fig.2.18(a) shows the B-integral and energy obtained with the GMII amplifier without optimization to the pumping rate of the amplifiers. Finally, the B integral become 2.5 rad with the laser energy of the 25J. However, the result as shown in Fig.2.18(b) is adjusted in gain rate of glass amplifiers to minimize the B-integral value, resulting in 2.0 rad with final laser energy of the 40J. In the results, the influence is not serious under 20J amplification, corresponding to 1.5 rad of the B-integral in the system.

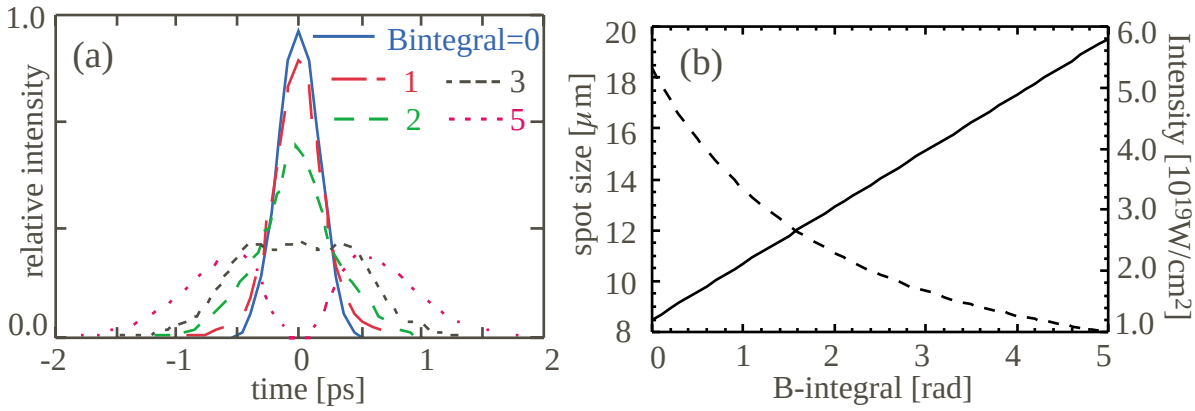

Figure 2.17: An influence of the B integral value. (a) The calculated compressed pulse shape changing the B-integral from 0 to 5 rad. (b)The focal spot size (solid line) and relative laser intensity (dotted line) as the laser peak power is fixed at 30TW.

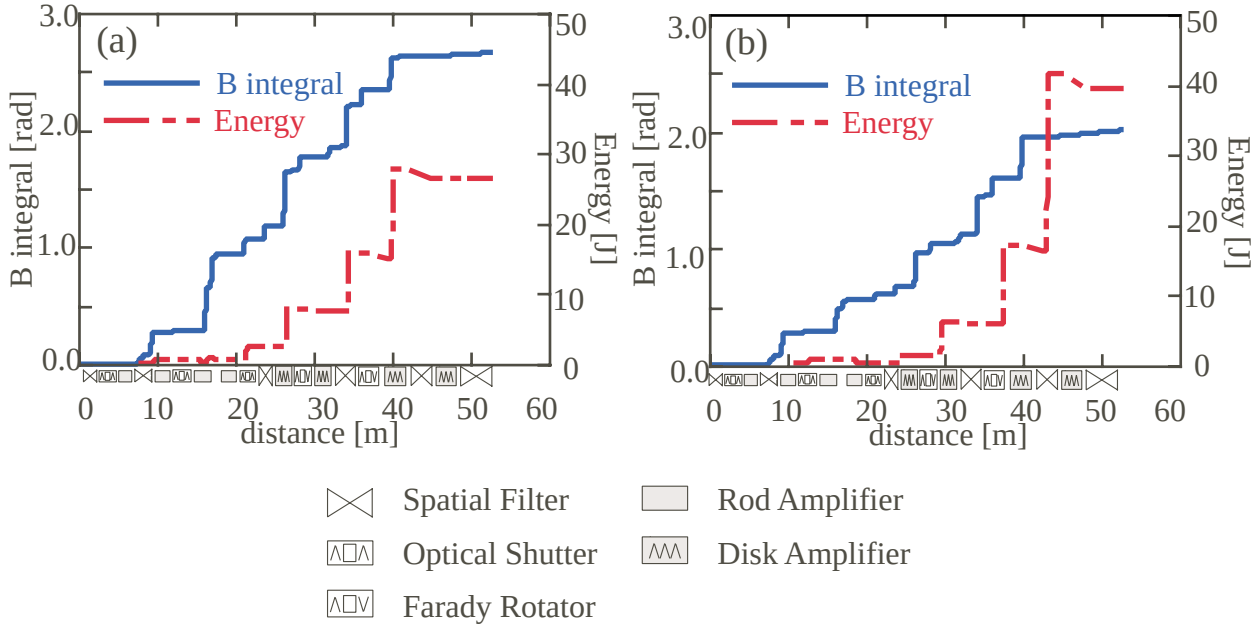

Figure 2.18: Simulation results of transition of B integral value as a function of the amplified laser energy with different gain rate of the glass amplifiers. (a) The result of successively increase of the gain rate. (b) The result to minimize the B-integral value.

2.5 Pulse compression

After the amplification, the laser pulse is compressed temporally to compensate the phase of chirp pulse. However, if the phase is not canceled, the compressed pulse shape is affected by the remained phase as shown in section 2.4. In this section, influence of adjustment mismatch between pulse stretcher and compressor on the compressed pulse shape is estimated. Finally, the obtained compressed pulse shape is compared the calculation.

2.5.1 Estimating mismatch between grating pair

At the ideal chirp pulse amplification, total time delay after the pulse compression is equal to 0. However, it is difficult to be 0 phase because of the mismatching between grating pair, self-phase modulation through the amplification and so on. The influence of the self-phase modulation has been mentioned in the section 2.4, in this section, arrangement mismatching between the stretcher and the compressor are described. I calculate the compressed pulse shape when an incident angle and grating parallel of the compression gratings are shifted to $\Delta\theta$ from the ideal position as shown in Fig. 2.19.

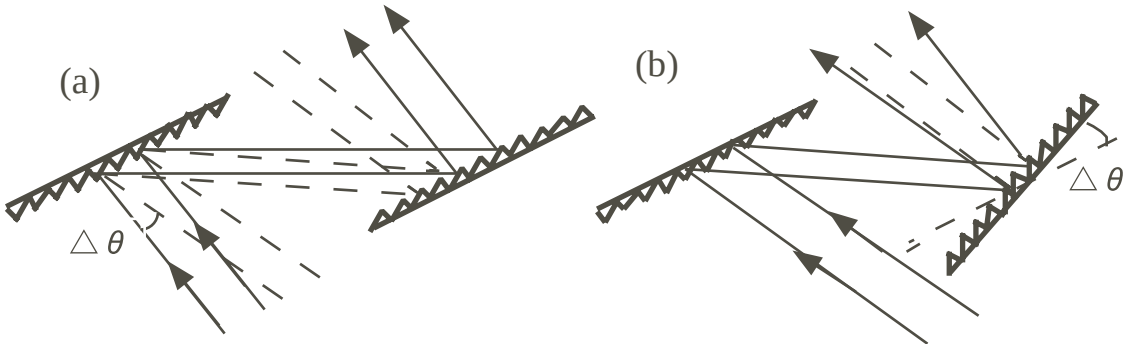

Figure 2.19: Misarrangement of the pulse compressor. (a) Incident angle shift. (b) Shift of parallel between gratings.

In the calculation, the grooves of the gratings in the stretcher and compressor is 1200 l/mm, and the incident angle and distance between grating pair are fixed at 27.4 deg. and 2.36m. And incident pulse is assumed to Gaussian shape with 3.5nm spectral width at the center wavelength of 1053nm. The results to the shifted angle $\Delta\theta$ are shown in Fig.2.20.

The incident angle shift that is under 1mrad shows not significant influence on the compressed pulse shape. In the system, an accuracy of the incident angle to the compression grating is under 0.1mrad, resulting in negligible of the influence in the compressed pulse. On the other hand, grating parallel arrangement affects significantly on the compressed pulse shape compared with the incident angle shift. At least, the accuracy of the grating parallel arrangement requires less than 0.1mrad. The stepping motor for the grating rotation can move in order of 1μrad in the system, therefore the shift can be compensated.

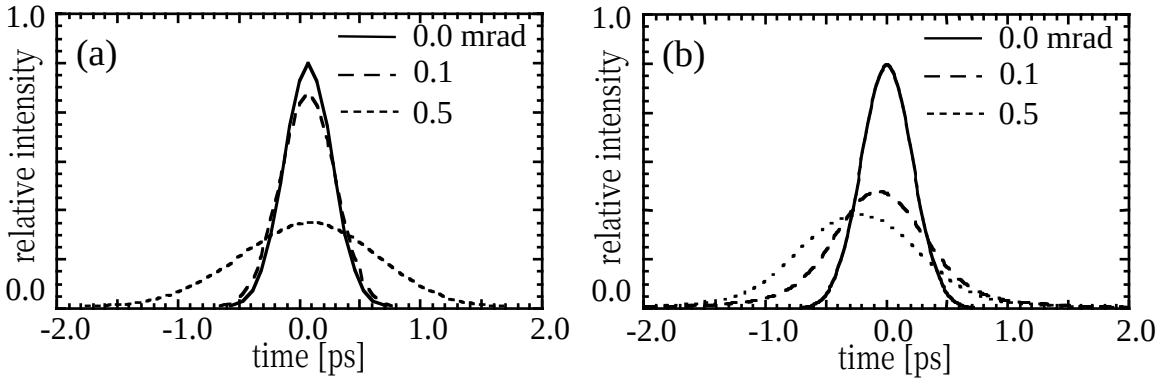

Figure 2.20: The compressed pulse shape as misarrangement of the pulse compressor. (a) Incident angle shift of 0.0, 0.1, and 0.5 mrad. (b) Shift of grating parallel of 0.0, 0.1, and 0.5 mrad.

2.5.2 The compressed pulse shape in pulse compressor

In the system, the compression chamber is used 4 grating system as shown in Fig.2.21. The advantage of the 4 grating system is to be easy of the grating arraignment and to small of the grating size.

The experimental amplified spectrum and the compressed pulse shape are shown in Fig.2.22. Fig.2.22(a) shows the amplified pulse spectrum as a black solid line with the calculated amplified spectrum as a gray solid line. The amplified energy was 13.3J, and experimental spectral width was 2.93nm. And the solid line in Fig. 2.22(b) shows the compressed pulse shape detected by 2nd-order autocorrelator deconvoluted with the amplified pulse spectrum. The dotted line is the Fourier transformed shape of the amplified spectrum itself. The pulse duration of the deconvoluted pulse was 460fs, resulting in peak power of 35TW. On the other hand, the pulse duration from the Fourier transform of the spectral shape is 540fs. The difference of the pulse duration may be derived from the compressor grating misarrangement, indicating the increase of pedestal before and after the main pulse in Fig. 2.22(b).

Figure 2.23 shows the compressed pulse duration in the experiment with the estimated pulse duration from the calculated spectral width as shown in sectionsec:amp. The squares in Fig.2.16 show the pulse duration from the experiments at different energies. These pulse duration form the experiments is well agree with the calculations. In the results, the pulse duration were obtained in average of 500fs at the 20J amplification, resulting in laser peak power of 40TW.

2.6 Laser focusing

The intensity per an unit area of the compressed pulse is about 10^3 times larger than that of the pulse before the compression. When the 40TW laser with a 15cm diameter propagates a typical glass of which nonlinear reflective index $\sim 10^{-20} m^2/W$, the B-integral value

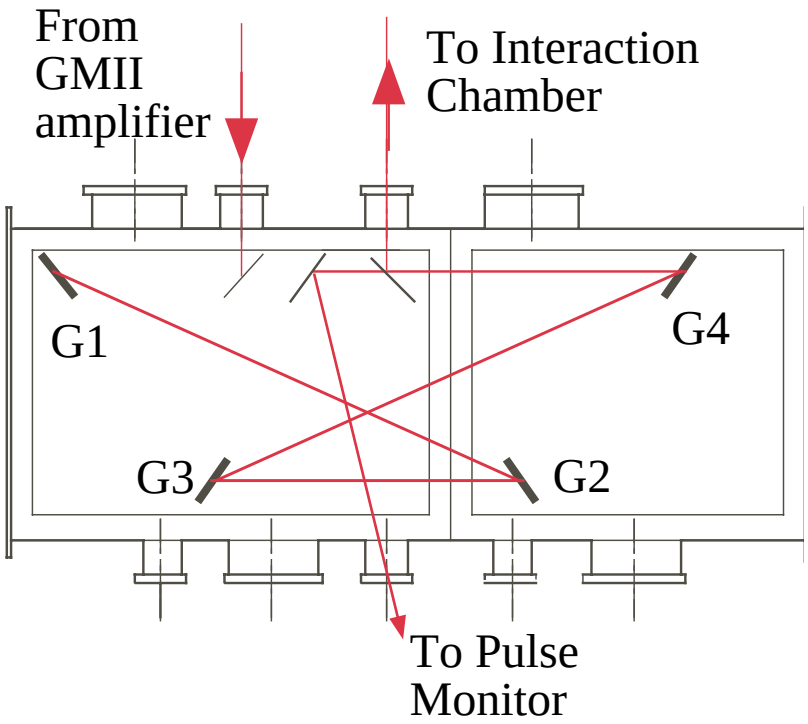

Figure 2.21: The compression chamber and the 4 gratings compressor.

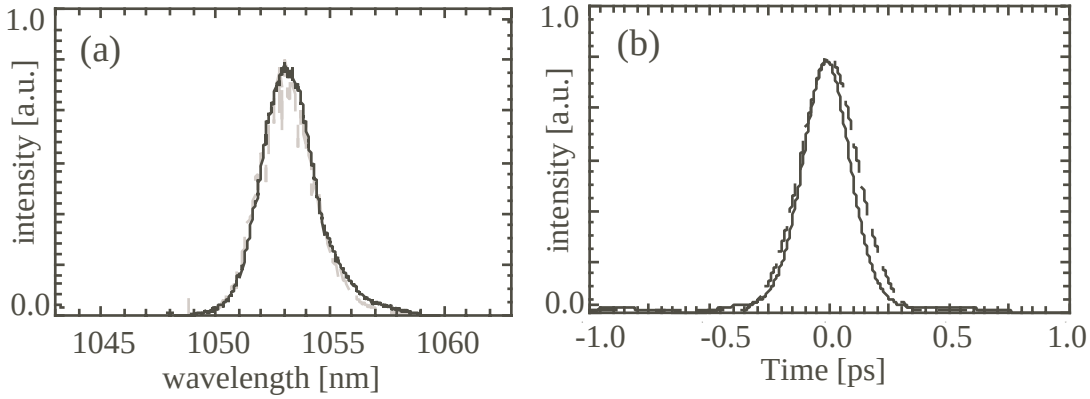

Figure 2.22: The amplified spectrum shape and the compressed pulse shape. (a)Typical spectrum used in the plasma interaction experiment (solid line : 2.93nm(FWHM)) and the calculated spectrum (dotted line : 3.1nm (FWHM)). (b) Deconvoluted pulse shape (solid line : 460fs (FWHM)) and Fourier transformed pulse shape (dotted line : 540fs(FWHM)).

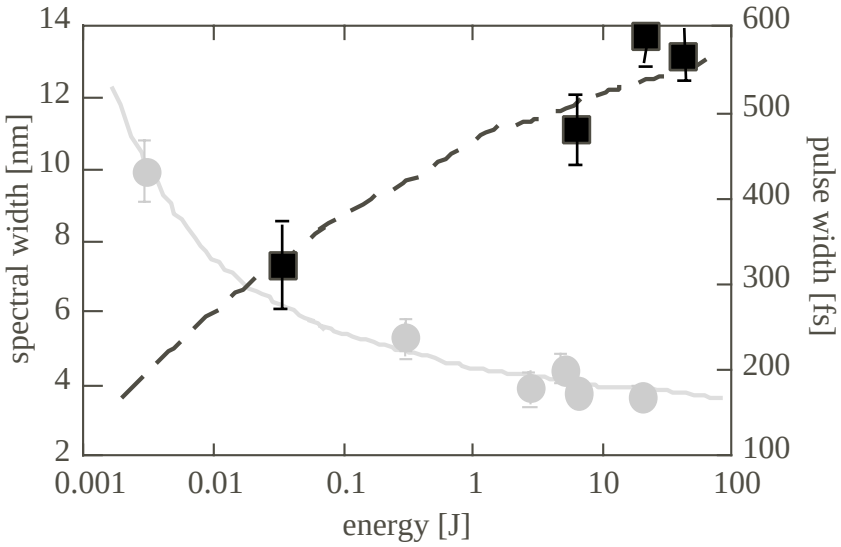

Figure 2.23: Summary of compressed pulse duration in the experiment with the estimated pulse duration from the calculated spectral width.

per a centimeter become up to 1.5 rad. Therefore, the laser focusing using a translation focal mirror induces rapidly distortion of the wave front, resulting in decrease in the focal intensity. In the system, an off-axis reflection mirror is used as a focal mirror to avoid the distortion.

The focal length of the off-axis mirror is f/3. The off-axis angle is 25° and the maximum surface accuracy is about $\lambda/6$. The parabolic mirror is coated by the multi-layer dielectrics with the ±100nm width of the reflection wavelength at the center of 1053nm. Figure 2.24 shows a typical focal spot image for a 20μm thick Al target detected by a x-ray pin-hole camera with a spatial resolution of the pin-hole image of about 13μm with the laser energy of 6.9J on target. Assuming the Gaussian shape, the spot size on the target was 25.4×14.1μm at the 1/e from the peak, resulting in the peak focal intensity of $2.2\times10^{19}W/cm^2$ with the average intensity at the 1/e of $3.1\times10^{18}W/cm^2$.

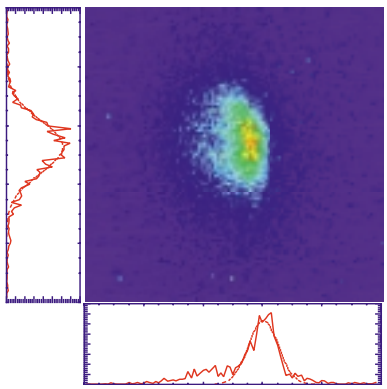

Figure 2.24: The focal spot image detected by an X-ray pin-hole CCD camera.

2.7 Summary

I developed ultra intense short pulse CPA laser system using Ti:sapphire oscillator coupled with Nd:glass amplifier. The pulse oscillated by the Ti:sapphire is stretched temporally to about 720ps by a grating in the pulse stretcher. The pulse is amplified to a few tens joule by Nd:glass amplifiers in GEKKO-Module II(GMII) system at Institute of Laser Engineering (ILE). The amplified pulse is compressed temporally to fourier limit pulse by four gratings compressor, resulting in obtained pulse duration of the pulse of 500fs and the peak power of 40TW. The pulse is finally focused by f/3 off-axis parabolic mirror to the diameter of ten μm, resulting in the intensities of 10^{19}W/cm^2. The influences of the self-phase modulation and grating misarrangement on the compressed pulse shape and laser focusing are negligible under 20J amplification to adjust the gain of the each amplifier.

Reference

[1] D. Strickland and G. Mourou, Opt. Comm. **56**, 219 (1985).

[2] *Ultrafast phenomena VII:proceedings of the International Conference*, (Springer-Verlag, New York),75 (1990).

[3] D. E. Spence, P. N. Kean and W. Sibbett, Opt. Lett. **16**, 42 (1991).

[4] B. C. Stuart, M. D. Perry, J. Miller, G. Tietbohl, S. Herman, J. A. Britten, C. Brown, D. Pennington, V. Yanovsky, and K. Wharton, Opt. Lett. **22**, 242 (1997).

[5] K. Yamakawa, H. Shiraga, Y. Kato, and C. P. J. Barty, Opt. Lett. **16**, 1593 (1991).

[6] C. N. Danson et al., Opt. Commun. **103**, 392 (1993).

[7] M. W. Phillips et al., Opt. Lett. **15**, 1453 (1992).

[8] J. Zhou et al., Opt. Lett. **19**, 1149 (1994).

[9] A. Stingl, M. Lenzner, Ch. Spielmann, F. Krausz, R. Szipöcs, Opt. Lett. **20**, 602 (1995).

[10] J. M. Eggleston, L. G. DeShazer, and K. W. Kangas, IEEE J. Quantum Electron. QE-**24**, 1009 (1988).

[11] L. G. DeShazer, J. M. Eggleston, and K. W. Kangas, *Tunable Solid-State Lasers II*, Springer-Verlag (Berlin), pp228-234 (1986).

[12] B. C. Start, S. Herman, and M. D. Perry, IEEE J. Quantum Elecon. QE-**31**, 528 (1995).

[13] M. D. Perry, T. Ditmire and B. C. Stuart, Opt. Lett. **19**, 2149 (1994).

Chapter 3

Pulse Shaping with Spectral Control

3.1 Introduction

CPA laser system using glass amplifiers can provide large energies and ultra-intense laser power such as 100TW [1]. However, the system have disadvantages on the spectral response such as gain narrowing which cause to broaden the pulse duration and non-Gaussian shape which generates a pedestal in the compressed pulse. 2nd-order harmonics conversion of the compressed pulse using a nonlinear crystal [8] can avoid the gain narrowing as same as increase of contrast ratio. However, there is a possibility to decrease the focal intensity in this method due to low conversion efficiency of laser energy at the nonlinear crystal and wave front distortion due to the phase modulation.

Another possibility to avoid the disadvantages is controlling the pulse spectrum, which determines the shape of the compressed pulse. Using mixed glass amplifiers such as phosphate and silicate is one of the methods to avoid gain narrowing and obtain a shorter pulse duration [7]. Another method of spectral control is using etalon in high-power table-top laser system [9]. The pulse duration in the compressed pulse can be shortened to suppress the gain narrowing using these methods. But at the same time, prepulse or pedestal may be generated in the compressed pulse because of difficulties to control precisely the spectrum in these methods. Therefore, other method to control the spectrum could be required.

One of the possibilities to precise control of the spectrum is utilizing a spectral dispersion in the pulse stretcher. Some methods to control the spectrum in pulse stretcher were demonstrated in previous works. Putting a mask pattern [10] or liquid crystal modulator [11] into the optical pass in the pulse stretcher can easily change the chirped pulse spectrum. To be more precisely control of the spectrum of the chirped pulse, we used a thin film filter of which transmission rate changes for the first time.

We have demonstrated pulse shaping with spectral control using a spatial gradient filter in a pulse stretcher applying for the CPA system using glass amplifiers. The precise control of the spectrum of chirped pulse enabled to control of the prepulse before and after the main pulse and pedestal around the main pulse by changing spectrum of the chirp pulse taking account of the system spectral response. The spectral control was also applied to shorten the pulse duration from 500fs to 300fs at energy of 20J corresponding to 70TW with the glass amplifier system.

3.2 Pulse shaping in a CPA method with glass amplifiers

In a CPA laser system, a compressed pulse shape is determined by a Fourier transform of the amplified pulse spectrum given by

$$I_{com}(t) = \int_{-\infty}^{\infty} I_{amp}(\omega) e^{-i\omega t} dt, \tag{3.1}$$

where $I_{com}(t)$ is the temporal shape of the compressed pulse, ω the wave frequency and $I_{amp}(\omega)$ the spectral shape of the amplified pulse. This equation indicates the changing the pulse spectral shape $I_{amp}(\omega)$ allows to control the compressed pulse shape $I_{com}(t)$. Therefore, the spectral control of the amplified pulse can control the pulse shape in the compressed pulse. However, controlling the amplified pulse spectrum might generate significant phase shift by nonlinear effect in optical medium because of high energy density of the amplified pulse. On the other hand, controlling of the incident pulse spectrum before the glass amplifier enable to avoid the nonlinear effect as well as to control the pulse shape.

The pulse shaping with spectral control of the incident pulse in a glass laser system can be calculated with a laser amplification and compression code taking account of a spectral response of the system. When the controlled incident pulse spectra $I_c(\omega)$ is given by

$$I_c(\omega) = F(\omega) \cdot I_{nc}(\omega), \tag{3.2}$$

where $F(\omega)$ is the transmission of the spectral filter and $I_{nc}(\omega)$ the original incident pulse spectrum, then the amplified pulse spectrum $I_{amp}(\omega)$ in a small signal gain amplification is expressed by

$$I_{amp}(\omega) = e^{\Gamma\theta(\omega)\sigma(\omega)} \cdot I_c(\omega), \tag{3.3}$$

where Γ is energy gain, $\theta(\omega)$ the stimulated emission cross section and $\sigma(\omega)$ the total spectral response of the laser system such as at polarizers and at pockel's cells. We used the calibrated spectral response of the glass laser system as the $\sigma(\omega)$, which was precisely obtained through measurements of amplified spectrum shape in our system. Using these equations, we can calculate the compressed pulse shape with any spectral control of incident pulse such as prepulse control, pedestal reduction and shortening of the compressed pulse duration.

3.3 Experiments for pulse shaping

The experiments of pulse shaping with spectral control were performed using the GEKKO MII glass laser system at Institute of Laser Engineering, Osaka University [12]. The front end of the system consists of a Ti:sapphire oscillator, a pulse stretcher and a Ti:sapphire regenerative amplifier. The oscillator is operated at $1.053\mu m$ with a pulse duration of 100fs full width of half maximum (FWHM). The pulse is temporally stretched to 700ps (FWHM) using a grating (1200 g/mm) at the pulse stretcher. This pulse is taken into the regenerative amplifier, which is optically pumped at both ends of the Ti:sapphire crystal by the frequency-doubled output of a Q-switched Nd:YAG laser at a repetition rate of 5Hz.

The output pulse from the regenerative amplifier with energy of a few mJ is injected into the phosphate glass (LHG-8) amplifiers. The energy of 20-30J can be derived in the system with a clear aperture of 15cm.

The spectral control of the input pulse for the glass amplifiers was realized by utilizing the spatial dispersion in the pulse stretcher as shown in Fig.3.1. Insertion of a thin film filter with a spatial modulation on the transmission into the spatial dispersion at the pulse stretcher can change the spectral intensity profile of the chirped pulse. The spatial modulation of the transmission of the filter was determined to obtain appropriate spectrum after the regenerative amplifier taking account of spectral response through the amplification. The incident angle to the grating in the pulse stretcher is 27.4 degree and spatial dispersion in front of the Retro mirror, where the modulation filter is inserted, is about 3nm/cm from the ray-trace calculation.

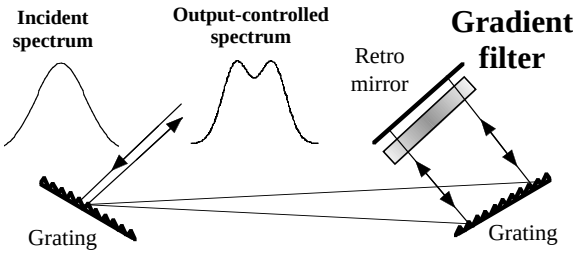

Figure 3.1: Spectral control at pulse stretcher. Laser pulse is dispersed spatially according to spectral dispersion relation on wavelength at grating. Inserting a thin film filter, whose transmission changes gradually in space, can make precisely control on the spectrum of the chirped pulse.

The influence of phase modulation due to the filter might become a significant problem on the pulse compression and focusing. We measured far field pattern of 8mm diameter laser beam after the regenerative amplifier with the spatial modulated filter by using a f/6 focal lens as compared with that for the case of no filter, resulting in no significant effect of the filter in the focal diameter ($\ll 1\%$). In the results, a phase modulation was estimated to be less than 0.1 radian ($\sim \lambda/50$) from the Frenel diffraction. Therefore, no significant effect of the filter on the pulse compression and beam focusing will be expected in a few hundred fs compressed pulse duration, which are affected by over 2 radian phase shifts in our system.

3.4 Prepulse control

One of the interests in the pulse shape is the prepulse control (prepulse timing or height ratio to the main pulse) from a viewpoint of various applications in laser plasma interaction. Figure 3.2 shows a typical calculation indicating a prepulse control in the compressed pulse by spectral shaping of the incident pulse using the glass amplifier system.

A solid and a dotted line in Figs.3.2(a) and (b) show the spectrum of the controlled and no-controlled (Gaussian) shape before and after the amplification, respectively. The

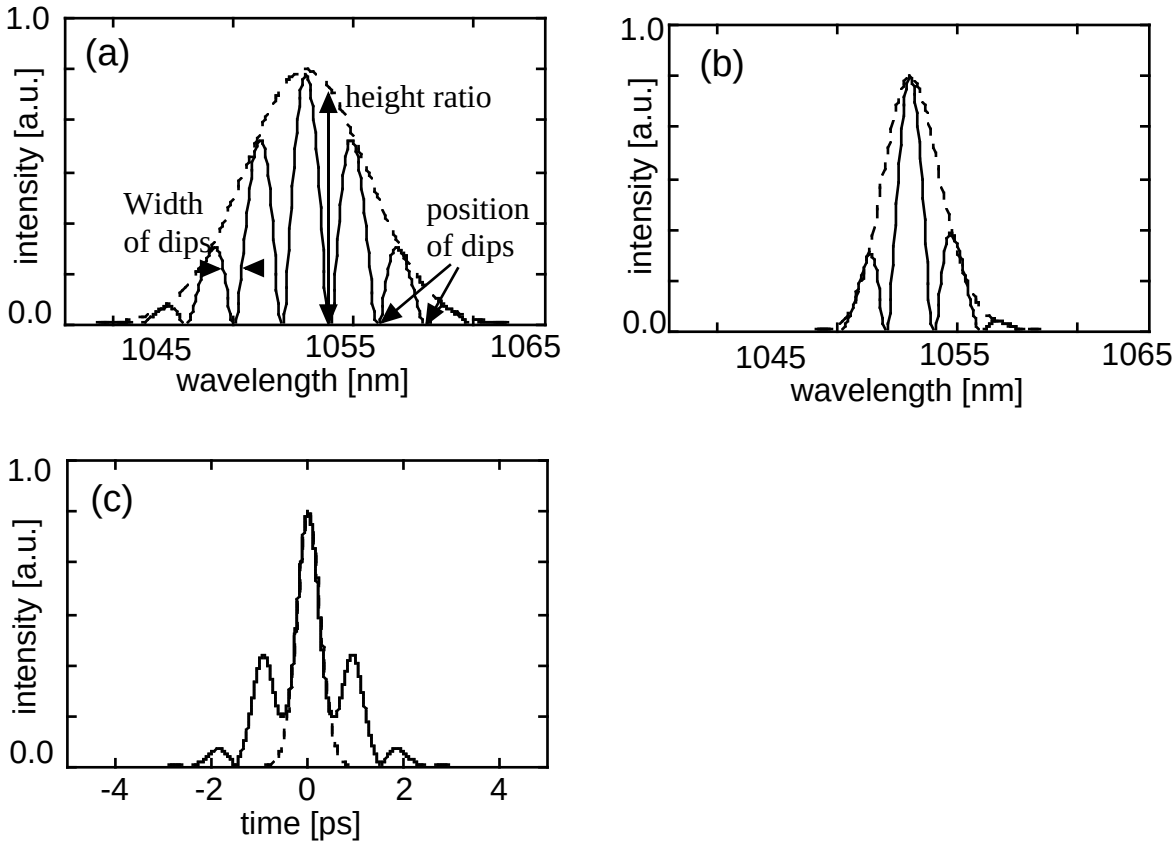

Figure 3.2: Outline of Prepulse control. (a) Incident spectra of controlled (solid line) with spectral dips and no-controlled (dotted line) pulse. (b) Amplified spectra of controlled (solid line) and no-controlled (dotted line) pulse. (c) Compressed pulse shape of controlled (solid line) and no-controlled (dotted line) pulse.

Table 3.1: Summary of the various spectral control to the incident pulse for the prepulses control in the compressed pulse.

Spectral control	Effect on the prepulse
Height of spectral dips	Prepulse intensity
Spectral position of dips	Prepulse timing
Width of spectral dips	Prepulse intensity, timing and number
Number of spectral dips	Pedestal between main and prepulse
Laser energy	No effect

energy gain in the glass laser is assumed to be 2×10^4 in the calculations. No differences are observed in the shape of the spectral envelope of the amplified pulse between the controlled pulse and the Gaussian one, because the width of the gain spectrum of the glass amplifier is relatively wider than the spectral width of the incident spectra. Then the pulse duration of main pulse in the compressed pulse is almost the same between the controlled pulse and the Gaussian one as shown in Fig.3.2(c).

The prepulse shape (timing and intensity) only depends on the spectral modulation. We changed the spectral modulation of the incident spectrum to control the prepulse timing and intensity in the compressed pulse. Table 3.1 show the summary of the various spectral control and its effect on the prepulse shape.

As the calculation condition, the amplification gain is fixed at 2×10^4. The height of the spectral dips in the incident pulse can change the prepulse height in the compressed pulse as shown in Figure 3.3(a). Solid, dashed, and dotted lines show the compressed pulse shape with the incident spectrum having 0.0, 0.25, and 0.5 of the height ratio of the spectral dips to the original Gaussian spectrum, respectively. In the results, prepulse intensities in the compressed pulse are increased in the depth of the spectral dips in the incident spectrum. On the other hand, a spectral position of the spectral dips from the center wavelength affects mainly the prepulse timing in the compressed pulse as shown in Fig.3.3(b). Solid, dashed, and dotted lines show the compressed pulse with 0.5, 1.0, and 2.0 nm of the spectral position of the spectral dips from the center wavelength, respectively. The spectral dips become closer to center wavelength, the timing between prepulse and main pulse becomes later. We checked also other spectral control for the prepulse control. A width of the spectral dips affects both prepulse intensity and timing at the same time, then the control of the dip width will be not appropriate for the precise control of the prepulse. Number of spectral dips and laser energy show no significant effect on the prepulse intensity and timing in the compressed pulse.

From these prepulse controls, we have demonstrated the prepulse timing control, which could be one of the most important control of the prepulse. Figure 3.4 shows typical experimental spectra and compressed pulse shape for prepulse timing control with spectral shaping.

The incident spectrum was controlled to be a spectral shape with the 1nm width dips located at 1nm blue and red sides from the center wavelength symmetrically. Black and

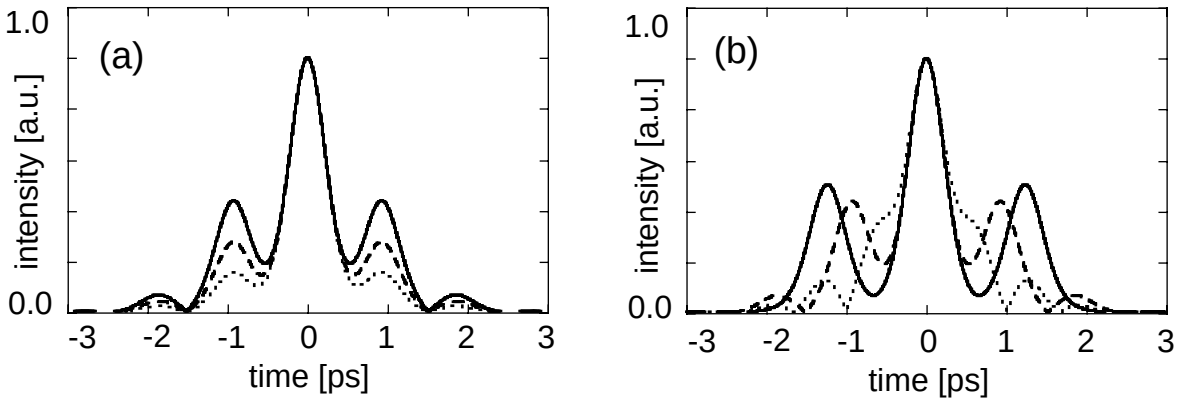

Figure 3.3: (a) Prepulse height control in the compressed pulse with changes of height of the spectral dips in the spectral shape of the incident pulse. Solid, dashed, and dotted lines show the compressed pulse shape with the incident spectrum having 0.0, 0.25, and 0.5 of the height ratio of the spectral dips to the original Gaussian spectrum, respectively. Width of the spectral dips and position of the dips from the center wavelength are fixed at both 1.0nm. (b) Prepulse timing control with a spectral position of the spectral dips from the center wavelength. Solid, dashed, and dotted lines show the compressed pulse with 0.5, 1.0, and 2.0 nm of the spectral position of the spectral dips from the center wavelength, respectively. Other calculation conditions are same as Fig.3.3(a).

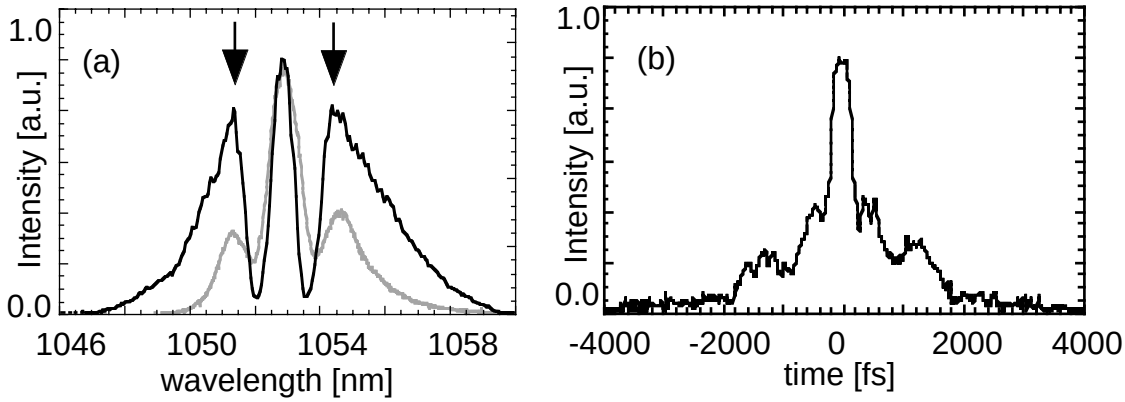

Figure 3.4: Experimental result for prepulse control. (a) Incident (black solid line) and amplified (gray solid line) spectrum of controlled pulse. The arrows show the wavelength of higher and lower spectral component, indicating no change of the positions through the amplification. (c) Compressed pulse shape deconvoluted the pulse shape detected by 2nd-order autocorrelator with the spectral shape.

Table 3.2: Summary of the experimental results of the prepulse timing control in the compressed pulse changing the spectral dip position from the center wavelength in the incident spectrum.

Position of spectral dips [nm]	Prepulse timing [ps]	Laser energy [J]
1.4	0.6	6.48
0.7	1.6	12.1
0.6	1.7	10.2
0.7	1.6	6.88

gray lines in Fig.3.4(a) show the incident and amplified spectrum of the controlled pulse, respectively. The center component of the controlled spectrum of the incident pulse had a peak wavelength of 1053nm and a width of 1nm, which were maintained after the amplification at the gain of about 2×10^4. The positions of the intensity peak of the spectral wing shown by arrows in Fig. 3.4(a) were also kept after the amplification. The compressed pulse shape of the controlled pulse is shown in Fig. 3.4(b), which is evaluated by an obtained spectrum and pulse shape of the 2nd-order auto-correlation. The prepulses and the postpulses were observed at 0.4ps and 1.2ps before/after the main pulse.

The prepulse timing has been changed to control the spectral dip position from the center wavelength in the incident spectrum as shown in Table 3.2.

All the width and height ratio of the spectral dips was fixed at 1.0nm and 0.1. The prepulse timing was decreased in increase of the spectral distance between the spectral dips and the center wavelength of the incident spectrum of the controlled pulse. On the other hand, the difference of the amplified energy has not affected on the prepulse timing of the compressed pulse shape of the controlled pulse.

In this control, the prepulse timing is restricted by the spectral width. In addition, if the spectral distance between the first spectral dip and the center wavelength are wider than the half of the spectral width (FWHM), the prepulse height control could be difficult because the change of the height ratio of the spectral dips become much smaller than peak of the main component. Therefore, the prepulse control with the spectral control will be suited for less than a few ps timing of the prepulse, which is difficult to control with other method of prepulse control.

3.5 Pedestal control

It is also possible to suppress the pedestal of the compressed pulse by controlling the incident pulse spectrum in the CPA laser system with glass amplifiers as shown in Fig.3.5.

A incident pulse with the Gaussian shape as shown by a dotted line in Fig.3.5(a) is moderated through the amplification in the glass amplifiers due to non-uniformity of gain spectrum. Then the amplified spectrum become to distort form Gaussian shape (dotted line in Fig.3.5(b)) and the compressed pulse has a pedestal (dotted line in Fig.3.5(c)). However, if the amplified spectrum is close to the Gaussian shape, no pedestal can be expected on the compressed pulse. If the incident pulse spectrum is controlled as shown by a solid line

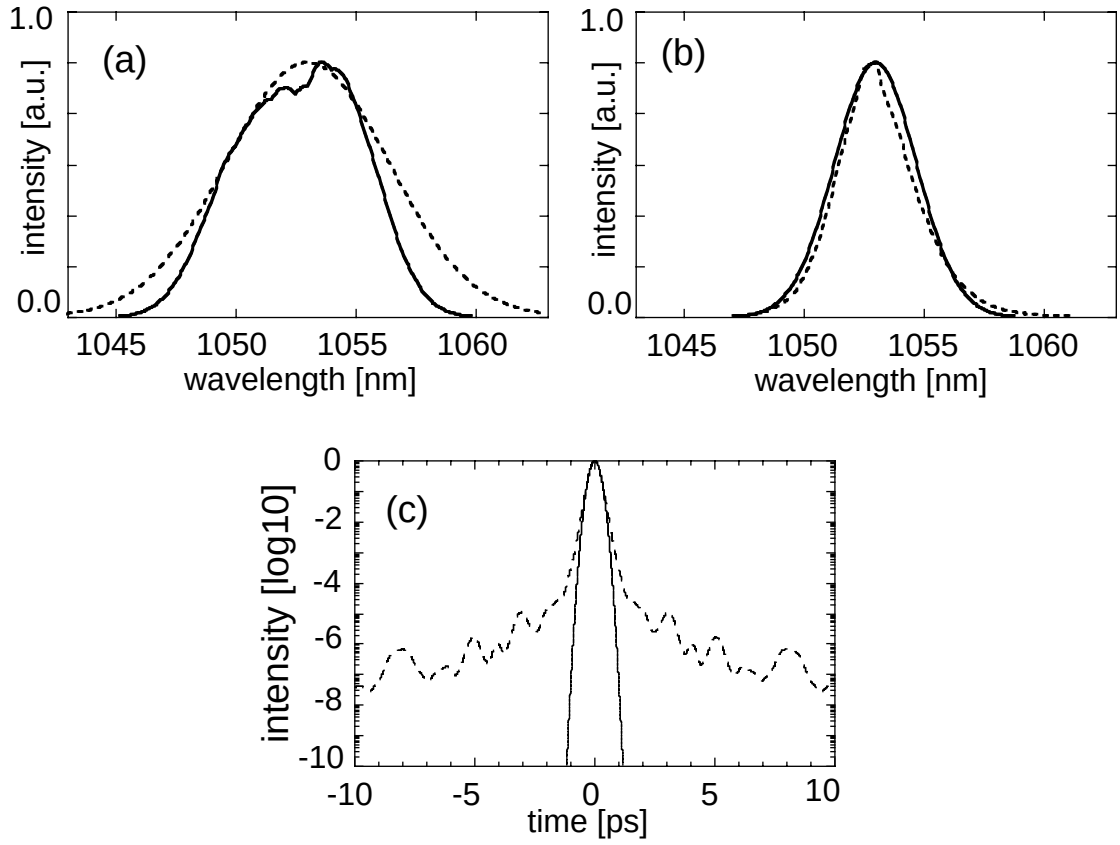

Figure 3.5: Outline of pedestal control. (a) Incident spectra of controlled (solid line) and no-controlled (dotted line) pulse. (b) Amplified spectra of controlled (solid line) and no-controlled (dotted line) pulse. (c) Compressed pulse shape of controlled (solid line) and no-controlled (dotted line) pulse in a logarithmic scale.

in Fig.3.5(a) taking account of the spectral response of the laser system, the amplified pulse spectrum becomes close to Gaussian shape as shown by a solid line in Fig.3.5(b). In the result, the compressed pulse, as shown by a solid line in Fig.3.5(c), also become close to the Gaussian shape. The intensity ratio of the pedestal at 1ps before the peak of the main pulse of the compressed pulse can be decrease from 10^{-4} (Gaussian) to 10^{-7} (controlled spectrum).

The experimental demonstration for pedestal level control is shown in Fig.3.6. We controlled the incident spectrum to reduce the spectral intensities of higher wavelength (black solid line) slightly from the center compared with no-controlled spectrum (gray solid line) as shown in Fig.3.6(a). The amplified spectrum of controlled (black solid line) and no-controlled (gray solid line) pulse are shown in Fig.3.6(b).

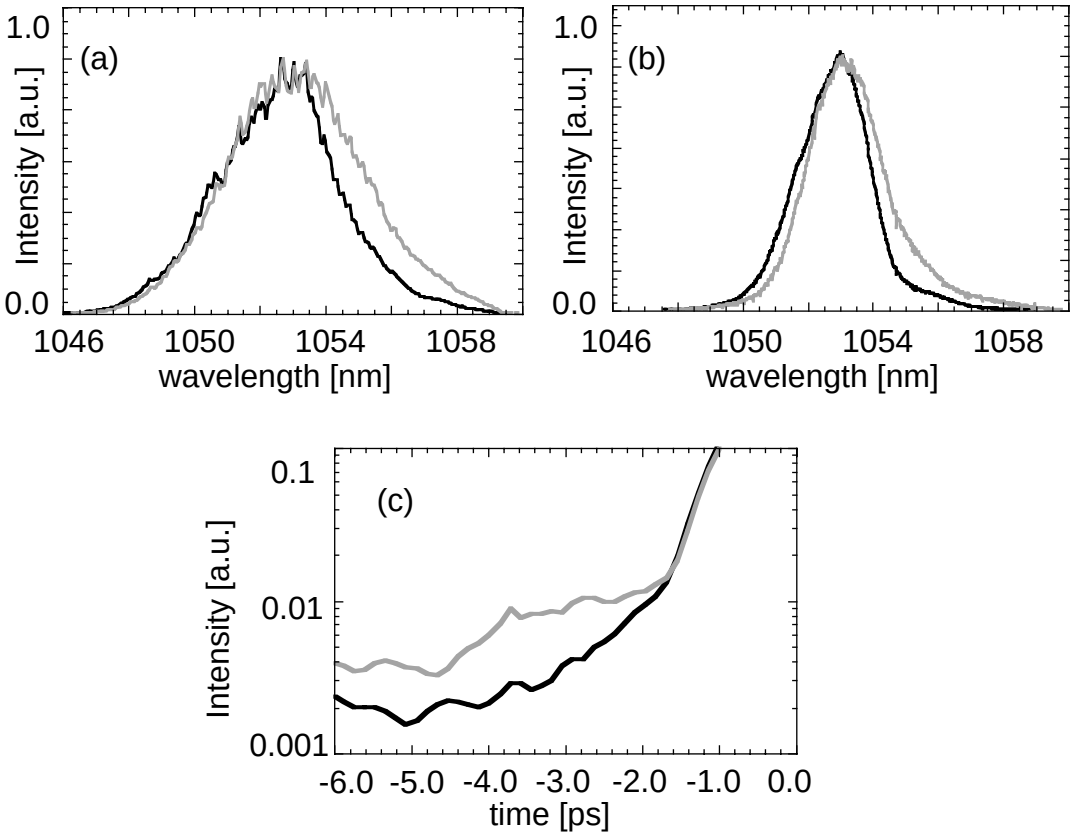

Figure 3.6: Experimental results of pedestal control. (a) The incident spectrum of controlled (black solid line) and no-controlled pulse (gray solid line). (b) The amplified spectrum of controlled (black solid line) and no-controlled pulse (gray solid line). (c) The pedestal level in the compressed pulse of controlled incident (black solid line) and no-controlled (gray solid line) pulse in a logarithmic scale, which are also deconvoluted by the pulse shape detected by 2nd-order autocorrelator with the amplified spectral shape.

Fitting of the amplified spectrum to Gaussian distribution is estimated by the value of a χ^2, represented as a dimension of a spectral distortion from the Gaussian shape [13],

resulting in 0.62 of controlled spectrum and 0.83 of no-controlled spectrum, respectively. These results indicate the controlled spectrum is closer to the Gaussian shape compared with no-controlled spectrum. Fig.3.6(c) shows the pedestal level on the compressed pulse of controlled spectrum (black solid line) and no-controlled spectrum (gray solid line) in a logarithmic scale from 6.0ps before to the peak of the main pulse. These compressed pulses are also deconvoluted the pulse shape detected by 2nd-order autocorrelator with the spectrum. In the result, the half of pedestal was obtained on the controlled pulse compared with that on the no-controlled pulse. The pedestal level will be more small by precise control of the incident pulse spectrum to close the χ^2 to zero in the amplified pulse spectrum.

3.6 Shortening of the pulse duration

Shortening of the compressed pulse duration is also interesting control of the incident pulse spectrum against gain narrowing in the glass amplifier system. Incident pulse with no-controlled spectrum which has a spectral width of 8nm (dotted line in Fig.3.7(a)) will narrow to be 3nm of the spectral width (dotted line in Fig.3.7(b)) through the 2×10^4 times amplified gain in the system. The expected pulse duration of the compressed pulse is near 500fs (dotted line in Fig.3.7(c)) from the Fourier transform of the spectral shape of the amplified pulse. Then the gain narrowing become a significant problem to reduce the pulse duration of the compressed pulse and increase laser out-put power.

However, if the incident spectrum has a shape of decreasing peak intensity as shown by solid line in Fig.3.7(a), the spectral width of amplified pulse as shown by solid line in Fig.3.7(b) will be wider (5nm spectral width) than that of no-controlled pulse due to the suppression of the gain narrowing. It is because the spectral shape of the controlled pulse prevents to rise only the spectral intensity near the central wavelength more and more taking account of the gain spectrum of the amplifier. In the results, the compressed pulse duration of the controlled pulse as shown by solid line in Fig.3.7(c) will be shorter than that of no-controlled one. Dipping the center part of the incident pulse spectrum to be 20% of the original spectral peak intensity shortens the pulse duration to be 300fs even at higher amplification rate of 3×10^4 (no controlled pulse : 500fs at 2×10^4 times amplification).

The pulse duration of the compressed pulse is reduced not by simply broadening spectral width of the incident pulse but by this spectral control to the incident pulse. The incident pulse with Gaussian shape as shown by solid line in Fig.3.8 having wider spectral width (14nm) compared with the original pulse spectrum as shown by dotted line in Fig.3.7(a) will be narrowed to be about 3nm spectral width through 2×10^4 amplification as shown by dotted line in Fig.3.8 because of strong gain narrowing, therefore, expected pulse duration is similar as that of dotted line in Fig.3.7(c).

In the result, the spectral control of decreasing peak intensity is more effective to shorten the pulse duration of the compressed pulse. In our calculation, at more than 1.5×10^4 times gain amplification in glass amplifier, no-controlled pulse spectrum over 10nm spectral width (FWHM) will be narrowed to be less 3.0nm and not be changed so much at more higher gain amplification.

The compressed pulse duration of the controlled pulse also depends on the spectral

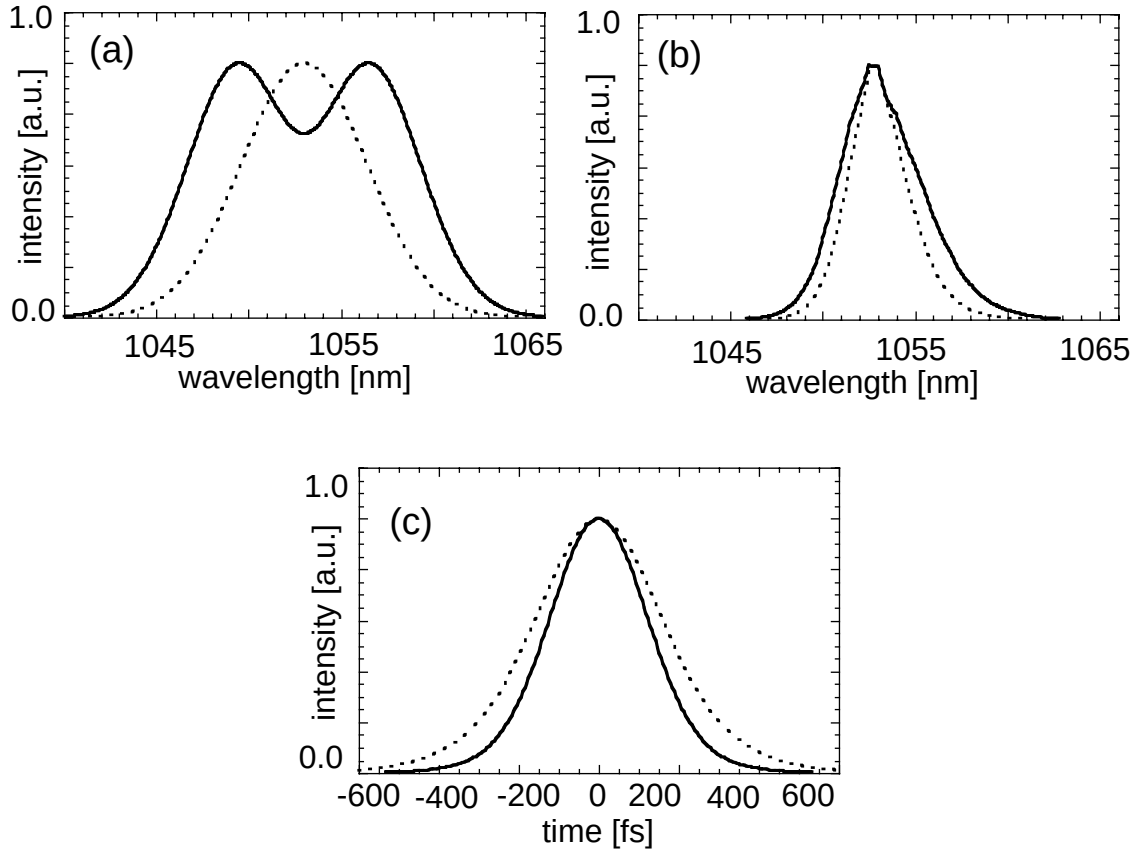

Figure 3.7: Outline of shortening of the compressed pulse duration. (a) Incident spectra of controlled (solid line) and no-controlled (dotted line) pulse. (b) Amplified spectra of controlled (solid line) and no-controlled (dotted line) pulse. (c) Compressed pulse shape of controlled (solid line) and no-controlled (dotted line) pulse.

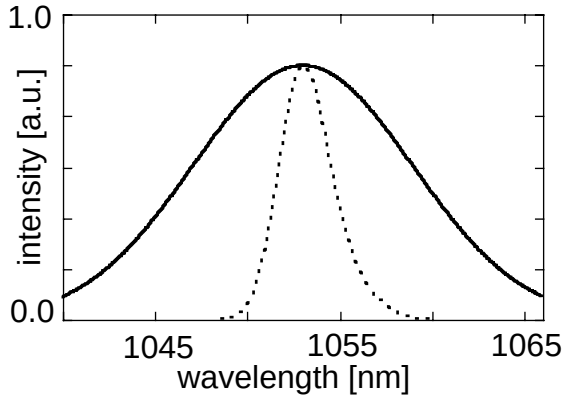

Figure 3.8: The laser amplification with the wider spectral width in the incident pulse spectrum compared with the original Gaussian pulse as shown by dotted line in Fig.3.7(a). The incident pulse having a Gaussian shape (solid line) with appearance spectral width (14nm) as same as the controlled pulse spectrum (solid line in Fig.3.7(a)).

shape of the dip at the center of spectrum, i.e. spectral separation between the double peak and intensity depth of the dip in the incident spectrum as shown by solid line in Fig.3.7(a). Figure 3.9(a) shows the pulse duration (FWHM) as functions of the spectral separation between the double peaks and the intensity ratio of the dip height to the peak of the original Gaussian pulse in the incident spectrum. The spectral separation width is normalized by the spectral width (FWHM : 8nm) of the original spectrum shape. The amplification rate is slightly changed to obtain the amplified laser energy at 20J because of difference of the incident pulse energies due to the decrease of spectral peak intensity, whose fluctuations are within 20-30%. The pulse duration decreases in increase of the spectral separation and the intensity ratio in the controlled incident pulse, for example, near 250fs pulse duration can be expected by controlling the incident spectrum with 0.8 of separation width per spectral width and 0.0 of intensity ratio.

However, the pedestal level in the compressed pulse is increased at the same time as shortening of the pulse duration. Figure 3.9(b) shows the pedestal intensity ratio to the main pulse at 1ps before the peak of the main pulse as functions of the spectral separation of the double peak and the intensity ratio of the dip to the double peak of the controlled incident pulse. Increasing the spectral separation and the intensity ratio also affects the spectral shape of amplified pulse to be further from the ideal Gaussian shape, resulting in increase of the pedestal level. Therefore, the pulse duration can be shorten to about 350fs if the pedestal level will be kept at the same level with that of the non-controlled pulse when the incident pulse has 0.8 separation width per spectral width and 0.3 intensity ratio of the dip.

The typical experimental spectra and pulse shape of the controlled pulse to shorten pulse duration are shown in Fig.3.10.

Black solid line in Figure 3.10(a) shows incident pulse spectrum of the controlled pulse having double spectral peaks. The controlled spectrum had 0.8 separation width between

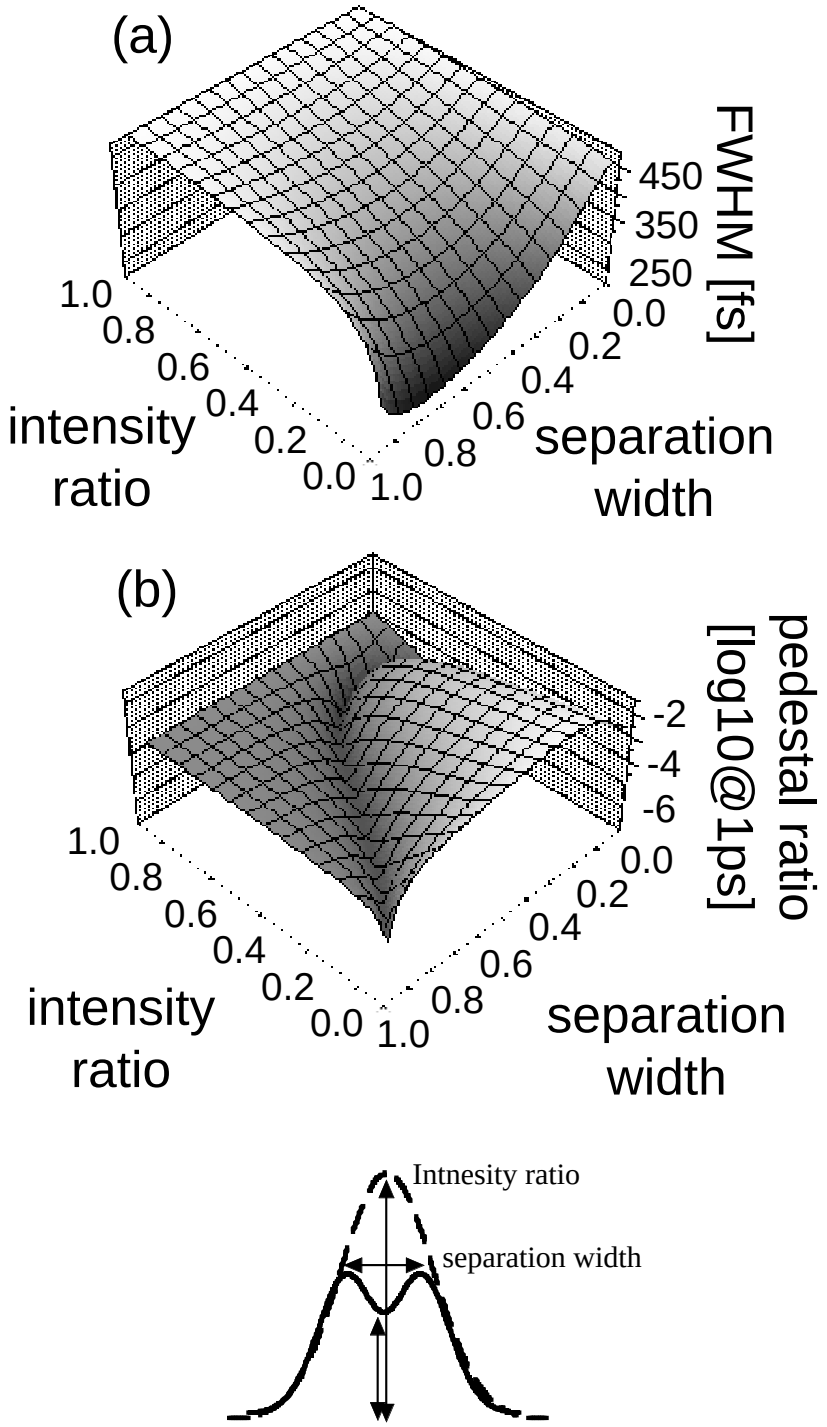

Figure 3.9: (a)Temporal duration (FWHM) in the compressed pulse and (b)pedestal level at 1ps before from pulse center to peak intensity. Right axis shows the spectral separation width between the double peaks in the incident pulse spectrum divided by the spectral width (FWHM). On the other hand, left axis shows intensity ratio of the dips at the spectral center to the peaks. In the calculation, laser energy is fixed at 20J.

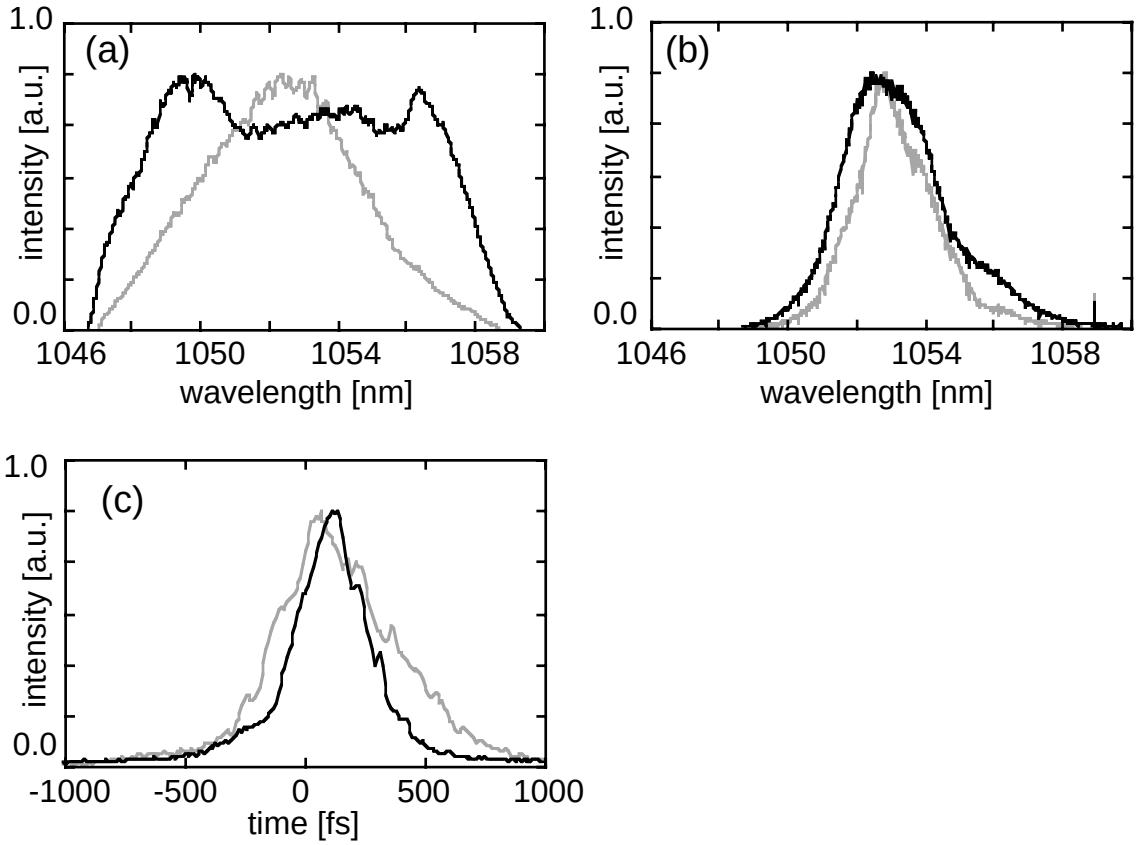

Figure 3.10: A typical experimental results for pulse duration shortening. (a) The incident spectra; controlled double peak spectrum (black solid line) and original spectrum (doted line) as a no-controlled pulse, respectively. (b) Amplified pulse spectra; controlled double peak spectrum (black solid line) and original spectrum (doted line) as a no-controlled pulse, respectively. (c) The compressed pulse shape with pulse duration of 320fs (controlled pulse:black solid line) and 552fs (original incident pulse:gray solid line) at a laser energy of 20J.

two peaks per spectral width (FWHM) of the no-controlled spectrum and 0.4 intensity ratio of spectral dip to peak intensity of the no-controlled pulse. Respectively, incident spectrum of no-controlled pulse with 4.1nm spectral width (FWHM) is also shown as gray solid line in Fig.3.10(a). Significant narrowing was seen on the amplified spectrum of the no-controlled pulse as shown by gray solid line in Fig.3.10(b) with a spectral width (FWHM) of 3.1nm at a laser energy of 20J, resulting in a pulse duration of 533fs on the compressed pulse as shown in gray solid line in Fig.3.10(c). On the other hand, controlled pulse was only narrowed to be 4.0nm (black solid line in Fig.3.10(b)), resulting in shortening the 320fs pulse duration (black solid line in Fig.3.10(c)). In the results, the laser power was increased from 28TW to 63TW at the 20J amplification with the spectral control.

Experimental results of compressed pulse duration changing spectral intensity ratio of spectral dip peak in the incident pulse were shown in Fig.3.11 as circles.

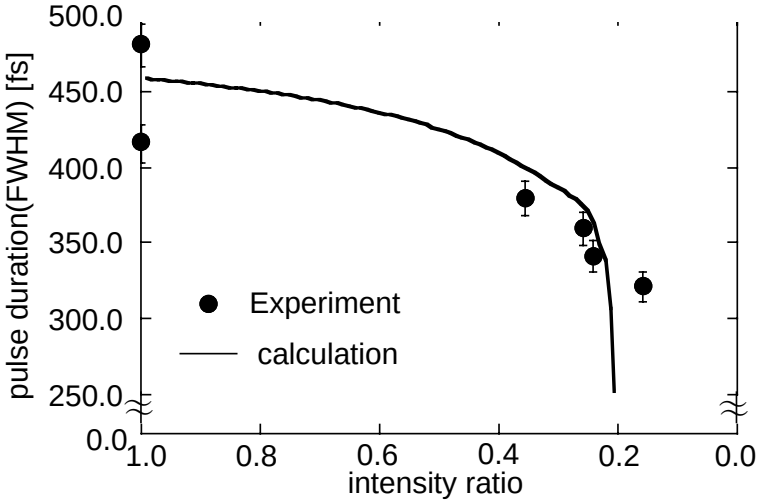

Figure 3.11: Summary of shortening of the compressed pulse duration. The experimental results of the pulse duration are shown by solid circles changing the intensity height of the spectral dips between the two peaks as shown by solid line in Fig.3.7(a) to the peaks in the incident pulse spectrum. The spectral separation width between two peaks divided by the spectral width (FWHM) in the incident pulse spectrum is fixed at 0.8. The solid line shows calculated results of the pulse duration changing the intensity height of the dips in the incident spectrum with an original spectral width of 6nm (FWHM). Other calculation conditions such as separation width or laser energy are same as the experimental conditions.

All the separation width between two peaks to the spectral width (FWHM) was fixed at 0.8. Amplified energy of all the experimental data were between 20J and 15J. The calculation of the compressed pulse duration changing spectral intensity ratio of spectral dip peak in the incident pulse were shown by solid line in Fig.3.11 at amplified energy of 15J, respectively. The pulse duration in the compressed pulse was decreased in increase of the intensity ratio of the spectral dip to the peak as same as the calculation results.

3.7 Summary

We have demonstrated compressed pulse shaping with incident spectral control using a spatial modulation filter at the glass amplifiers system coupled with Ti:sapphire front end. The spectrum was controlled with the spatial gradient transmission filter changing spatial modulation into the pulse stretcher. The pulse shaping was applied to control the prepulse, reduce the pedestal and shorten the pulse duration on the compressed pulse shape in experiment and simulation. We showed prepulse control with various spectral controls such as spectral dips control in the incident pulse spectrum. In the result, changing the separation width of the spectral dips controlled prepulse timing. Pedestal control was also performed by the spectral control, resulting in obtaining half of pedestal level in the compressed pulse compared with the no-controlled pulse. By the spectral control for the shortening the pulse duration, the chirped pulse amplification providing a 40TW/500fs laser pulse was improved to be a 70TW/300fs system. In these method, various pulse shaping can be performed only changing the spatial modulation of the transmission on the filter. In addition, these pulse shaping can be also performed at the same time, i.e. control of the shortening the pulse duration with less-pedestal in the compressed pulse and so on.

Reference

[1] B. C. Stuart, M. D. Perry, J. Miller, G. Tietbohl, S. Herman, J. A. Britten, C. Brown, D. Pennington, V. Yanovsky, and K. Wharton, Opt. Lett. **22**, 242 (1997).

[2] M. Tabak, J. Hammer, M. E. Glinsky, W. L. Kruer, S. C. Wilks, J. Woodworth, E. M. Campbell, M. D. Perry, and R. J. Mason, Phys. Plasmas, **1**, 1626 (1994).

[3] L. M. Corbunov, and V. I. Kirsanov, Zh. Eksp. Teor. Fiz **93**, 509(1987): Sov. Phys. JETP **66**, 290(1987).

[4] H. Hamster et al., Phys. Rev. Lett **71**, 2725 (1993).

[5] H. Daido et al, J. Opt. Soc. Am. B **11**, 280 (1994).

[6] J.Z ang et al, Phys. Rev. Lett **74**, 1335 (1995).

[7] C. Rouyer, N. Blanchot, L. Allais, E. Mazataud, J. L. Miquel, M. Nail, A. Pierre, C. Sauteret, and A. Migus, J. Opt. Soc. Am. B **13**, 55 (1996).

[8] P. Loza-Alvarez, D. T. Reid, P. Faller, M. Ebrahimzadeh, and W. Sibbett, Opt. Lett **24**, 1071(1999)

[9] C. P. J. Barty, T. Guo, C. Le Blanc, F. Raksi, C. Rose-Petruck, J. Squier, K. R. Wilson, V. V. Yakovlev, and K. Yamakawa, Opt. Lett **21**, 668 (1996).

[10] M. M. Wefers, K. A. Nelson, and A. M. Weiner, Opt. Lett **21**, 746 (1996).

[11] A. M. Weiner, D. E. Leaird, J. S. Patel, and J. R. Wullert II, IEEE. J. Quantum Electronics **28**, 908 (1992).

[12] Y. Kitagawa et al., Fusion Engineering and Design **44**, 261 (1999).

[13] χ^2 is represented by $\chi^2 = \sum_i^N (\frac{y_i - f(x_i)}{\sigma_i})^{\frac{1}{2}}$, where $f(x_i)$ is the Gaussian distribution, the y_i the actual value of the data to fit and the σ_i weight for the data.

Chapter 4

Solid-dense plasma heating by high energy density electrons

4.1 Introduction

Recent progresses in ultra intense laser technology, generation of energetic electrons in MeV ranges has been reported in the laser plasma interaction [1, 2]. These energetic electrons are interested as high-energy electron sources in many applications such as the fast ignitor in Inertial confinement fusion research and generation of a high brightness γ ray source.

However, the propagation of energetic electron generated in ultra-intense laser-plasma interactions into the dense plasma has been not evaluated yet. The current propagation into solid dense plasmas is restricted in the alfvén limit, giving $17000\gamma\beta$ [A], where $\gamma = 1/\sqrt{1-(v/c)^2}$ and $\beta = v/c$. If the electron current generated in the ultra-intense laser-plasma interactions become over the limit, the current might be destroyed due to magnetically self-pinching and blanched off in filaments. The energy of accelerated electrons generated in ultra-intense laser-plasma interactions is estimated in $kT_e = 100\left(\frac{I}{10^{17}W/cm^2}\right)^{1/3}$keV [3] or $kT_e = 511[(1+(I/10^{18}(W/cm^2))/1.37)^{1/2}-1]$keV [4], resulting in the electron velocity of 0.85c or 0.93c at the intensity of $10^{19}W/cm^2$. In both model, the alfvén limit is order of 10^4A, which is almost 10^3 times smaller than the electron current assuming a solid density. In addition, if the current with a cylinder of radius ($\sim 10\mu$m) penetrated a distance $\sim$ a few tens μm into the solid dense plasma, the energy in the magnetic field would be of the order of kJ, which is larger than incident laser energy of ultra-short pulse laser, indicating energetically impossible [5].

As another possibility of the propagation, the fast electrons propagate in the dense plasma retaining the high density due to the return current to cancel the magnetic field generated by the fast electrons. The electron propagation gives the significant influence on the plasma heating, therefore, study of the electron propagation in the dense plasma is significantly critical point for the fast ignitor concept to heat up the core fuel plasma by the fast electrons.

These propagation processes could be affected by the current density of the fast electrons, which is different with the polarization of the irradiated laser. For s-polarization, the electrons are accelerated by the $J \times B$ heating [6] in the laser direction. On the other

hand, p-polarized laser accelerates the electron in the direction of rear normal of the target surface due to the strong Brunel absorption [7] as shown in Appendix B. From the particle-in-cell(PIC) simulation, the laser absorption for p-polarization is three times than that for p-polarization [8]. In addition, the absorption could be changed by the density scale of the plasma or by laser incidence angle in the p-polarization condition. Therefore, condition of the laser plasma interaction will affect the current density, resulting in affecting on the plasma heating.

In this chapter, I describe the plasma heating by high dense energetic electrons in ultra-intense laser-plasma interactions. First section shows theoretical prospects for transport of the high dense energetic electrons. The second shows the plasma heating by the fast electrons with the x-ray and neutron spectroscopy. The third section is about the propagation of the fast electron in the dense plasma. The last is summary.

4.2 Plasma heating by the fast electrons

4.2.1 Experiment setup

For the purpose of the measurement of the plasma temperature heated by the electron current, I performed the experiment using GEKKO-MII CPA short pulse laser system as mentioned in chapter 2, changing the laser incidence conditions such as plasma density scale and laser incident angles. The laser conditions in this experiment were described in Table 4.1.

Laser energy	20J
Pulse duration	500fs
Focal intensity	$10^{19} W/cm^2$
Polarization	p-polarization
Incident angle	$10°, 20° and 45°$
Prepulse level	$10^{-3} \sim 10^{-5}$
	(6.5ns and 13.0ns before)

Table 4.1: Laser condition for electron propagation experiment

In this experiment, the laser polarization was used the p-polarization to create higher density electron current via Brunel absorption compared with the s-polarization via $J \times B$ heating. Furthermore, the laser incident angle and prepulse level to create the preformed plasma were changed to create the dense current because the Brunel absorption depends on the incident angle and plasma density scale.

To measure the fast electrons and the plasma temperature heated by the electron current, different types of detectors were used in the experiment in Table 4.2.

The X-ray spectrometer is purposed to measure the plasma temperature and density heated by the fast electron current. The obtained X-ray spectrum is analyzed by the "FLY" code [10] to compare a signal intensity and spectral width of the characteristic X-ray with the obtained spectrum. The detector was used Bent crystal spectrometer, which has also one-dimensional spatial resolution. The detection range of the detector is $0.55 \sim 0.65nm$

Detection method	Measurement purpose	Detection subject
X-ray spectroscopy	Plasma temperature and density	Characteristic X-ray
X-ray imaging	2D imaging of radiation	X-ray 2D image
Visible-ray sampling imaging	from the fast electrons	Visible-ray 2D image
Electron spectroscopy	Electron temperature	Fast electrons
Neutron spectroscopy	Plasma temperature	Thermal neutrons

Detector	Detection range
Bent crystal spectrometer	$1.9 \sim 2.2keV$
X-ray penumbra camera	$1 \sim 30keV$
High speed sampling camera (HISAC)	(wavelength) $400 \sim 700nm$
Electron spectrometer	$100keV \sim 10MeV$
Plastic scintillator	ł20MeV

Table 4.2: detector

with the spectral resolution of $10^{-3}nm$ and the spatial resolution of $200\mu m$. I obtained the heated temperature of plasmas to compare the intensity ratio between H-like line (0.574nm) and He-like line (0.631nm) of the Aluminum.

The X-ray imaging and visible-ray sampling imaging are each purposed to measure 2-D image of radiation generated by the electron current at the rear side of the target. For the X-ray imaging, I used X-ray penumbra camera, which has a detection range of $1 \sim 30keV$. On the other hand, a high speed imaging sampling camera (HISAC) system was used as the visible-ray detector, which has a detection range of $400 \sim 700nm$ with the about 20nm spatial resolution and 40 ps temporal resolution.

The electron spectrometer is used to measure the fast electron from the target rear side to bend the electron motion with the magnet in the detector. Imaging plate [10] were used to obtain the electron track in this detector. The detection range of the electron energy is about 100keV∼10MeV.

The neutron spectrometer is purposed to measure the 2.45MeV thermal neutron from the thermal fusion reaction in the heated plasma by the electron current. The plastic scintillators using a time of flight (T.O.F.) method detect the neutron spectra from the different view angles to identify the 2.45MeV thermal neutron signal. The detection range of the neutron energy is under 20MeV with the energy resolution of 100keV.

The target was designed as three layer consisted of Al-CD-Al. The front aluminum layer is placed to generate the fast electron effectively and to protect the generation of beam fusion neutron. The middle layer of CD (deuterated plastic) is placed for thermal neutron generation to measure the plasma temperature. The fast electrons can emit X-ray and visible-ray effectively at the rear side of the Al. Each of thickness is fixed at 10μm, 50μm and 1μm, resulting in $\rho R \sim 7.7 \times 10^{-3} g/cm^2$. The laser incident angle to the target was changed to control the current of the fast electrons via the Brunel absorption for p-polarization, which depends on also the plasma density scale.

4.2.2 Experimental results

The electron spectrometer shows the dependence of incident angles on the electron spectrum with the small density length ($\sim 3\mu$m) as shown in Figure 4.1.

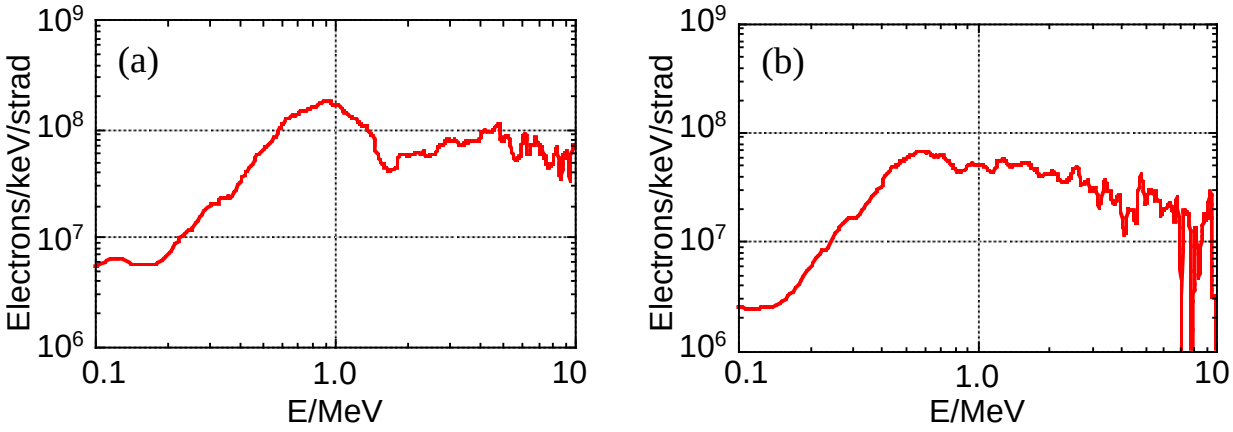

Figure 4.1: The electron spectrum at (a)10° incidence and (b)45° incidence detected at the 45° from the rear target normal.

Figure 4.1(a) was the electron spectrum when the laser irradiated small-scale length ($\sim 3\mu m$) plasma at the intensity of $10^{19} W/cm^2$ with 10° incidence to the target normal. On the other hand, Fig.4.1(b) was the electron spectrum at the 45° incidence. It is clear that both the electron temperature and the accelerated electron number at 10° incidence was larger than that at the 45° incidence. In the results, the fast electrons at the 10° incidence were effectively generated compared with that at the 45° incidence.

Furthermore, clear difference of the laser incidence on the neutron spectrum was also observed. At the 20° laser incidence, a thermal neutron peak was observed at the 2.45MeV in the neutron spectrum detected at the detection angle of 23.5° from the rear target normal as shown in Fig.4.2(a). On the other hand, no signals were observed in the spectrum at the 45° incidence as shown in Fig.4.2(b). These results indicate that the fast electrons at the 20° incidence heated up the plasma at higher temperature compared with that at the 45° incidence.

To investigate an influence of the laser absorption on the plasma heating, neutron spectra were observed changing the density scale of plasmas and laser incident angles. Figure 4.3 shows a dependence of the plasma density scale on the neutron counts at the 2.45MeV peak in the neutron spectra at the intensities ranging on $0.7 \sim 1.0 \times 10^{19} W/cm^2$ with laser incidence of 20° incidence.

The neutron peak at 2.45MeV in the spectra could be observed in the interactions with small-scale length ($\leq 5\mu m$) plasma. On the other hand, no neutron signal in the interactions with large-scale length ($\geq 10\mu m$) plasma were observed in the spectra. These results that the plasma heating increased in decrease of the plasma density scale is consist with the Brunel absorption, which become stronger in the smaller density scale of plasmas [11].

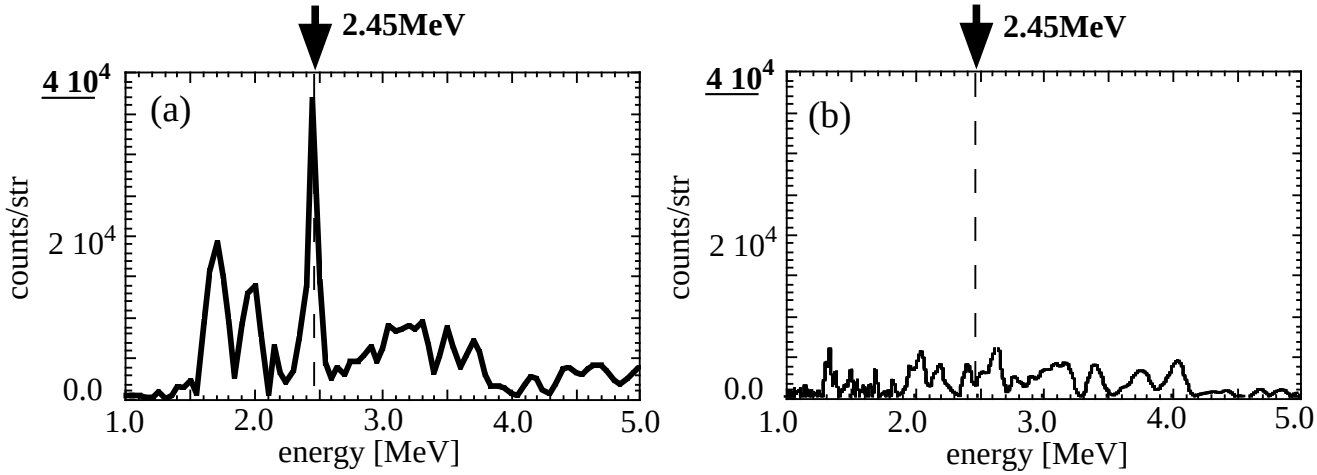

Figure 4.2: Laser incidence dependence on the neutron spectra. (a) The neutron spectrum at the 20° laser incidence. (b) The neutron spectrum the 45° laser incidence.

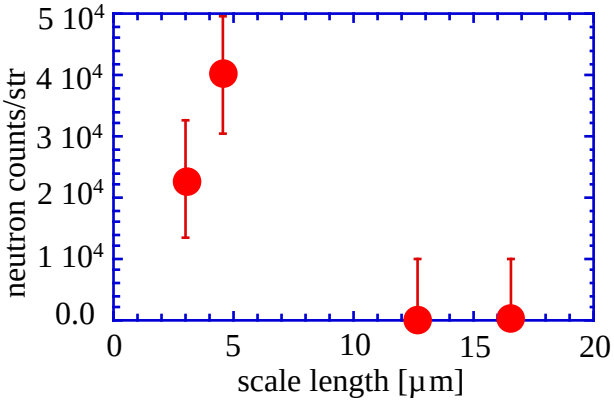

Figure 4.3: Density scale dependence on the thermal neutron counts. The laser incident angle was 20° with the *p*-polarization.

A laser incident angle dependence on the 2.45MeV neutron peak in the neutron spectra is shown in Fig.4.4(a). As the experimental condition, the density scale of plasma was relatively small ($\leq 5\mu m$). Other conditions such as laser intensity were same as Fig.4.3.

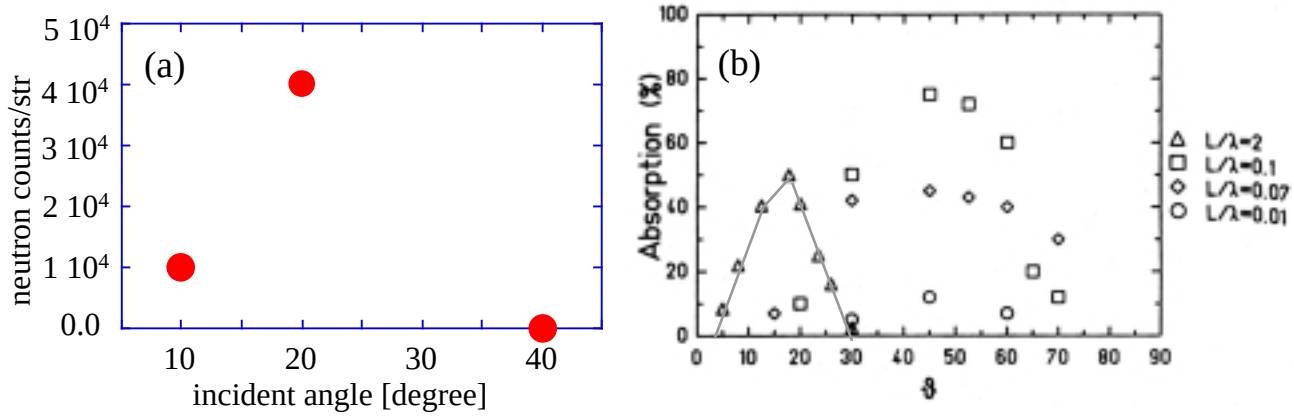

Figure 4.4: (a) Dependence of the laser incident angle on the thermal neutron counts in the observed neutron spectra. (b) Dependence of the laser incident angle with different scale length from the particle-in-cell(PIC) simulation [11].

The neutron counts could be observed at the laser incidences of 10° and 20° . On the other hand, there was no neutron signals at the 45° incidence. The dependence of the laser incidence on the Brunel absorption was also investigated in the PIC simulation [11] at the intensity of $10^{16}W/cm^2\mu m^2$. Fig.4.4 shows the laser absorption for p-polarization become strongest at the incident angle of 45° with the absorption rate of 80% in the case that the density scale length is close to the 0.1λ. On the other hand, when the scale length increases up to L/λ ~2, the strongest absorption can be obtained at the 20° laser incidence with the absorption rate of 60%. However, the absorption at the 45° incidence with L/λ ~2 will decrease in ~0%. The simulation results are consistent with the experimental results of the laser incident dependence on the neutron count. Therefore, plasma is heated at higher temperature with increase in the laser intensity and absorption rate, which will generate high-density energetic electrons in the ultra-intense laser-plasma interactions.

A temperature of the heated plasma can be estimated by the neutron signal at the 2.45MeV. Assuming a Gaussian shape at the 2.45MeV in the neutron spectrum, the ion temperature is given

$$T_i[keV] = \left(\frac{\Delta E_{FWHM}[keV]}{C}\right)^2, \tag{4.1}$$

where E_{FWHM} is the spectral width of the neutron signal at the 2.45MeV and C the constant given by $82.48[keV^{1/2}]$ for D-D neutron. To fit the Gaussian shape on the peak in the neutron spectrum as shown in Fig.4.2, the energy width of the neutron spectrum was 53 keV (FWHM), resulting in the ion temperature of 410eV.

The dependence of the laser incidence on the plasma heating was also obtained by the X-ray spectrometer. Figure 4.5 shows the spectral image detected by the X-ray CCD at the target rear side.

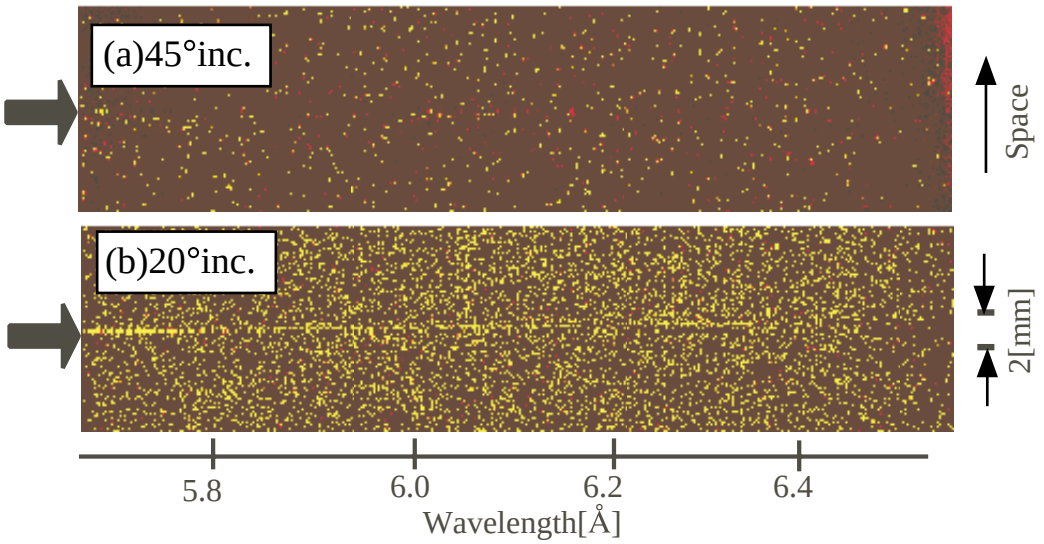

Figure 4.5: The spatial-spectral image of the X-ray spectrometer detected at the target rear side. Upper image was detected at the 45° laser incidence and lower one is at the 20° incidence. Experimental conditions are same as Fig.4.3.

There was no signal in the upper image at the 45° laser incidence. On the other hand, the straight line can be observed in the lower image, which is at the 20° incidence. These signals only observed when the 2.45MeV neutron peak signal was also detected in the neutron spectra. Unfortunately, the straight signal level is too small to distinguish from the background noise (which is about half of the signals), resulting in difficulty of spectral analyze of the characteristic peaks. However, this signal suggests that the plasma was heated at the keV level by the high dense energetic electrons.

In these results, there was a clear difference on the results changing the laser incident conditions. The electron spectra show the electrons are accelerated to higher energy when the laser absorption become strong. Furthermore, the neutron spectrum and the image of X-ray spectrometer indicate that the plasma is heated at higher energy with increase of the laser absorption of the Brunel heating. Therefore, the current of the fast electrons become more intense at the 20° incidence interacted with small density scale, resulting in plasma heating of 410keV.

4.3 Propagation of fast electrons in dense plasmas

The electron current can be estimated from the heated temperature. The total energy of the heated plasmas as a function of propagation distance of the electrons ϵ(x) is given [12]

$$\epsilon(x) = \frac{T_{electron} \cdot \left(\frac{x}{l}\right)^{-0.1}}{l \cdot S \cdot \rho} \exp\left(-1.9\left(\frac{x}{l}\right)^{1/3}\right) \quad [J/g], \tag{4.2}$$

$$where \quad l = 9 \times T_{electron}[keV] \cdot \frac{10^{21}}{n_i(cm^{-3})} \cdot \frac{10^{-4}}{[Z(Z+Z^2)]^{1/2}} \quad [cm], \tag{4.3}$$

$T_{electron}$ the energy of energetic electrons, x the target thickness, S the heating area, ρ the density of the plasma, n_i the number density of the plasma and Z the atomic number. Assuming the electron current is collimated within a laser focal spot($\sim 20\mu m$) through out the target with the electron temperature given by $T_e = 511[(1+10^{19}W/cm^2/10^{18}W/cm^2/1.37)^{1/2}-1]keV$ [4], the electron current which need to heat the plasma ($\rho R \sim 7.7 \times 10^{-3} g/cm^2$) up to 410eV is about $1.5 \times 10^7 A$.

On the other hand, the electron current can be also estimated from the laser absorption. Assuming the energy conversion is 20∼50% for p-polarization at $10^{19}W/cm^2$ [4] with the laser energy of 20J, the electron current become $2 \sim 4 \times 10^7 A$, resulting in consistent with the current estimated the heated temperature.

These electron current are about 10^3 times larger than the alfvén limit. Therefore, high dense energetic electrons, which heat the plasma up to 400eV, could not propagate in the plasmas. As one of the possibilities to propagate and heat up the plasma, the high-density energetic electrons might propagate with return current in the plasmas to cancel the magnetic field, which acts a pinching force of the fast electrons and destroyed the current propagation [13].

However, density effect on the electron propagation become important in such a high current ($\sim 10^7 A$). The magnetic field generated by the spatial distribution of the dense electron current is given by

$$\frac{\partial \mathbf{B}}{\partial t} = \nabla \times \eta \mathbf{j}_f - \nabla \times \left(\frac{\eta}{\mu_0} \nabla \times \mathbf{B} \right), \tag{4.4}$$

where η is the resistivity, $\mathbf{j}_f$ the current density of the fast electrons and μ_0 the magnetic permeability in vacuum. The first and second term of the right side of the equation show each the generation and diffusion of the magnetic field. Assuming a rotational symmetry along with the electron acceleration direction as z-axis ($j = j_z \exp(-r^2/r_0^2)$), the magnetic field on cylindrical system is given by

$$\frac{\partial \mathbf{B}}{\partial t} = -\eta \frac{\partial j_r}{\partial r} - (\nabla \eta)_r j_z. \tag{4.5}$$

The first term become higher with the current density of the fast electrons assuming the fast electrons are collimated within a spot radius. The high gradient of the current density in radial direction generates a strong negative magnetic field, which acts to pinch the fast electrons. Therefore, the electron current could be blanched off in filaments due to the magnetic self-focusing. If the current densities are over $10^7 A$, the negative magnetic field become equivalent to the magnetic field generated by the electron propagation ($B = I/2\pi r \sim$ a few handret MG).

On the other hand, the local plasma heating through the Ohmic heating by the fast electrons reduces a plasma resistivity locally [14]. Therefore, the low resistivity channel along the fast electron direction creates strong positive magnetic field, given by the second term of the right side in the eq.4.5. The positive magnetic field could prevent the self-pinching of the electron current, which is generated from the first term of the eq.4.5.

In the ultra-intense laser-plasma interactions, the resistivity in the solid dense plasma can't use the ordinary Spizter-Härm model due to resistivity saturation [16]. Therefore the an experimental fitting curve must be used as the resistivity in the eq.4.5 [15], given

$$\eta = \frac{1}{1.0 \times 10^6 (T_p)^{-1} + 170 (T_p)^{3/2} + 3.0 \times 10^5} \Omega m, \tag{4.6}$$

where T_p is the background temperature in eV.

Figure 4.6 shows the magnetic field in the radius direction with the fast electron energy of 1MeV and the density of near solid density changing the heated plasma temperature and current density.

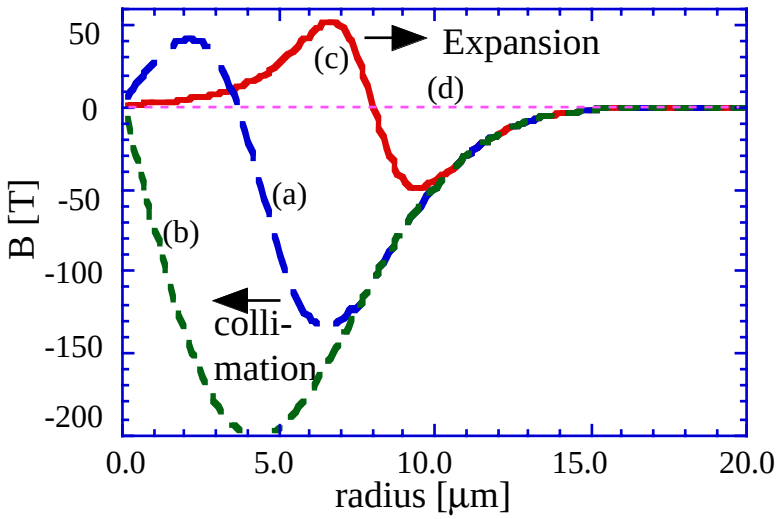

Figure 4.6: The magnetic field in radius direction with the fast electron energy of 1MeV and the density of near solid density changing the heated plasma temperature and current density. (a) $T_{plasma} = 0.1$eV and $j_{fast} = 1.5 \times 10^7 A$. (b) $T_{plasma} = 24$eV and $j_{fast} = 1.5 \times 10^7 A$. (c) $T_{plasma} = 400$eV and $j_{fast} = 1.5 \times 10^7 A$. (d) $T_{plasma} = 400$eV and $j_{fast} = 1.5 \times 10^5 A$.

If the heated temperature of the plasma is relatively low ($\simeq 0.1eV$), only the negative magnetic field is generated due to the high current density ($\simeq 1.5 \times 10^7 A$), resulting in self-pinching of the fast electron current. The positive magnetic field is increased in the temperature of the heated plasma. At the temperature of 400eV, the norm of the positive magnetic field become equivalent to that of the negative magnetic field, which allows the propagation of the electron current with the high current density. On the other hand, the low electron current ($\sim 10^5 A$) can only small magnetic field, resulting in no effect on the electron propagation.

The density effect on the electron propagation was also suggested in the visible-ray image radiated from the fast electrons detected at the rear side of the Al target with different target thickness as shown in Fig.4.7.

At the thin target, the electron current looks like collimated. On the other hand, the fast electrons blanched in filaments at the thick target such as $500\mu m$. The results can be explained the plasma heating with the high-density electron current. The heated temperature near the target surface could be larger than that at the target further incide due to the stoping power in the plasmas. Therefore, the positive magnetic field can not be

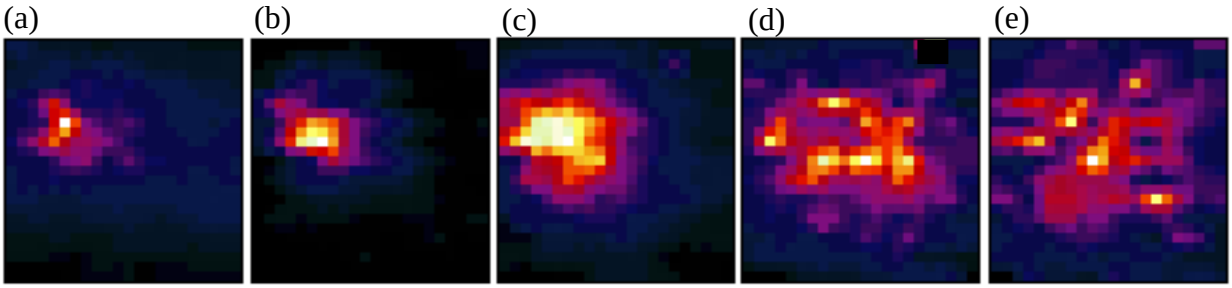

Figure 4.7: The visible-ray 2-dimentinal image radiated from the fast electrons detected at the rear side of the Al target with different target thickness. (a) $5\mu m$. (b) $50\mu m$. (c) $200\mu m$. (d) $500\mu m$. (e) $1000\mu m$.

enough created to balance the negative magnetic field at the target further incide, resulting in self-focusing of the electron current and blanched off in the filaments.

4.4 Summary

The study of the propagation of the high-density energetic electrons generated in ultra-intense laser-plasma interactions is investigated to measure the plasma heating by the electrons. The plasma temperature was up to 400eV from the neutron spectroscopy. The dependencies of the incident angle and plasma scale length on the plasma heating indicate that the plasma heating is strongly influenced by the Brunel absorption. The propagation of the high-density energetic electrons in the solid density plasma has a possibility of the collimating with the magnetic field by the density gradient and resistivity reduction in the plasma.

Reference

[1] G. Malka and J. L. Miquel, Phys. Rev. Lett. **77**, 75 (1996).

[2] K. B. Wharton, S. P. Hatchett, S. C. Wilks, M. H. Key, J. D. Moody, V. Yanovsky, A. A. Offenberger, B. A. Hammel, M. D. Perry, and C. Joshi, Phys. Rev. Lett. **81**, 822 (1998).

[3] F. N. Beg et al., Phys. Plasmas **4**, 447 (1997).

[4] S. C. Wilks, W. L. Kruer, M. Tabak, and A. Langdon, Phys. Rev. Lett. **69**, 1383 (1992).

[5] A. R. Bell, J. R. Davies, S. Guerin, and H. Ruhl, Plasma Phys. Control. Fusion **39**, 653 (1997).

[6] E. G. Gamaly, Phys. Fluids **5**, 3765 (1993).

[7] F. Brunel, Phys. Rev. Lett., **59**, 52 (1987).

[8] Y. Sentoku et al., Phys. Plasmas **6**, 2855 (1999).

[9] R. W. Lee and J. T. Larsen, J. Quant. Spectrosc. Radiat. Transfer. **56**, 535 (1996).

[10] M. Sonoda, M. Takano, J. Miyahara and H. Kato, Radiology **148**, 833 (1983).

[11] P. Gibbon and A. R. Bell, Phys. Rev. Lett. **68**, 1535 (1992).

[12] J. D. Jackson, *Classical Electrodynamics 2nd. Edition*, chapter 13 (John Wiley & Sons.Inc., New York 1975).

[13] M. Honda, J. Meyer-ter-Vehn and A. Pukhov, Phys. Plasma **7**, 1302 (2000).

[14] L. Spitzer and R. Härm, Phys. Rev. **89**, 977 (1963).

[15] H. M. Milchberg, R. R. Freeman, S. C. Davey, and R. M. More, Phys. Rev. Lett. **61**, 2364 (1988).

[16] J. R. Davies, A. R. Bell and M. Tatarakis, Phys. Rev. E **59**, 6032 (1999).

Chapter 5

Compressed Plasma Heating by High Energy Electrons

5.1 Introduction

High density plasma heating by high energy electrons created in ultra-intense laser-plasma interactions is interesting from a view point of inertial confinement fusion as well as high energy density phisics. Here the compressed plasma heating by the hot electron current is verified utilizing conically guided compression scheme. The attraction of the conically guided compression scheme is that it makes the rear surface of the compressed region more accessible to the short laser pulses both temporally and spatially. In fact, the compressed plasma in the guiding implosion within a conical hole in a dense high Z material is somewhat different from the plasma in the fast ignitor scheme in the point of the energy losses into the high Z material at high temperatures and the compression limitation of the plasma density in comparable to the cone material. It is, however, an attractive route to physics experiments to investigate some of the issues surrounding the fast ignitor with today's lasers.

In this chapter the hydrodynamics of the imploding material closely approximated to the 2D models and the heating of the imploded material with fast electrons from an ultra-short laser pulse is described.

5.2 Guided conical compression of plasma

The first question to address in guided compression is the effect of the high Z walls on the stability of the foil during the compression phase. Early investigations of guided compression in the late seventies at Los Alamos [1] and at the Lebedev in Moscow [2, 3] gave encouraging preliminary results, but these experiments have not been repeated since then. A more recent computational study has shown that the foil remains relatively stable during the compression stage, at least for a hollow, ablatively driven target [4].

To study this interesting stability problem, an experiment was conducted on the Nd: glass laser VULCAN [5] at the Rutherford Appleton Laboratory in U.K. The laser can be supplied sub-ns long pulse laser and sub-ps short pulse laser simultaneously. The output

of the broad-bandwidth (16nm) Tsunami Ti:sapphire oscillator was stretched to 300 psec with additional amplification before being split between the two rod amplifier arms, for long pulse and for short pulse. This eliminated all timing jitter between the different beam lines, and provided broad bandwidth for spectral smoothing in the long pulse drive beams. In the long pulse arm, a beam splitter was used to stack two pulses to provide a 600 psec full width at half maximum (FWHM) duration pulse. The ratio between the two pulses in the beam splitter was adjusted to provide a flat top output pulse; i.e. the effect of gain saturation was taken into account on the final pulse shape. This pulse was then amplified in the rod chain and then split between the six 108mm disk amplifiers. All long pulse beams were the frequency doubled to 527 nm. Two beams were stacked to provide a foot pulse of $16J/1nsec/5 \times 10^{13} Wcm^{-2}$ to target. The remaining four beams were displaced to provide a flat top main drive pulse to target of $2nsec/320J/5 \times 10^{14} Wcm^{-2}$. Shaped random phase plates, with f/10 lenses generated a focal spot diameter of $200\mu m$. The intensity distribution in the focal plane was doughnut shaped and was higher on the edges than in the centre by a factor of 1.2:1.0. The doughnut intensity profile was used in an attempt to shape the flat foil during the implosion (although it is recognized that a spherically shaped foil is the better solution for future experiments). In the short pulse arm of the VULCAN laser, the beam was amplified to the 60J level (45J to target) and compressed using large area diffraction gratings to 15 psec. The beam was focused onto target using a f/3 off-axis parabola.

Figure 5.1 shows the first experimental layout. The short pulse beam was focused onto an aluminum disk ($13\mu m$ thickness, $270\mu m$ diameter) which was coated with $0.5\mu m$ of bismuth. The beam was irradiated onto the Bi target at 30° from the target normal with a peak intensity of $5 \times 10^{15} Wcm^{-2}$. The Bi backlighting target was placed $700\mu m$ from the edge of a 2mm thick copper block which had a v-groove cut into the side. The depth of the groove was $250\mu m$ and the entrance size was $200\mu m$. On this Cu block was mounted a foil consisting of $12.5\mu m$ thick polyethylene with $2.0\mu m$ of chlorinated paralyene coated on the inner edge. The 2ω drive beams were focused $500\mu m$ on the foil from the edge of the Cu block. The $5\mu m$ diameter pinhole was position either at 7mm or 17 mm from the Bi target. The 16-bit Intaspec x-ray CCD detector (which was filtered by $125\mu m$ Be to all eliminate Cu L-shell emission) was positioned 21 cm from the Cu target, giving a magnification of $\times 30$ for Figures 5.2(a) and 5.2(b) and $\times 12$ for Figure 5.2(c).

Figure 5.2(a) shows an image recorded when only the 2ω nanosecond drive beams irradiated the target. The remaining unirradiated stationary foil, which is still in the line of sight, can be seen in this image. Also, some self-emission from the ablated plasma at the front and back of the foil can be observed. The important point to note is that no self-emission from either the Cu walls or from the stagnating plasma can be observed, resulting in remaining at low temperature. Figure 5.2(b) shows an image when the Bi backlighter foil was irradiated without drive beams. The stationary foil can be seen in the real size of the Bi-coated backlighter. Figure 5.2(c) shows an image of the guided plasma taken 1.0 nsec from the leading edge of the $2nsec, 5 \times 10^{14} Wcm^{-2}$ pulse. It can be seen that the inner edge of the foil has moved into the cone. The foil image shows some inner curvature according to the doughnut intensity profile of the drive beams at the edges of the v-groove without exhibition of the growth of any hydrodynamics instability at the foil surface.

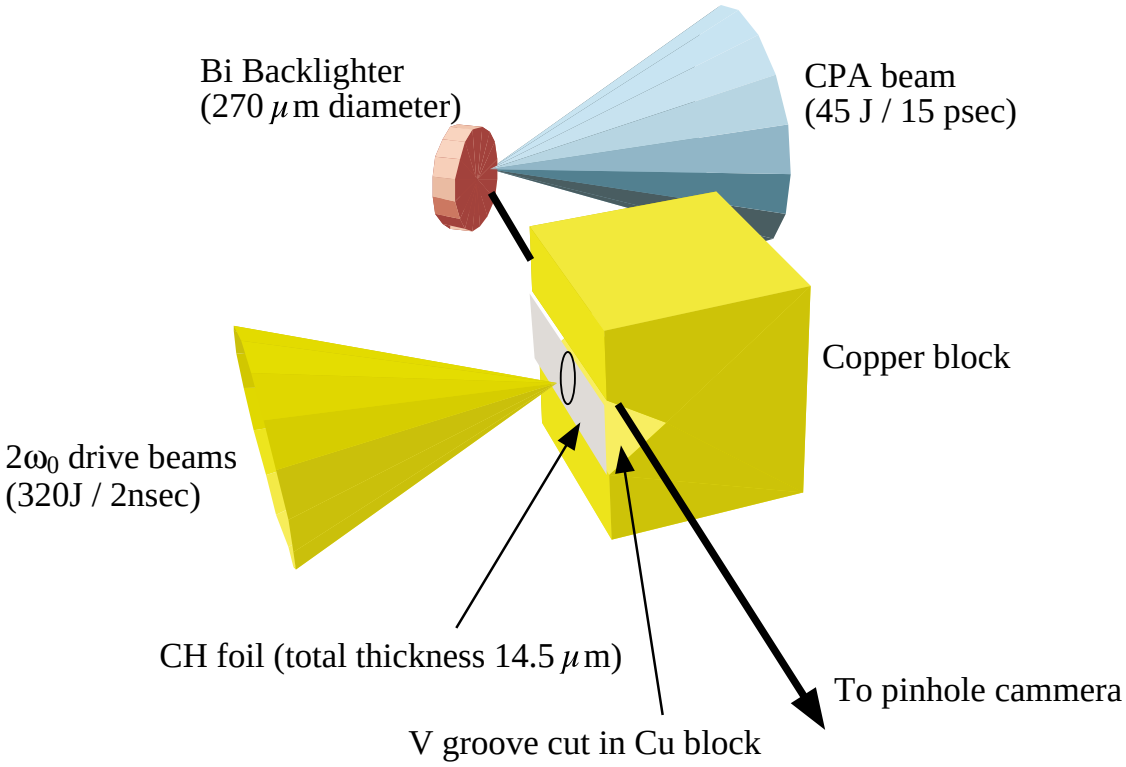

Figure 5.1: Schematic illustration of the back-lighting experiment.

The experiment was modeled using the Eulerian code POLLUX [8]. POLLUX is a two dimensional hydrodynamics code that uses a corrected Thomas-Fermi equation of state (although no radiation transport is included). Simulations with 240×133 cells were run on a PC class machine. The target and illumination geometry reproduced those used in the experiment, including the doughnut shaped intensity distribution in the focal plane. However, the drive intensity had to be adjusted to $1.0 \times 10^{13} W cm^{-2}$ and $1.0 \times 10^{14} W cm^{-2}$ on the foot and main drives pulses respectively, in order to match the observed implosion velocity. Figure 5.3(a) shows the development of the guided compression at 1 nsec from the main drive pulse. It is interesting that the majority of the foil is uniform, although there is significant roll up of the edges of the foil on the guiding walls, in good agreement with the observations (and that calculated by Charakhch'yan who attempted to explain the early Lebedev experiments [7]). Figure 5.3(b) shows the foil as the beginning of the first shock convergence taken at 1.57 nsec. The density achieved at this point is $4 g cm^{-3}$ and the temperature is ~100 eV. No further increase in the compressed density is obtained at stagnation with this implosion velocity.

5.3 Compressed plasma heating

A fully integrated conical compression experiment was conducted to test these predictions, and to determine the efficiency of fast electron heating. In this second experiment, the six

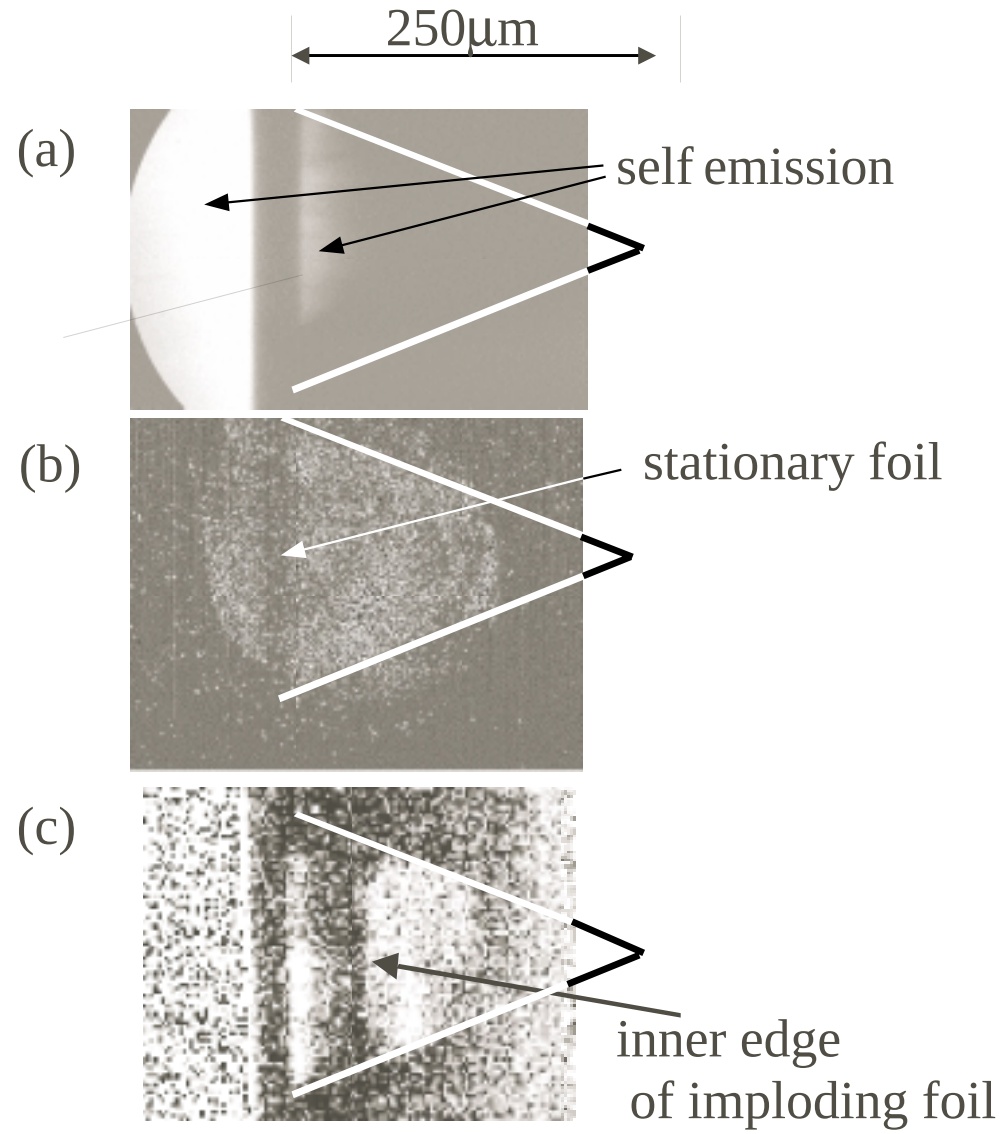

Figure 5.2: Images of the guided compression looking down the v-groove with (a) the drive beams only (b) the 15 psec beam (c) all beams taken at 1.0 nsec from the start of the main drive pulse.

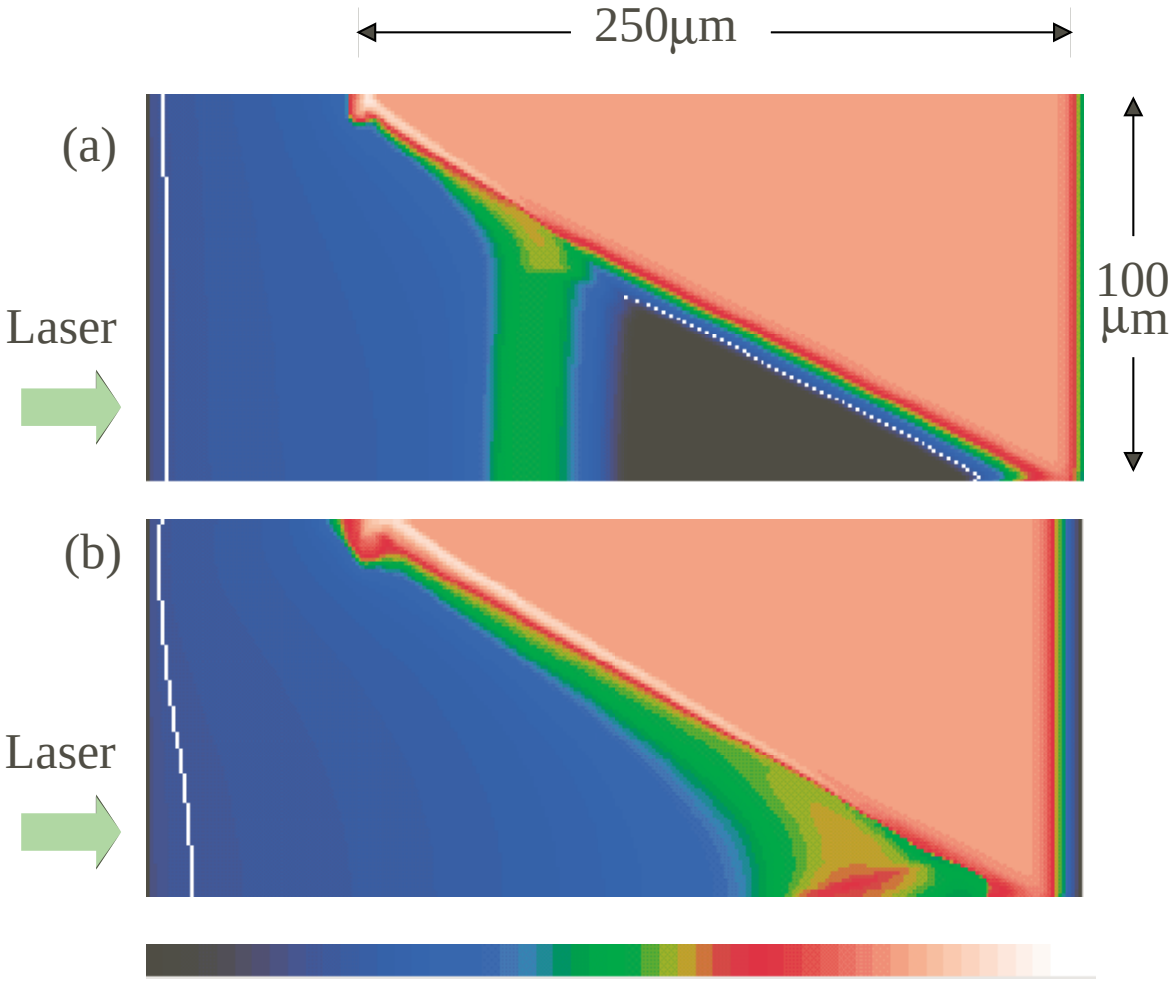

Figure 5.3: 2D simulations taken at (a) 1.0 nsec and (b) 1.33 nsec from the start of the main interaction pulse. The roll up of the foil plasma can be clearly seen in (a).

2ω long pulse beams irradiated a $12.5\mu m$ flat polyethylene CH foil, which was covered with a $2.0\mu m$ of deuterated polystyrene CD foil. A $100\mu m$ diameter, 100nm thick signature layer of Ti and a 500nm thick layer of chlorinated paralyene were deposited between the CH and CD foils, with the CD layer facing the apex of the Au cone. The distance from the entrance hole to the apex was $250\mu m$ and the Au cone material was $20\mu m$ thick. A $20\mu m$ hole was machined in apex of the cone, so that the target could be precisely positioned and the fast electrons transport was through the compressed CH/CD material only. A $12.5\mu m$ thick, $270\mu m$ diameter polyethylene foil was placed over the apex of the cone, in order to control the scale-length of the short pulse interaction process. The p-polarized 45J / 15 psec pulse was focused onto this foil in a 20mm spot, giving a peak intensity on target of $10^{18} W cm^{-2}$ and electrons with a temperature of between 200-300 keV [9]. The cone assembly and the foil covering the apex of a sample target are illustrated in Figure 5.4.

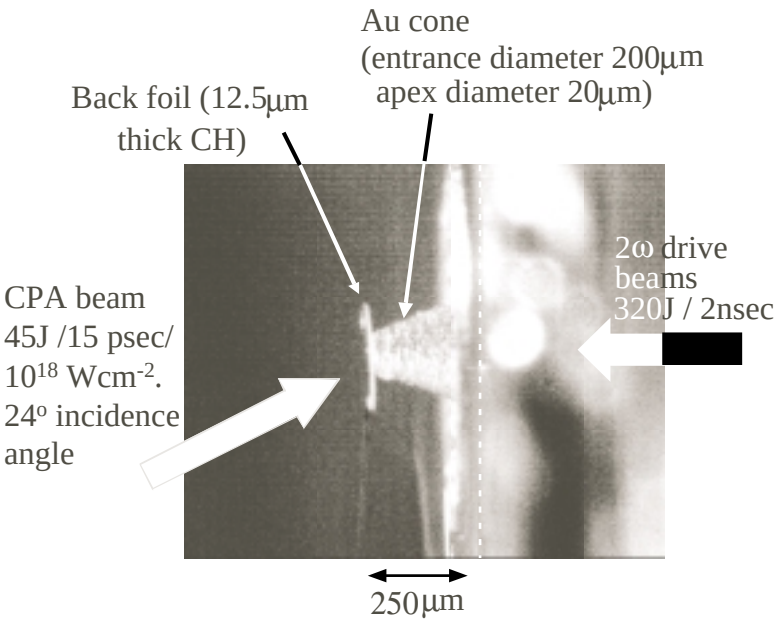

Figure 5.4: Image of the assembled target for the conical compression experiment.

The diagnostics for this experiment consisted of both time integrated and time resolved crystal spectrometers, a highly sensitive Ag activation counter and a number of current mode time-of-flight neutron detectors. The spatially integrated x-ray emission from the signature layers in the compressed/heated targets was observed using flat crystal spectrometers with a Si 111 crystal for the Cl Lα ($\lambda = 4.185$ Angstroms) and a Si 220 crystal for Ti Heβ ($\lambda = 2.221$ Angstroms) lines. A flat KAP crystal was coupled to a Kentech x-ray streak camera to observe the spatially integrated, but spectrally and temporally resolved x-ray emission.

A highly sensitive Ag activation counter was constructed to measure the $d(d,n)^3He$

neutrons from the heated CD layer. The counter consisted of a polished $5 \times 5 \times 5cm^3$ perspex which was surrounded on all sides by a 5mm thick NE102 plastic scintillator, of which the outside was covered by Ag foil. The 2.45 MeV neutrons were moderated in the perspex and the thermal neutrons which were generated as a result then interacted with the Ag via the reactions ${}^{107}_{47}Ag(n,\gamma)^{108}_{47}Ag$ and ${}^{109}_{47}Ag(n,\gamma)^{110}_{47}Ag$. The ${}^{108}_{47}Ag$ and ${}^{110}_{47}Ag$ then β^- decay to ${}^{108}_{48}Cd$ and ${}^{110}_{48}Cd$ with a half-lives of 24.6 seconds and 144 seconds respectively. The β^- decay produces photons in the plastic scintillator, and the perspex block acts as a wave-guide for these photons to the photo-multiplier whose electrical signal was then fed into an amplifier/counting unit. The instrument was located such that the perspex block was 10.7 cm from the target, resulting in a collection angle that was close to 1 steradian. The instrument was calibrated off-line using a moderated ${}^{241}Am/Be$ fission source.

The time resolved x-ray spectra showed that there was a significant increase in x-ray emission that peaked at 1.7 nsec after the beginning of the main pulse, suggesting that this increase in x-ray emission corresponded to the onset of stagnation. However, the x-ray signal was appeared when only the main drive beams were fired. The time integrated spectra for this shot did reveal that some M-band Au emission was present, as well as some Cl Lα emission, suggesting that kinetic energy of the stagnating foil was converted to thermal energy, as expected. The high intensity heating pulse was then employed and moved to coincide with the stagnation time. However, the Si 220 crystal spectrometer showed no evidence of time integrated spectra Ti Heβ emission when the short pulse beam was fired at 1.7 nsec after. Calculations with the atomic physics package FLY[10] confirmed that pressure ionization of the n=3 level only becomes significant with densities above $\sim 30gcm^{-3}$, and that Heβ emission from the Ti layer should have been observed with an electron temperature of 1.0 keV. Thus, the absence of Ti Heβ line emission in the experiment sets an upper bound to the heated electron temperature of 1keV.

Neutrons were observed when the shot of the short pulse beam was fired at 1.7 nsec after the beginning of the main pulse. Crosses in Fig. 5.5 show the β^- decay counts taken in the Ag activation counter. Also plotted are with three other separate shots which were taken when the heating beam was moved $\pm$100 psec from this point in time, equivalent to background level as shown by dotted line in Fig. 5.5. These shots show that if any neutrons were generated at these other times, they were below the threshold of the detector. They tend to rule out (γ, n) and (p,n) neutron generation processes in the target or the surrounding equipment. It is because the energetic protons or γ-ray generation due to the electron bremsstrahlung is decided only the intensity of the short pulse laser at the CH foil. When the background signal is subtracted from the decay signal, the observed β^- decay curve is consistent with a 25 second half life, and a yield of 2×10^4 neutrons (the signal to noise is too small to unambiguously count the ${}^{109}_{47}Ag(n,\gamma)^{110}_{47}Ag$reaction). The data strongly suggest that the neutrons are generated as a result of the thermonuclear reaction $d(d,n)^3He$ from the heated CD layer.

I can make an estimate of the plasma temperature needed to generate this neutron yield. Assume the fast electrons uniformly heat the plasma. The energy obtained from an inertially confined DT plasma is equal to the burn-up fraction multiplied by the total energy available from the fuel. The burn up fraction is given by the expression

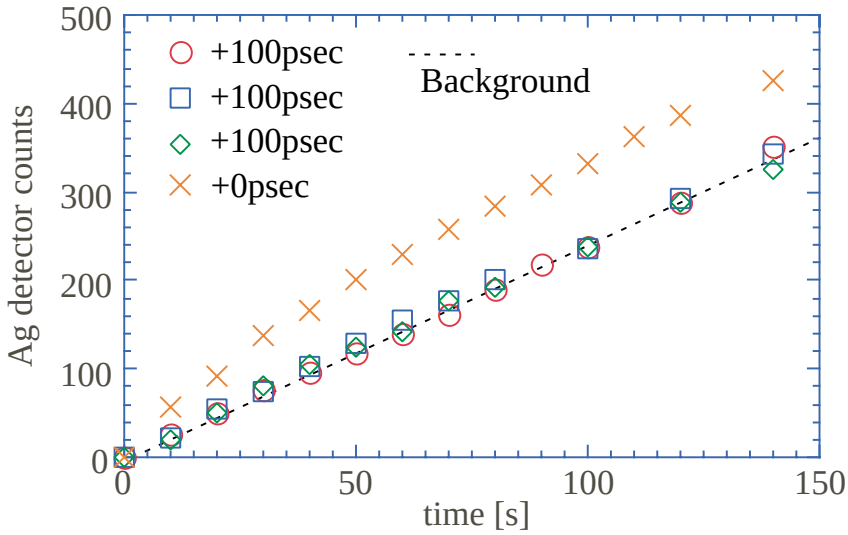

Figure 5.5: Measured counts in the Ag activation counter for four shots taken within 100 psec of the stagnation point at 1.7 nsec showing.

$$f_b = 5.6 \times 10^3 (\rho R) exp\left(\frac{-19.9}{kT_{keV}^{1/3}}\right) / kT_{keV}^{1/3}, \tag{5.1}$$

When CD material is substituted for DT and ρR of $\sim 10 mgcm^{-2}$ is used, then the plasma temperature of the CD layer needed to generate 2×10^4 neutrons is $\sim 500eV$. This means that $\sim 7\%$ of the short pulse laser energy was coupled to the plasma to produce this temperature. While this coupling efficiency appears somewhat low, it may be increased by a more suitable match of the range of the fast electrons (which depends upon $I\lambda^2$) to the achieved ρR.

5.4 Summary

I have shown here the guided compression to explore some of the physics issues of hot electron heating and transport in the compressed plasma, while avoiding the difficulties associated the stability of the channel formation pulse. I have demonstrated, using an open geometry and x-ray backlighting, that the guided foil remains stable during the compression, and that good agreement is obtained with two-dimensional hydrodynamics simulations. An integrated conical compression experiment has confirmed, resulting in the heated temperature of about 500eV in the compressed plasma.

Reference

[1] M. Key et al., Phys. Plasmas, **5**, 1966 (1998)

[2] R. J. Meson, R. J. Fries, and E. H. Farnum, Appl. Phys. Lett, **34**, 14 (1996).

[3] S. I. Anisimov et al., Sov. Tech. Phys. Lett., **4**, 175 (1978).

[4] S. I. Anisimov et al., JETP Lett., **29**, 134 (1980).

[5] J. M. Martinez-Val and M. Piera, Fusion Technology, **29**, 134 (1996).

[6] C. N. Danson et al., J. Modern Optics, **45**, 1653 (1998).

[7] A. A. Charakhch'yan, J. App. Mech. & Tech. Phys., **4**, 506 (1994).

[8] G. J. Pert, J. Comp. Phys., **43**, 111 (1994).

[9] S. C. Wilks, W. L. Kruer, M. Tabak, and A. B. Langdon, Phys. Rev. Lett., **69**, 1383 (1992).

[10] R. W. Lee and J. T. Larsen, J. Quant. Spectrosc. Radiat. Transfer., **56**, 535 (1996).

Chapter 6

Neutron Spectroscopy for Ion Acceleration Mechanism

6.1 Introduction

Recent progresses in an ultra intense laser technology, generation of energetic ions [1, 2, 3] in MeV ranges have been reported in the laser plasma interactions. These energetic particles are extremely important in the Fast Ignitor concept [4] in Inertial Confinement Fusion(ICF) research to study of additional heating of fuel core plasmas. There energetic particles are also interesting as high energy particle sources in other fields such as nuclear physics and laboratory-astrophysics. In this chapter, I show the study of ion acceleration mechanism in ultra-intense laser-plasma interactions from polarization, laser intensity and prepulse level dependences of neutron spectra from nuclear fusion reactions in targets.

6.2 Ion acceleration mechanism

As mentioned in chapter 1, the ion acceleration mechanism in ultra-intense laser-plasma interactions has not been elaborated yet because of its complicated process. The ions are accelerated following the electron acceleration since the ion is too heavy to be directly accelerated by the laser field at intensities of less than $10^{20}W/cm^2$ for 1μm light. As one of the possibilities of the ion acceleration mechanism, fast electrons generated in ultra-intense laser-plasma interactions might drag ions via a coulomb potential between the fast electrons and ions [5]. The acceleration direction of the fast electrons depends on the laser absorption mechanism influenced by the laser polarization [6], i.e. the laser direction via $J \times B$ heating [5] for s-polarization and the rear normal of the target surface via Brunel absorption [7, 8] for p-polarization. Then ions might be accelerated in the different direction following the fast electrons at the different polarization. Another candidate of the ion acceleration mechanism is an electrostatic field created along the target surface by a charge displacement due to an exclusion of the fast electrons at the laser front. Therefore, the static field accelerates the ions in the direction of the rear normal of the target surface at any polarization. Coulomb explosion in gases, clusters and plasmas could be also one of the possible mechanisms of ion acceleration in the isotropic direction [9]. Therefore,

precise measurements of the ion motion with different laser polarization are essential for the investigation of the ion acceleration mechanism.

I obtained the laser polarization dependence of momentum distribution of accelerated ions in ultra-intense laser interactions with a solid target. The ion acceleration inside the target was investigated by measurements of neutron spectra from nuclear fusion reactions of accelerated deuterons with the target deuterons (beam fusion). The first observation of neutron from beam fusion reaction in ultra-intense laser-plasma interactions has been made by P.A.Norreys et al. [10]. Angular distribution of neutron yield has been also reported [3] before. However, momentum distribution of the accelerated ions inside the target has not been obtained yet, which requires precise observation of the angular distribution of neutron energy spectra. Then I have observed neutron spectra from different view angles to evaluate a momentum distribution of the accelerated ions. The experimental results have been also compared with a 2-D particle in cell (PIC) simulation to investigate the ion acceleration.

6.3 3D monte-carlo simulation

The momentum distributions of the accelerated ions are evaluated with the neutron spectra using a Monte-Carlo calculation. The calculated spectra were fitted to all the obtained neutron spectra from different angles to evaluate the distributions of the accelerated ions in the three-dimensional momentum space. To obtain the ion momentum distributions using the simulation, the neutron spectra were detected from different view points. The peak shift of the every neutron spectra and the intensity ratio among the spectra give an imformation of the ion acceleration direction and the ion energy. The spectral width in all neutron spectra show the ion distribution shape.

In the calculation, the target is assumed to be a solid density ($\sim 1.1 g/cm^{-3}$) deuterated plastic (polyethylene) plane ($100\times100\times5\mu$m) with an initial temperature of 0.1eV (not ionization) and test particle numbers of 8214. The stopping power to the accelerated ions is given by Jackson's equation [11] taking accounts of density effects in the relativistic region on scattering and energy losses, giving

$$\frac{\delta E}{\delta z} = \frac{\omega_p^2 (z_{eff})^2 e^2}{c^2 \beta^2} G(y_e) ln\Delta, \tag{6.1}$$

where E is the ion energy, ω_p the plasma frequency, Z_{eff} the effective charge number, $G(y_e)$ the error function, y_e the accelerated ion energy divided by background electron or ion temperatures and $ln\Delta$ the coulomb logarithm.

On the other hand, the accelerated ions impacts to the ions in the solid target and generate neutrons through nuclear fusion reaction. I used deuteron-deuteron reaction ($D[D,n]^3He$) as the neutron generated reaction of which cross sections for the neutron reaction of deuterons are referred from established data [12]. The neutron yield is represented by

$$Y_n = n_{ai} n_{ti} < \sigma v > dt, \tag{6.2}$$

where the n_{ai} is accelerated ion number density, n_{ti} the target ion number density, σ the cross section of nuclear reaction, v the relative velocity between accelerated and target ions and dt the reaction time.

The direction of neutrons to the angle of the incident deuteron in the Lab. system can be relatively written by

$$\begin{aligned} E_n &= \frac{-(d) \pm \sqrt{(d)^2 + 4(c)(a)}}{2(c)}, && (6.3)\\ where(a) &= 2m_D c^2 E_D - 2m_{^3He} c^2 (Q + E_D) - Q^2 - 2QE_D, && (6.4)\\ (b) &= 2(m_n c^2 + m_{^3He} c^2 + Q + E_D), && (6.5)\\ (c) &= 4cos^2\theta \cdot (2m_D c^2 E_D + E_D^2) - (b)^2, && (6.6)\\ and(d) &= 8cos^2\theta \cdot m_n c^2 (2m_D c^2 E_D + E_D^2)^2 - 2(a)(b). && (6.7) \end{aligned}$$

m_D, $m_{^3He}$ and m_n are the rest mass of deuteron, ^3He and neutron, respectively. Q is the released energy through the nuclear reaction, θ the incident angle and E_D the incident energy of the accelerated deuteron.

In the three-dimensional space, we change shapes of an ion momentum distributions in respective coordinates, i.e. Px, Py and Pz, where Px corresponding to the target rear side normal, Py the y-axis parallel to the electrical field of the laser lights and Pz the z axis perpendicular to the electrical field. As examples, we show five different distributions as shown in Fig.6.1; (a) Isotropic momentum distribution of accelerated ions. (a)-i is a momentum distribution with a Maxwellian energy distribution. The arrow in the target shows the direction of laser incidence. The gray area represents the target inside and the white is the vacuum region. (a)-ii and (a)-iii shows the calculated spectra at 180 degree and 90 degree from the target normal direction. (b) Isotropic momentum distribution of accelerated ion with a monochromatic energy. Other figures conditions are shown as a same as (a). (c) Momentum distribution collimated the target normal direction and the calculated spectra with Maxwellian energy distribution. (d) Momentum distribution and calculated spectra collimated 45 deg. from the target normal with a Maxwellian energy distribution. (e) Complicated momentum distribution shape and its calculated spectra with a Maxwellian energy distribution. Even if there is a similar shape spectrum, neutron spectra with multi channel detection can identify the ion momentum distribution.

To compare the experimental and calculated neutron spectra from different angles, a calculation condition is fixed: the target is a solid density ($\sim 1.1 g/cm^{-3}$) deuterated plastic plane (100x100x5μm) with an initial temperature of 0.1eV (not ionization) and test particle numbers of 8214.

6.4 Experiment

The experiments were performed by using 50-100TW short pulse glass laser systems at Institute of Laser Engineering (ILE), Osaka University. The 1.05μm light laser energies were 20-50J on target and the pulse widths were 450-800fs from a second-order autocorrelator. The pulse shape was identified with correlation between the autocorrelator signals

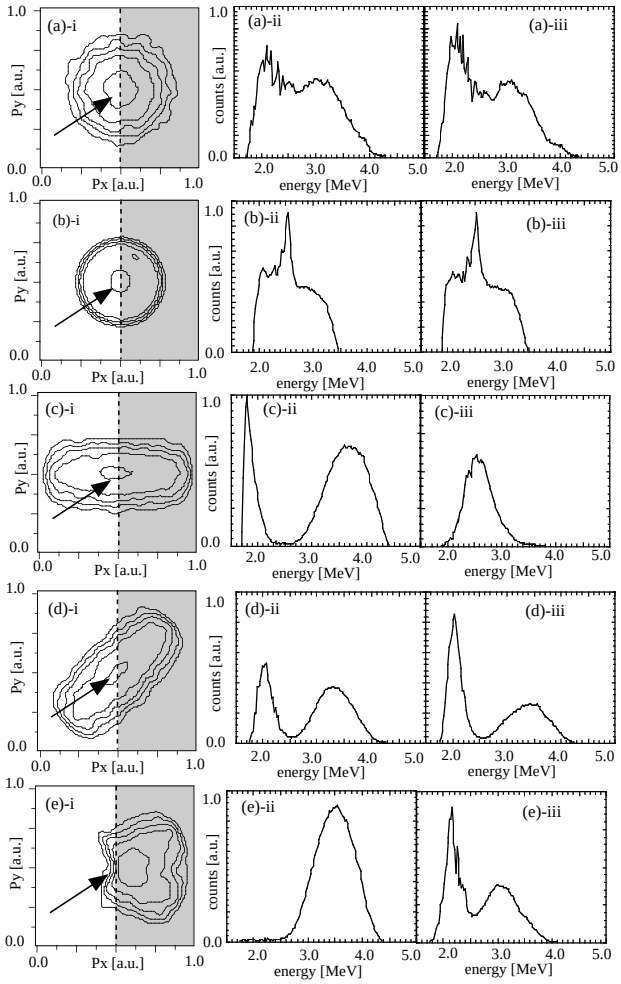

Figure 6.1: Examples of (i) ion momentum distributions and (ii), (iii) calculated spectra from 180 deg. and 90 deg. to the target normal. The arrow shows the direction of the laser incidence. The gray area represents the target inside and the white is a vacuum region. (a) Isotropic distribution with a Maxwellian energy distribution. (b) Isotropic distribution with a monochromatic energy ion. (c) Momentum distribution collimated to the target normal direction with a Maxwellian energy distribution. (d) Momentum distribution collimated to the 45 degree to the target normal with a Maxwellian energy distribution. (e) Complicated momentum distribution.

and spectra from a spectrometer as well as the result from a third-order autocorrelator. The prepulse level was monitored with a pin diode to be less than 10^{-4} to the main pulse intensity appended at 700 ps before the main pulse. Two different linear polarization conditions, i.e. *s*-polarization and *p*-polarization, were taken to measure the polarization dependence of the neutron spectra from $d[d,n]^3He$ fusion reaction. A 5μm thickness deuterated plastic (CD) target was obliquely irradiated by the short pulse laser light through f/3.8 off-axis parabolic focusing mirror. The peak intensity of the main pulse on the target was $10^{19}W/cm^2$ from the spot of 20μm in a diameter.

Neutron spectra were detected with neutron spectrometers consisted of plastic scintillators from different view angles through a time of flight (TOF) method. Two different types of spectrometers were used in the experiment: one type was a single channel detector to obtain the spectra from a temporal current profile of the scintillator signals and another a multi-channel detector system to obtain the spectra from the channel event number [13]. Reliable detection ranges of neutron energies of the system were under 20MeV. Energy resolutions of the neutron spectra were about 29keV(multi-channel detector) and 110keV(single channel detector). Three detectors (one is the current type and two are the counting type) were set up at different view angles. All the neutron detectors had 5cm-thick cylindrical polyethylene collimators with 5mm-thick lead blocks in the chamber to reduce a gamma-ray noise from scattered electrons at the chamber inside, e.g. at the chamber wall and the other diagnostics such as pinhole cameras. In order to reduce the signal level of a gamma-ray noise from the target, 15cm lead blocks were placed at the front of the scintillators. 5cm thick lead blocks were also set at the side of the detector to protect it from the gamma rays. Neutron scatter effects on the spectra at the lead block were calibrated with thermal neutron signals created in imploded glass micro balloon (GMB) with a DD-fuel, resulting in the negligible effect of scattering neutrons on the spectra.

6.5 Laser Polarization dependence

I obtained the laser polarization dependence of ion acceleration in ultra-intense laser interactions with solid targets. The ion acceleration was investigated by measurements of neutron spectra from nuclear fusion reactions of accelerated deuterons with the target deuterons (beam fusion). The ion momentum spatial distribution is estimated from the spectra comparing 3-D Monte-carlo simulation. The polarization dependence of the ion acceleration from the experiment is also compared with simulation results from 2-dimensional Particle in cell (PIC) code.

Solid lines in Figs.6.2(a) and 1(b) show the observed neutron spectra at a laser incident angle of 40° to the target normal for the *s*-polarization condition at observation angles of (a)56° and (b)39° to the target normal, corresponding to the back side of the laser direction. The spectra from 56° and target normal are shown in Fig.6.3(a) and 6.3(b) for the *p*-polarization condition with 36° incidence to the target normal. The signal level on the figures is normalized to be a neutron yield per solid angles taking account of the detector position and sensitivity. All the peak of the spectra for the target front side shift to the lower energy from 2.45 MeV given by the D-D thermal fusion reaction. These spectral shifts imply that ions are accelerated into target inside for either polarization

taking account of the momentum conservation, which is similar to a Doppler effect on the neutron spectra. Detailed analysis of the ion motion from the spectra is performed by using the 3-D Monte-Carlo code to fit the calculation to the experimental spectra. The dot-dashed lines in Figs.6.2(a), 6.2(b), 6.3(a) and 6.3(b) show the spectra well fitted to the experimental results giving the ion momentum distribution collimated to the rear normal of the target surface. As a comparison, the spectra corresponding to the ion acceleration to the laser direction are also shown as dotted lines in Fig.6.2 and 6.3. No possibility of the ion acceleration in the laser direction is clearly seen from the spectra fitting for both polarization conditions. The well-fitted 3-dimensional momentum distributions are given by an anisotropic 3-D Maxwellian distribution. The distribution projected on the x-y plane is shown as a contour plot in Fig.6.2(c) (s-polarization) and Fig.6.3(c) (p-polarization), where Px corresponds to the rear normal of the target surface, the Py axis parallel to the target surface and Pz the direction perpendicularity to the figure. Each line represents every $10^{0.2}$ of the ion number in a logarithmic scale. The ion energy in the x-direction corresponding to the rear normal of the target surface is about 330keV for the s-polarization and 370keV for the p-polarization whereas the energy to the y- and z-directions are about 30keV for the s-polarization and 40keV for the p-polarization. In the results, the ions are accelerated toward the rear normal of the target surface in the either linear polarization. We also changed the laser incident angles ($10^\circ \sim 45^\circ$) at different polarization. At all the incident angles and polarization, we concluded the ion acceleration to the rear normal of the target surface from the neutron spectra.

Momentum distributions of accelerated ions inside the target at different polarization (s- and p-polarization) are also investigated with a two-dimensional particle-in-cell (PIC) code in ultra-intense laser-plasma interactions. In the simulation code, the deuteron plasmas are fully ionized and its geometry has an oblique surface to the laser axis set in the middle of a simulation box (23μm square). The density profile from $4n_c$ as a maximum density to $0.1n_c$ has a steep exponential shape with a scale length of 0.1μm. The 1.05μm laser light with a 200fs pulse duration irradiates the plasma at an incidence angle of 30° and a peak intensity of $10^{19}W/cm^2$ during the simulation time within a 7μm spot diameter. Figure 6.4 shows the contours of the ion momentum for (a) s-polarization and (b) p-polarization from the PIC simulations at the end of pulse duration. Each contour line corresponds to every $10^{0.5}$ of the ion number in a logarithmic scale. At either polarization, the ion accelerations shown in the PIC simulation are collimated toward the rear normal of the target surface, which agree with the experimental results.

All the experiment and simulation results show the ion acceleration in the directions of rear normal of the target surface at either polarization. These results indicate that the ions are not accelerated by a direct coulomb potential between the accelerated electrons and remained ions but by the electrostatic field. At the laser front, a charge displacement is generated along the target surface due to an exclusion of the fast electrons. The charge displacement creates an electrostatic field along the target surface to the rear normal of the surface. Then this static field accelerates ions in the direction of the rear normal of the target surface at any polarization.

On the other hand, the energy of accelerated ions could be different from each other at different laser polarization condition. Table 6.1 shows the ion momentum distributions and energies to the rear normal of the target surface from the experiment and the PIC

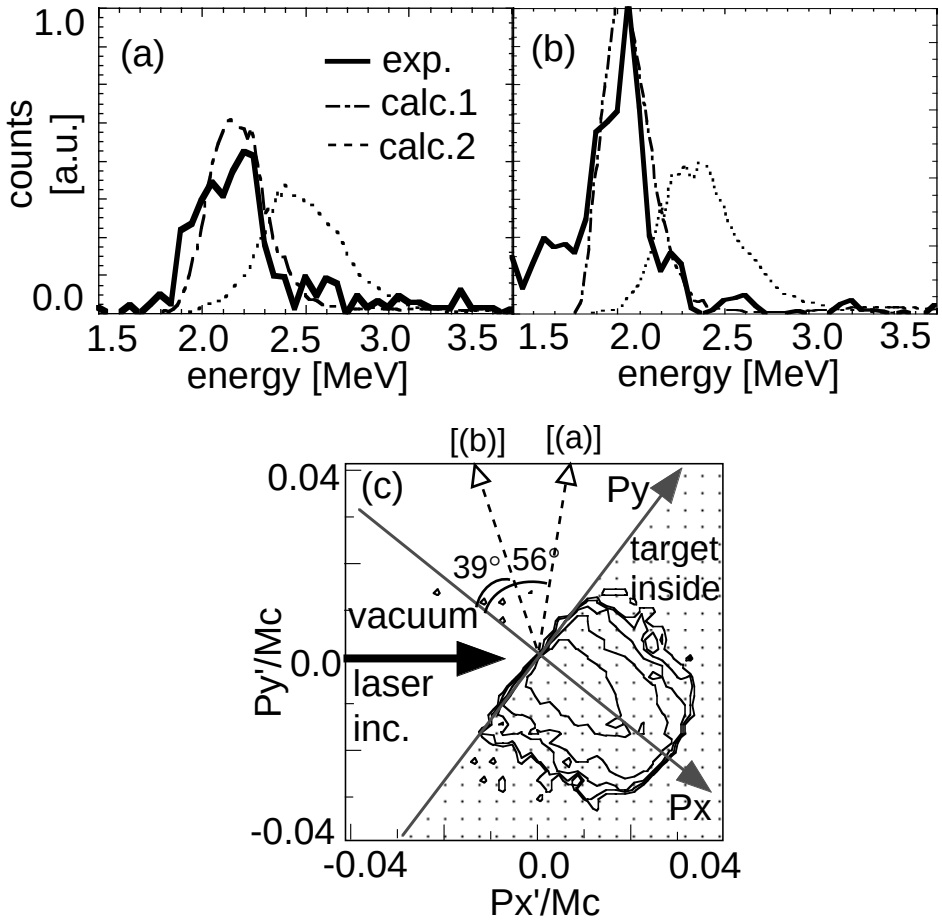

Figure 6.2: The neutron spectra for the *s*-polarization detected at (a)56° and (b)39° to the target normal. The experimental spectra are shown by solid lines. The dot-dashed lines and dotted lines represent the calculated spectra from the 3D Monte-Carlo code assuming the ion acceleration in the direction of rear normal of the target surface and laser direction, respectively. (c) Contour plot of two-dimensional distribution of the ion momentum obtained by spectral fitting as shown in Figs.1(a) and (b). The momentum is normalized by Mc (M:ion rest mass, c: light speed). Each contour line represents every $10^{0.2}$ of the ion number in a logarithmic scale.

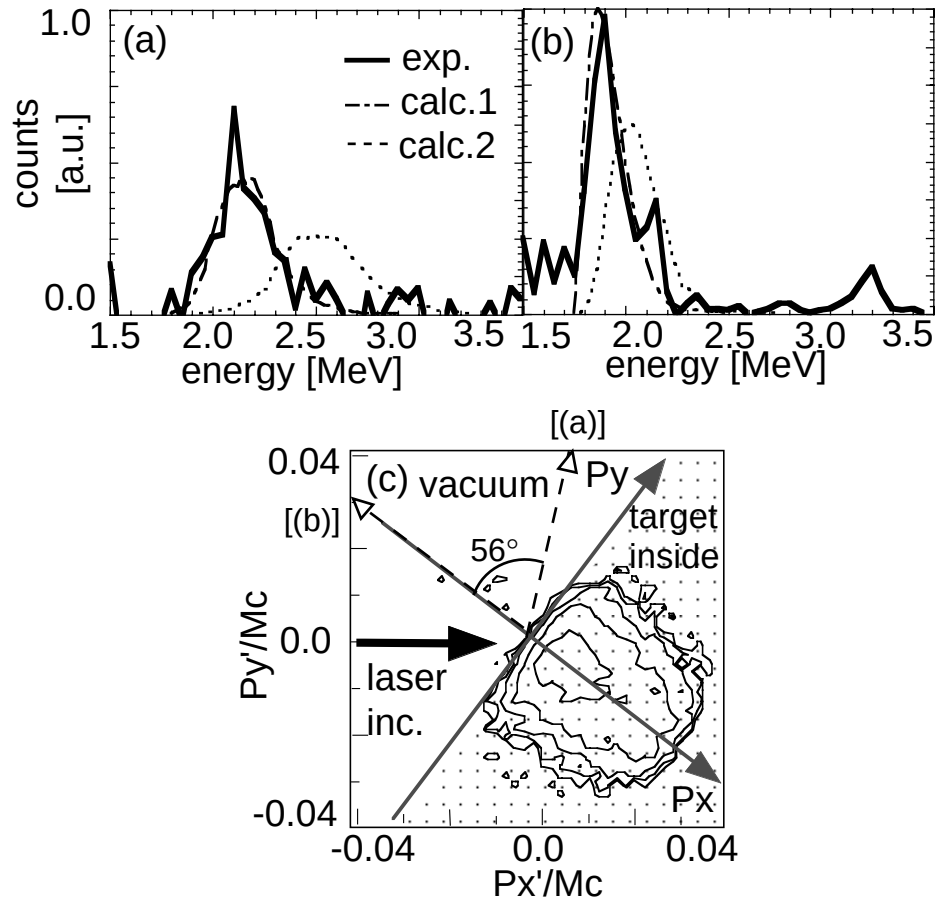

Figure 6.3: The neutron spectra for the p-polarization detected at (a)56° to the target normal and at (b)the target normal. The solid lines are experimental results. The dot-dashed lines and dotted lines show the calculated spectra corresponding to the ion acceleration to the rear normal of the target surface and to laser direction, respectively. (c) Contour plot of 2-D spatial distribution of the ion momentum for the p-polarization. The other figure conditions are as same as Fig.6.2(c).

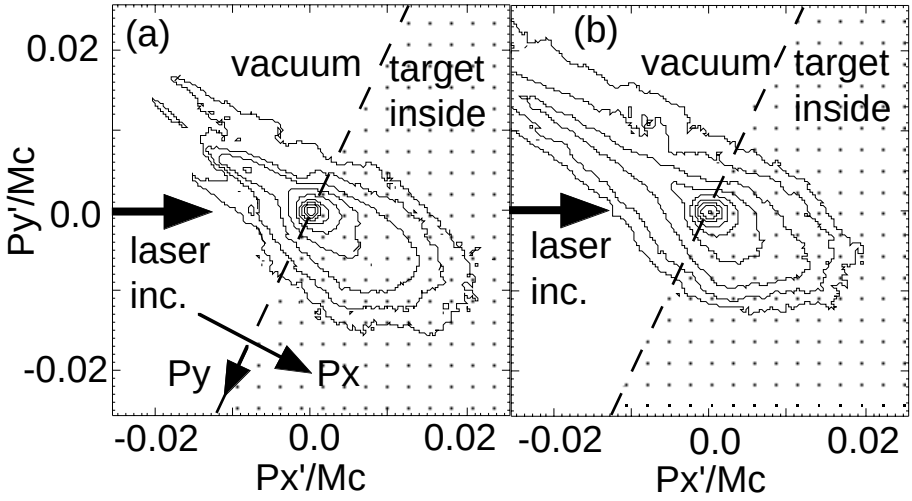

Figure 6.4: The ion momentum distributions of (a) *s*-polarization and (b) *p*-polarization from 2D PIC simulation. The momentum coordinate is normalized by Mc. Each contour line corresponds to every $10^{0.5}$ of the ion number in a logarithmic scale.

simulation at different laser polarization. At either laser polarization, the directions of the ion acceleration were rear normal of the target surface in both of the experiment and the simulation. However, the energies of ions were clearly different from each other at different polarization.

The difference of the accelerated ion energy could be due to plasma heating created by different laser absorption. Figure 6.5 shows the energy distribution of accelerated ions on the x-coordinate for (a) *s*-polarization and (b) *p*-polarization from the PIC simulation at the end of pulse duration.

The laser and plasma parameters in the calculation are the same as those in Fig.6.4. In the figures, the plus direction on the transverse axis corresponds to the target inside (rear normal of the target surface) and the minus to the vacuum side. The temperature

	Polarization	Momentum ratio (Px:Py:Pz)	Ex [keV]
Exp.	*s*-pol.	2.2:1:1	330
	p-pol.	1.4:1:1	120
Sim.	*s*-pol.	2.8:1:1	400
	p-pol.	1.4:1:1	120

Table 6.1: Summary of momentum distributions and temperature of ions from experiment results (incident angle : 45°) and 2D PIC simulations (30°) at different polarization. Px is momentum corresponding to the rear normal of the target surface, Py for y-axis parallel to the target surface and Pz the direction perpendicularity to the figure. Ex shows the temperature of accelerated ions to the x-direction (the target inside).

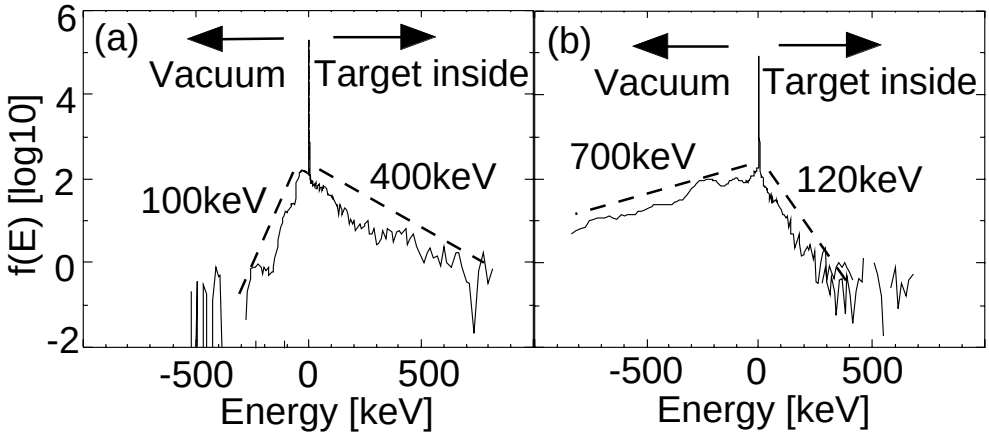

Figure 6.5: The ion energy distributions accelerated to rear normal of the target surface for (a) s-polarization and (b) p-polarization from the PIC simulation. The direction of the plus on the transverse axis corresponds to the target inside (rear normal of the target surface) and the minus to vacuum (target normal). The dotted lines show a near-Maxwellian distribution with a temperature of 400keV for ions into the target and 100keV to vacuum at s-polarization. At p-polarization, the temperature for the ions into the target is 120keV and 700keV to vacuum.

of ions accelerated inside the target is about 400keV at the s-polarization and 120keV at the p-polarization. On the other hand, the temperature of ions to the vacuum side at the p-polarization (700keV) is larger than that at s-polarization (100keV), indicating a strong plasma expansion to the vacuum side due to larger laser absorption at the p-polarization. From the PIC simulation, the absorption efficiency of p-polarized laser light at obliquely irradiation is about three times larger than that of s-polarized light, i.e. 26% for p-polarization and 8% for s-polarization [14]. The significant absorption at p-polarization creates higher-temperature plasmas with strong gradient pressures. The stronger gradient pressure could decrease more the ion acceleration inside the target. From the momentum conservation at the laser front, an equation of the accelerated ion motion is given by

$$\begin{aligned} m_i \frac{\partial v_i}{\partial t} &= F_{pond}\cos\theta - F_{grad} \\ &\sim (2-A)\frac{I}{c}\cos\theta\frac{1}{l_s n_i} - \frac{n_e k T_e}{L n_i}, \end{aligned} \tag{6.8}$$

where m_i is the ion mass, F_{pond} the ponderomotive force, F_{grad} the gradient force, I the laser intensity, A the absorption, l_s the skin-depth, n_i the ion density, θ the incident angle, n_e the electron density, T_e the electron temperature and L the density scale. At the intensity of $10^{19} W/cm^2$, the $F_{pond}\cos\theta$ is about $9.8\times10^{-3}[dyn]$ (s-polarization) and $8.9\times10^{-3}[dyn]$ (p-polarization) at $\theta = 45^\circ$ and $l_s = 0.1\mu m$ [5]. On the other hand, the F_{grad} at the relativistic critical density is $2.0\times10^{-3}[dyn]$ (s-polarization) and $2.8\times10^{-3}[dyn]$ (p-polarization) using the electron temperature of 1.2MeV (s-polarization) and 2.3MeV (p-polarization)

from the PIC simulation [15], respectively. Therefore, the ion energy from eq. 6.8 could be 3.6MeV for the s-polarization and 2.2MeV for the p-polarization for $n_i \sim n_e$. This simple estimation indicates that the ion energy for the s-polarization become larger than that for the p-polarization, which is consistent with the experiment and simulation results.

6.6 Laser Intensity dependence

I obtained the laser intensity dependence of the ion acceleration. The laser condition was fixed at p-polarization 20 deg. incidence with less prepulse level ($\leq 10^{-4}$). Figs. 6.6(a) and (b) show neutron spectra from 43° (solid line) and 87° (dashed line) to target normal at $2 \times 1018 W/cm^2$ and $1 \times 10^{19} W/cm^2$, respectively. The signal level on the figure is normalized to be a neutron counts per solid angles taking account of the detector sensitivity. The peaks of neutron spectra at $2 \times 1018 W/cm^2$ are not sifted from 2.45MeV so much. On the other hand, neutron spectra at an intensity of $1 \times 10^{19} W/cm^2$ show clearly the shift of the peak from 2.45MeV The peak of the spectra for the target front side shifts to the higher energy side (2.9MeV at 43°, 3.0MeV at 87°) from 2.45 MeV given by the D-D thermal fusion reaction. The neutron counts at $1 \times 10^{19} W/cm^2$ is about a hundred times than the counts at $2 \times 10^{18} W/cm^2$. These differences of peak shifts and the neutron counts clearly indicates ions irradiated at $10^{19} W/cm^2$ were accelerated higher energy than that of $10^{18} W/cm^2$. Using 3D Monte-carlo code, the energy of accelerated ion is estimated (a)40keV and (b)80keV assuming ion energy distribution as Maxwellian. Both of accelerated ion number are constant at a few times of 10^{13} from the spectral fitting. If the ion is accelerated by the static field, the energy of accelerated ion increases with laser intensity. Therefore the results are consistent with the acceleration mechanism is a static field as shown in previous section.

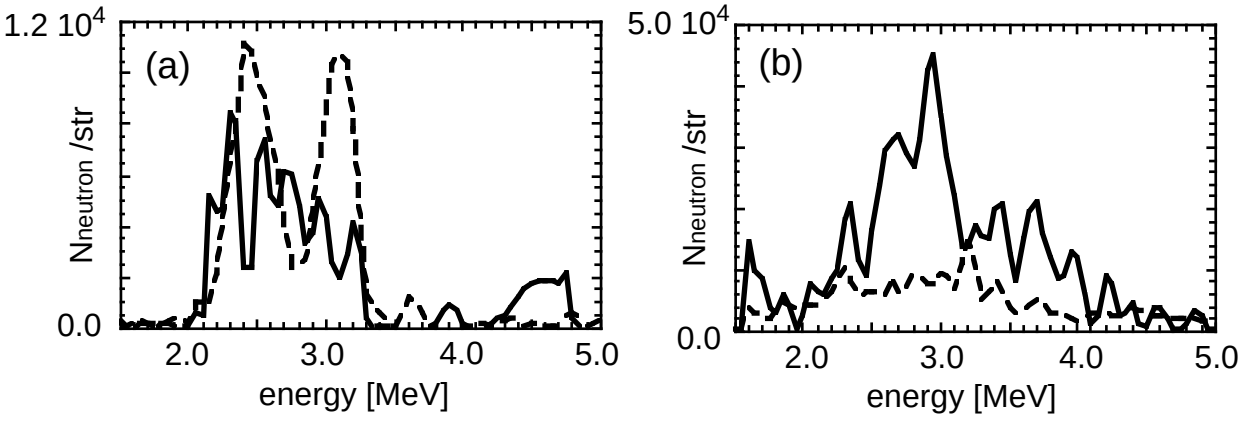

Figure 6.6: Laser intensity dependence at neutron spectra. (a)Neutron spectra at intensities of $10^{18} W/cm^2$ at 43° (solid line) and 87° (dotted line) from the target normal. (b) Neutron spectra at intensities of $10^{19} W/cm^2$. The other figure conditions are as same as Fig. 6.6(a).

The intensity dependence for ion acceleration is also obtained in the results of PIC simulation. Figure 6.7 shows the ion energy distribution at the intensities of $2 \times 10^{18} W/cm^2$

(black solid line) and $2 \times 10^{19} W/cm^2$ (grey solid line), respectively, as the case that Brunel absorption isn't dominant absorption mechanism. Other simulation condition and figure condition are same as Figure 6.5. The ion acceleration energy to both the target inside and vacuum side are increased with the laser intensity. The ion temperature to the target inside is 100keV and total temperature is 45keV at the intensities of $10^{18} W/cm^2$, it is almost a quarter smaller than that of the $10^{19} W/cm^2$.

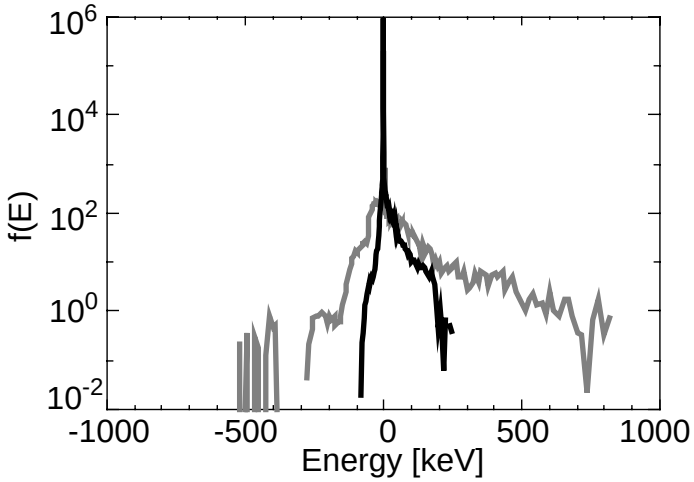

Figure 6.7: The ion energy distribution from the PIC simulation results. The black and grey solid lines are the distribution transverse and parallel to the target surface.

Figure 6.8(a) shows the intensity dependence of detected neutron yield at 93° (square) and 137° (circle) from the target normal. Neutron counts were increased with the laser intensities, the counts at $10^{19} W/cm^2$ was about 50 times larger than that of the $10^{18} W/cm^2$ results in both the view angles. The accelerated ion temperature to the target inside from the spectral fitting of the neutron spectra is shown in Fig. 6.8(b). The line circles and the line squares show the ion temperature in the fitting result of the experimental and the PIC simulation results (at the left axis). From the spectral fitting of the experimental neutron spectra, the accelerated ion momentum is also collimated toward the rear normal of the target surface at any intensities. In the results, the electrostatic potential predominates in the ion acceleration mechanism under these intensities. The solid circles at the right axis are an energy conversion from the laser to the accelerated ions, resulting in a few percentages of the laser energy. The calculated accelerated ion number is almost settled at $10^1 4$, therefore the increase of the counted neutron number depends on only the ion energy.

The ion temperature looks like proportion in the laser intensity. Therefore, the result is consistent with the ion acceleration of the static field acceleration because the electrostatic field is propotional with the laser intensity.

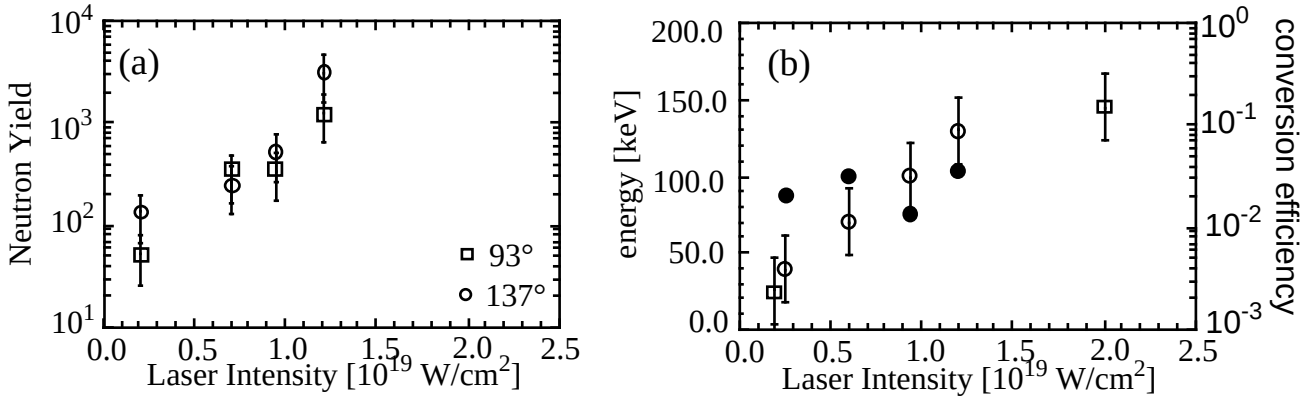

Figure 6.8: Neutron yield and the accelerated ion temperature with the laser intensity. (a) Intensity dependence of neutron yield at 93° (circle) and 137° (square) from the target normal. (b) The intensities of the ion temperature in the fitting results from the experiment (line circle) and PIC simulation result (line square). The energy conversion ratio from the laser to the ions is shown as solid circles.

6.7 Prepulse Level dependence

For the long scale plasma, the ion acceleration is expected to become isotropic resulting from the ponderomotive force in the laser channeling hole. Therefore, as the plasma scale length is enough long, the acceleration direction of ions will be perpendicular to the laser incidence direction. A dependence of a volume of the preplasma on the ion acceleration is obtained to change the prepulse level of the intense laser to generate various scale length plasma.

Using the plasma expansion model, a characterestic scale length is given by [5]

$$L = 0.4 Z_i \left(\frac{m_e}{M_i}\right)^{\frac{1}{2}} v_e t, \tag{6.9}$$

where the v_e is the mean electron velocity oscillated by the laser electric field, m_e the electron rest mass, M_i the mean ion mass and t the time between the prepulse and the main pulse. Figure6.9 shows the dependence of the scale length of the preformed plasma, corresponding the prepulse level, to the neutron yield. The neutron counts ratio is the counts detected at the 23.5° from the rear normal of the target surface devided by the counts at the 66.5°. Indicating the previous section, the neutron counts is asymmetry to the direction and the counts at the target rear normal direction is laser than that of the perpendiculer direction. However the neutron counts at the 23.5° become equivalent or even small than the counts at the 66.5° when the scale length is larger than $15\mu m$.

This reversion of the neutron counts means the change in the ion acceleration direction. Figure6.10 shows the neutron spectra and the ion acceleration momentum as the scale length of the plasmas is over $30\mu m$. The solid lines in Fig.6.10(a) and (b) show the neutron spectra at the (a) 23.5° and (b) 66.5° from the rear normal of the target surface at the intensity of $6\times10^{18} W/cm^2$. There are two prepulses at the 6.5ns and 13ns before, the energy

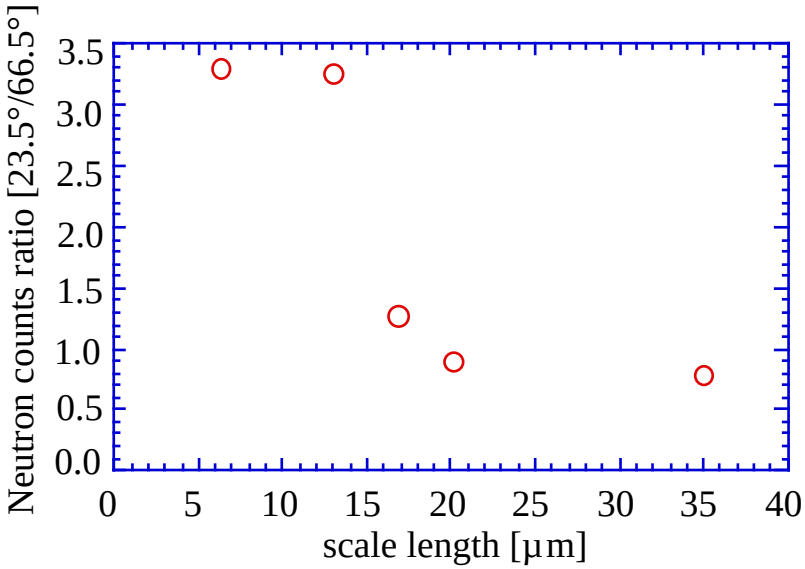

Figure 6.9: The dependence of the scale length of the preformed plasma, corresponding the prepulse level, to the neutron yield. The neutron counts ratio is the counts detected at the 23.5° from the rear normal of the target surface devided by the counts at the 66.5°.

ratio of the two prepulse to the main are both 1.0^{-3}. The peak shift to the heiger energy side from 2.45MeV in the Fig.6.10 is (a) 2.9MeV and (b) 3.0MeV. On the oher hand, that of the lower energy side is (a) 2.3MeV and (b) 2.1MeV. In the result, the ion acceleration is not collimated to the rear normal of the target surface but close to perpendiculer to the laser incidence direction.

The dotted lines in Figs.6.10(a) and (b) show the spectra well-fitted to the experimental results assuming the ion acceleration perpendiculer to the laser incidence direction with Maxwellian energy distribution. Three-dimensional momentum spatial distributions are given as a momentum ratio of Px:Py:Pz=1.4:1:1, where Px corresponding to the target rear side normal, Py the y-axis parallel to the target surface and Pz is the momentum in the direction perpendicularity to the figure. The two dimensional distribution on the x-y plane is shown as a contour plot in Fig.6.10(c). Each line represents $10^{0.2}$ of the ion number in a logarithmic scale. The ion number on the x-y plane is integrated in the z coordinate. It is clear that the ion momentum distribution are weakly collimated perpendiculer target normal direction. The ion energy to the direction corresponding the perpendiculer to the laser incidence is 56keV whereas the energy to the direction paralled to the laser incidence is 28keV.

For the long scale length plasma, the ion acceleration direction changes from the rear normal of the target surface to the perpendicular direction to the laser incidence due to the laser hole-boring. Therefore, it is reasonable that the ion acceleration mechanism is the electrostatic potential by the charge separation between the laser accelerated electrons and the remained ions in the plasma channel. However, there can't except an another possibility of the ion acceleration so-called 'coulombic explosion', which is the isotropic ion acceleration by the coulomb repulsion force among the ramineded ions [16, 17]. In this

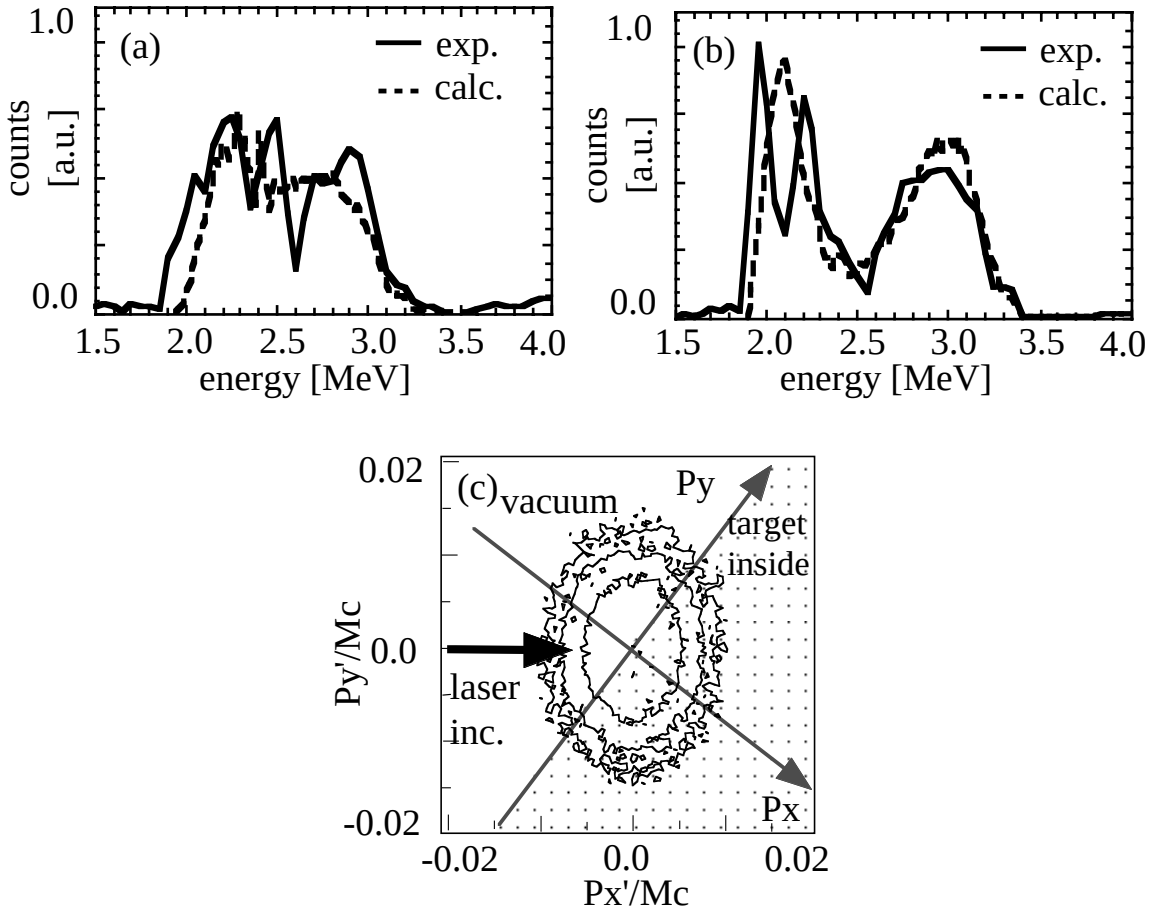

Figure 6.10: The neutron spectra for the large scale length detected at (a) 23.5deg. and (b) 66.5deg. to the rear normal of the target surface. The experimental spectra are shown as black solid lines. The dotted lines represent the calculated spectra from the 3D Monte-carlo code assuming the ion acceleration in the direction of perpendiculer to the target normal, respectively. (c) Contour plot of two-dimensional spatial distribution of the ion momentum obtained by spectral fitting as shown in Figs.6.10(a) and (b). The momentum is normalized by Mc. Each contour line represents $10^{0.2}$ of the ion number in a logarithmic scale.

acceleration, over 50 keV $Ar^{6+} \sim Ar^{8+}$ ions are obtained to irradiate the Ar gas with the density of $4.4 \times 10^{21} cm^{-3}$. The coulombic explosion is proportional to the ion charge, therefore deuteron ions can't accelerate so high energy. In [16, 17], the accelerated energy of the deuteron ions are expected an order of hundred eV. Therefore, the ion acceleration machanism is also the electrostatic potential.

6.8 Summary

I measured the dependences of lthe aser polarization, the laser intensities and the plasma scale length on the neutron spectra to study the ion acceleration mechanisms in ultra-intense laser interactions with solid targets. Comparing the neutron spectra with the 3-D Monte-carlo simulation indicates ion acceleration in the rear normal of the target surface direction at *s*- and *p*- polarization. These results were consistent with the 2D PIC simulation, indicating the ion acceleration with a electrostatic field by the charge separation between the ions and the electrons. The ion acceleration distributions changing the laser intensities and the plasma scale length show that the ions are also accelerated by the electrostatic field.

Reference

[1] A. P. Fews, P. A. Norreys, F. N. Beg, A. R. Bell, A. E. Dangor, C. N. Danson, P. Lee and S. J. Rose, Phys. Rev. Lett., *73*, 1801 (1994).

[2] G. Pretzler, A. Saemann, A. Pukhov, D. Rudolph, T. Schatz, U. Schramm, P. Thirolf, D. Habs, K. Eidmann, G. D. Tsakiris, J. Meyer-ter-Vehn, and K. J. Witte, Phys. Rev. E, **58**, 1165 (1998).

[3] L. Disdier, J-P. Garqonnet, G. Malka, and J-L. Miquel, Phys. Rev. Lett., **82**, 1454 (1999).

[4] M. Tabak, J. Hammer, M. E. Glinsky, W. L. Kruer and S. C. Wilks, Phys. Plasmas, **1**, 1626 (1994).

[5] E. G. Gamaly, Phys. Fluids **5**, 3765 (1993).

[6] M. I. K. Santala et al, Phys. Rev. Lett. **84**, 1459 (2000).

[7] F. Brunel, Phys. Rev. Lett., **59**, 52 (1987).

[8] P. Gibbon and A. R. Bell, Phys. Rev. Lett., **68**, 1535 (1992).

[9] T. Ditmire, J. Zweiback, V. P. Yanovsky, T. E. Cowan, G. Hays and K. B. Wharton, Nature **398**, 489 (1999).

[10] P. A. Norreys et al., Plasma Phys. Control. Fusion **40**, 175 (1998).

[11] J. D. Jackson, *Classical Electrodynamics 2nd. Edition*, chapter 13 (John Wiley & Sons.Inc., New York 1975).

[12] R. J. Howerton, R. E. Dye, M. H. MacGregor, S. T. Perkins, *Index to the LLNL Evaluated Charged-Particle Library*, (Lawrence Livermore National Laboratory, LLNL 1986)

[13] N.Izumi, K.Yamaguchi, T.Yamagajo, T.Nakano, T.Kasai, T.Urano, H.Azechi, S.Nakai and T.Iida, Rev. Scientific Instruments, **70**, 1221 (1999).

[14] Y. Sentoku et al., Phys. Plasmas **6**, 2855 (1999).

[15] Y. Sentoku, K. Mima, S. Kojima and H. Ruhl, Phys. Plasmas **7**, 689 (2000).

[16] M. Lezius, S. Dobosz, D. Normand, and M. Schmidt, Phys. Rev. Lett. , **80**, 261 (1998).

[17] T. Ditmire, J. Zweiback, V. P. Yanovsky, T. E. Cowan, G. Hays, and K. B. Wharton, Nature, **398**, 489 (1999).

Chapter 7

Nuclear Physics in ultra intense laser interactions

7.1 Introduction

Ultra-intense laser-plasma interactions generate an energetic electrons and ions with energies over MeV . These particles are generated in the solid or more high dense compared with the ordinary particle accelerator such as the linac and synchrotron. Therefore, a generated particle through the nuclear reaction is also created in high energy density, resulting in a possibility to study nuclear physics in ultra-intense laser interactions. In this section, I describe the experiment of D-Li and D-B nuclear fusion reactions generate an unstable nucleus. At first, the ion acceleration using Li and B is described to study a high energy part of the ions. Feasibility is also discussed of study an reaction of the unstable nucleus using the Li-D and B-D reactions.

7.2 Nuclear fusion reaction using Li and B

In previous chapter6, I show the accelerated ion distribution from the neutron spectroscopy using the D-D fusion reaction. However, the cross section of the D-D fusion reaction is almost constant from 1MeV to 10MeV of the incident deuteron energy. Furthermore, the population of the high energy part in the ion distribution is small, then the distribution profile in the high energy part may be not precious. Actually, the accelerated electron distribution is consisted of the two Maxwellian distribution, mainly low energy part and additional high energy part resulting from[1]. To measure the high energy part of the accelerated ion distribution profile, I utilized a neutron spectroscopy from the D-Li and D-B fusion reaction. The cross section of the neutron generated D-Li and D-B reaction are both increased from ∼1MeV as shown in Figure7.1

The cross section of the Li-D reaction become same level with the D-D fusion reaction near the $3MeV$ and that of the D-B has a peak near the 0.5 MeV of which cross section is the half of that of the D-D reaction. However, if the energy of the generated neutron from the Li-D and B-D reaction is the same range compared with the D-D neutron, the neutron spectroscopy become different. Figure7.2 shows the neutron energy detected at the 0° and

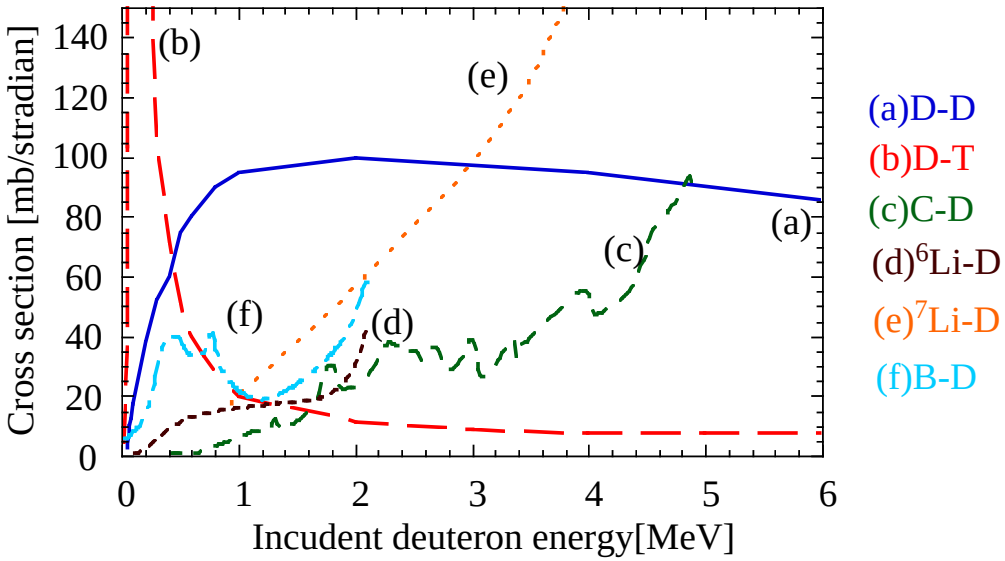

Figure 7.1: The cross section of the neutron generated (a)D-D (d[d,n]^{3}He), (b)D-T (d[t,n]^{4}He), (c)D-C (^{12}C[d,n]^{13}N), (d)D-^{7}Li (^{7}L[d,n]^{8}Be), (e)D-^{6}Li (^{6}L[d,n]^{7}Be) and (f)D-^{10}B (^{10}B[d,n]^{1}1C)fusion reaction with the initial deuteron energy.

180° from the ion acceleration direction.

The neutron energy of the Li-D is about 3MeV (^{6}Li-D) and 11MeV (^{7}Li-D). The neutron energy of the B-D is about 6MeV (^{10}B-D) and 11MeV (^{11}B-D). If the deuteron energy is over 5MeV, the neutron generated from the D-D reaction and ^{10}B-D reaction can't distinguished each other.

7.2.1 Experiment

The experiment to measure the accelerated ion distribution from the neutron spectroscopy using the D-Li and D-B fusion reaction was performed at the GMII ultra-intense short-pulse laser system in the Institute of Laser Engineering. The laser intensity was about 10^{18}W/cm^2 with the pulse duration of 600-700fs and spot size of 30μm.

Figure 7.3 shows the neutron spectra generated by D-B reaction detected at (a) the 86.5° and (b) the 145°.

The neutron spectra near the 2.45MeV shows the D-D fusion neutron. On the other hand, the neutron signal near the 6.0MeV can be the ^{10}B-D neutron. The fusion reaction number is estimated from the neutron counts of the B-D reaction, resulting in 2×10^5 of the neutron counts. Therefore, the unstable nucleus of ^{11}C was generated in 2×10^5 as same as the neutron number.

On the other hand, the neutron from Li-D fusion reaction was close to noise level. The released neutron energy in Li-D reaction is higher than that of the ^{10}B-D neutron, therefore, the noise level increase with the neutron energy in T.O.F method to be difficult to distinguish the noise and the signal in this experimental setup. The upper limit of the Li-D neutron is 7×10^4. Comparing the cross section between B-D and Li-D, the Li-D

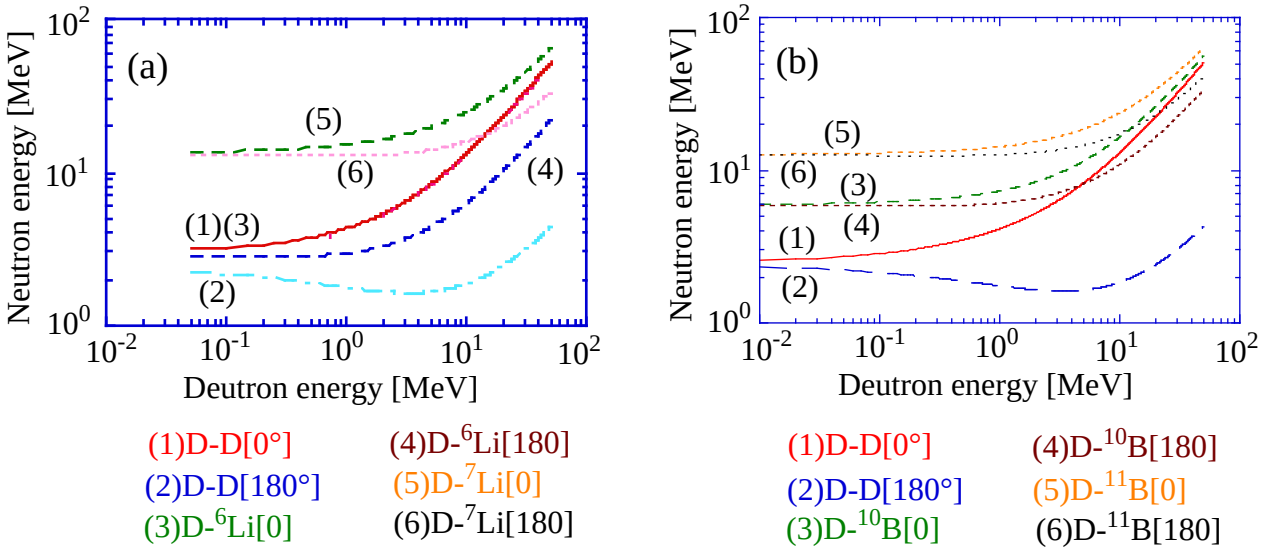

Figure 7.2: The neutron energy from (a) Li-D reaction and (b) B-D reaction at the 0° and 180° from the ion acceleration direction.

neutron can be expected also in 10^5 level.

The density of the reaction nucleus from the B-D fusion reaction is estimated considering the range of the accelerated deuteron, resulting in about $4\times10^{15}\mathrm{cm}^{-3}$.

7.3 Generation of Perfectly-Ionization unstable EC nuclei

In this section, the possibility of study for unstable nucleus resulting from the Li-D fusion reaction in ultra-intense laser-plasma interactions. ^{6}Li-D reactions is one of the chain reaction in sun. This reaction generate an unstable nucleus of ^{7}Be with a neutron. The ^{7}Be is well known in decay to ^{7}Li by the electron capture(unstable EC) on the orbit of the atom. However, under perfectly ionized state, for example in the laser generated plasma, these unstable nucleus are considered to be difficult to decay. Furthermore, the interaction with other hadron or lepton such as free electrons has not studied in detail yet. Especially, the ^{7}Be is considered to be perfectly ionized inner the sun, therefore, it is difficult to investigate the perfectly ionized unstable nucleus in the laboratory [2].

However, there is possibility to generate the unstable nucleus in high energy density due to the high energy density particles in ultra-intense laser-plasma interactions as shown in previsous chapter. Furthermore, such particle interacts with laser created plasma which is high energy and density can be reproduce the nuclear reaction inner the sun.

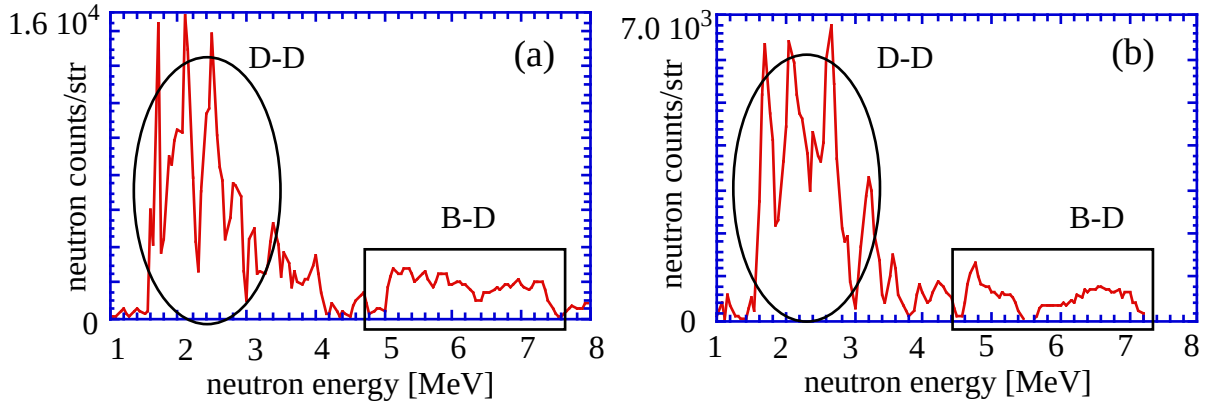

Figure 7.3: The neutron spectra generated from D-B fusion reaction (∼6MeV) with D-D reaction (∼2.45MeV). (a) The spectrum at the 86.5°. (b) The spectrum at the 145°.

7.4 Summary

Ultra-intense laser-plasma interactions generate an energetic electrons and ions with energies over MeV . The neutron from D-B nuclear fusion reactions were observed at 2×10^5, indicating in generation of same number of the unstable nucleus ^{11}C. The density of the nucleus is estimated considering the range of the accelerated ions in chapter6, resulting in 4×10^{15}cm^{-3}. Feasibility is also discussed of study an reaction of the unstable nucleus using the Li-D and B-D fusion reactions.

Reference

[1] A. B. Langdon, Phy. Rev. Lett. **44**, 575 (1980).

[2] C. E. Rolfs and W. S. Rodney, *Caudrons in the Cosmos*, The university fo chicago press (1988).

Chapter 8

Summary

I summarize and discuss the results obtained through the studies in this thesis. I have studied the generation and transport of high energy density particles to understand the ultra-intense laser plasma interactions.

In the chapter 2, I have developed an ultra-intense short-pulse CPA laser system using Ti:Sapphire oscillator coupled with Nd:glass amplifiers. To optimize the creation of chirped pulse, I developed a laser propagation simulation with the spectral response of the GEKKO-MII Nd:glass system. I also calculated the influence of the self-phase modulation on the compressed pulse shape and laser focusing intensity. On the basis of the results, 35TW/0.5ps laser light was obtained after the 16J amplification, resulting in the intensity of $10^{19} W/cm^2$ with a spot diameter of $20\mu m$.

In the chapter 3, I have demonstrated pulse shaping by spectral control using a spatial modulation filter at the glass amplifiers system coupled with the Ti:Sapphire front end. The spectral control was applied to shorten the pulse duration from over 500fs to 300fs at an energy of near 20J corresponding to 70TW with the glass amplifier system in the experiment. Control of the pedestal and the prepulse by spectral control of a chirped pulse were also performed taking account of the system spectral response.

In the chapter 4, I studied the generation and transport of the high energy density electrons. Obtained are the dependence of the generation of the high energy density electrons on the laser incident angle dependence and prepulse level. The dependence is caused by absorption mechanism such as brunel absorption. The heating processes are also influenced by the absorption

In the chapter 5, I have shown here is the guided compression to explore some of the physics issues of hot electron heating and transport in the compressed plasma, while avoiding the difficulties associated the stability of the channel formation pulse. I have demonstrated that the guided foil remains stable during the compression and that good agreement is obtained with two-dimensional hydrodynamics simulations. An integrated conical compression experiment has confirmed, resulting in the heated temperature of about 500eV in the compressed plasma with the density of $3 \sim 4 g cm^{-3}$.

In the chapter 6, I measured laser polarization, intensities and prepulse level dependencies of fusion neutrons to study the ion acceleration mechanisms in ultra-intense laser interactions with solid targets. Comparing the neutron spectra with the 3-D Monte-carlo simulation indicates ion acceleration in the rear target normal direction at any polarization

or incident angles. These results were consistent with the 2D PIC simulation, indicating the ion acceleration with a static electric field by charge separation between ions and electrons. This acceleration mechanism is reinforced from the intensity dependence and prepulse dependence of the ion acceleration with the neutron spectroscopy.

In the chapter 7, I demonstrated one of applications in high energy density particles generated in ultra-intense laser interactions by ion acceleration in D-Li or D-B nuclear fusion reaction to generate density unstable nucleus. I shown the neutron spectra which have a possibility of generating from the D-B fusion reaction. From a comparing the neutron yield between the D-D neutron and D-B neutron, a reaction number of the D-B is 2×10^4.

The results in this thesis will some contribute on the understanding in ultra-intense laser-plasma interactions and realizing the fast ignitor.

Appendix A

Fast Ignitor

A concept of fusion using laser was designed in 1972 by J. Nuckolls et al. [1]. The design of the laser fusion is called a " Inertial confinement fusion (ICF) " from enclosure a fuel plasma utilizing inertial force, against magnetically confinement fusion (MCF) which enclose plasma by the magnetic field. Figure A.1 shows the story of the ICF: (a) the laser beams irradiate spherical target symmetry. (b) After the laser irradiation, a shock wave generated by a reaction force of the plasma ablation transmits toward a center of the target (implosion). (c) The shock wave increases a temperature at the target center and then stimulates to ignition (ignition). In this model, the fuel is consisted to hot spark plasma and surrounding high dense, low temperature main fuel. The two plasma regions are equilibrium in pressure and isobaric. However, ununiformity of the sperical symmetry in the laser irradiation prompts a growth of the instability in the implosion plasmas and troubled to formation of the hot spot in the plasma center.

On the other hand, with recent progress of ultra powerful lasers, the fast ignitor concept was considered in 1994 by M. Tabak et al [2]. The fast ignitor is purposed to relax the implosion instability due to additional heating of the hot spot in the plasma by energetic particles generated in laser-plasma interactions. Figure A.2 shows the story of the fast ignitor: (a) During the plasma implosion, ultra-intense laser irradiates the plasma and then push out underdense plasma (channeling). (b) Other ultra-intense laser goes into the plasma channel and interacts with the critical dense plasma. The interactions generate energetic particles to heat up the core fuel plasma (additional heating). (c) The hot electrons increase a temperature at the target center and then stimulates to ignition (ignition). In this method, the drive energy required to assemble the fuel to high density is significantly reduced and the energy gain of the target is potentially much higher for the isochoric compared with the isobaric scheme mentioned above. Equally significant, the symmetry requirements needed to assemble the fuel to high density can also be considerably relaxed, principally because the stagnation pressure is significantly lower.

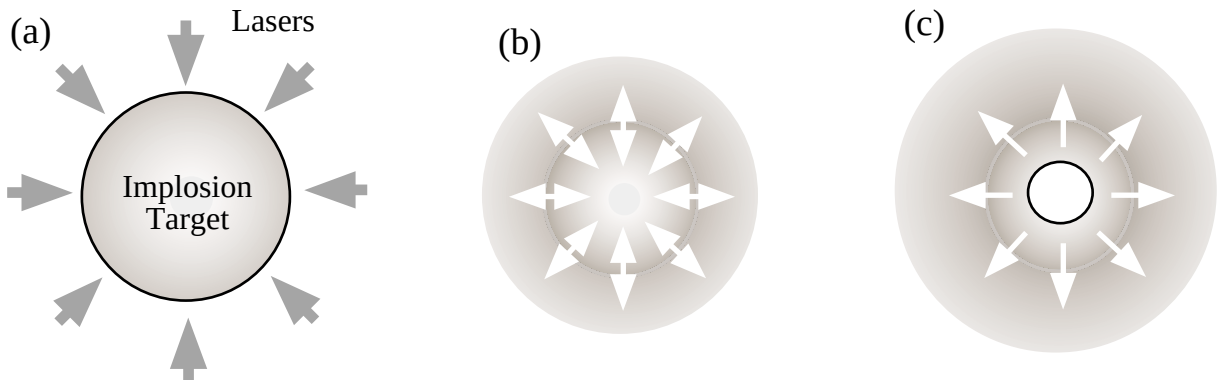

Figure A.1: Inertial confinement fusion scheme. (a) Symmetrical irradiation. (b) Implosion. (c) Ignition.

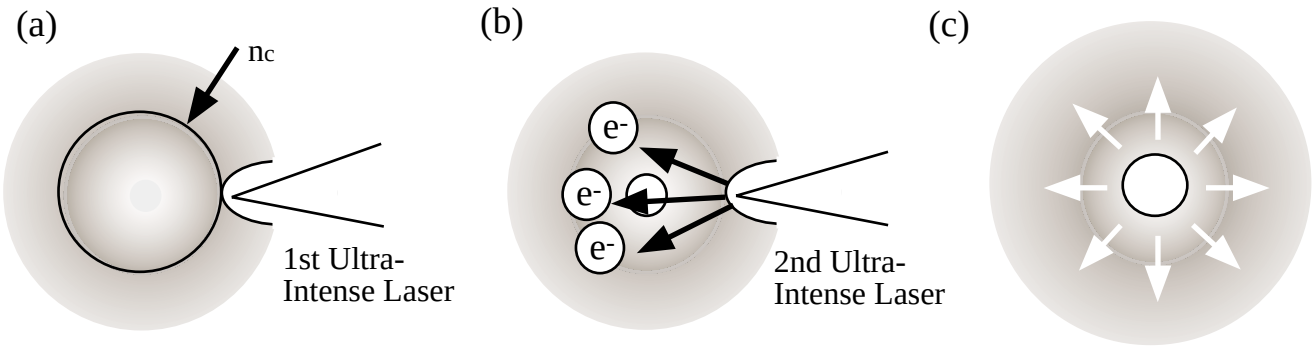

Figure A.2: fast ignitor scheme. (a) Laser channeling. (b) Hot electron generation. (c) Ignition.

Reference

[1] J. Nuckolls et al., Nature **239**, 139 (1972).

[2] M. Tabak et al., Phys. Plasma **1**, 1626 (1994).

Appendix B

Electron acceleration in ultra-intense laser-plasma interactions

B.1 Electron acceleration mechanism

As an acceleration mechanism of the electron in ultra-intense laser-plasma interactions, J×B acceleration [2] and Brunel-type absorption [1] is considered.

In the J×B acceleration, the electron is accelerated by a lorenz force by laser magnetic field and the quiver electron current. The J×B acceleration is appeared by the nonlinear effect in the interactions of electron and electromagnetic wave. The motion equation of the electron without the relativesitic effect is given

$$m\frac{dv}{dt} = -e[\mathbf{E} + v \times \mathbf{B}]. \tag{B.1}$$

Here, linear polarized electric field is given as $\mathbf{E} = E_L(x)(\sin\omega_L t)\hat{y}$, the ponderomotive force is given from equationB.1 as

$$f_p = -\frac{m}{4}\frac{\partial}{\partial x}v_0^2(x)(1-\cos 2\omega_L t)\hat{x}. \tag{B.2}$$

The first term of the right side of the equation shows a light pressure. The secound term induce a electron oscillation. If the light irradiate the steep gradient plasma, oscillated electrons will go around between high dense plasma and vacuum. However, the light can't propagate into the high density plasma if the density is over the critical density. Therefore, when the electron reinter the plasma from the vacuum, the electrons propagate into the plasma without the oscillation by the laser electric field. The accelerated direction of the electrons are expected to the laser propagation direction.

On the other hand, the p-polarized light irradiated a steep gradient plasma, the brunel absorption become predominated in the laser absorption. In this acceleration, the electrons are oscillated by the electric field between the plasma and the vacuum because the electric field of the p-polarized light is perpendicular to the target normal at the turning point of the light. Therefore, the acceleration direction of the electron is considered the target normal direction. The absrobed rate is estimated by the Brunel[1], given

$$f_{brunel} = (\eta/2\pi)(e/m\omega c\cos\theta)\frac{E_0^3}{E_L^2}, \tag{B.3}$$

where E_L is the incident laser field, $E_0 = \xi E_L \sin\theta$ is the total incident and reflected field, 1¡ξ¡2 accounts for the complex reflectivity, and Brunel found numerically that $\eta = 1.75(1 + 2v_{th}/v_{osc})$ $(v_{th}0(2kT_e/m)^1/2)$.

B.2 Electron acceleration direction

The acceleration direction of electron can be changed with the laser polarization due to the difference of the acceleration mechanism. The acceleration direction was investigated to detect the visible-ray emission from the target heating at the rear face through the electron propagation. FigureB.1 shows the difference of the acceleration direction of the electrons.

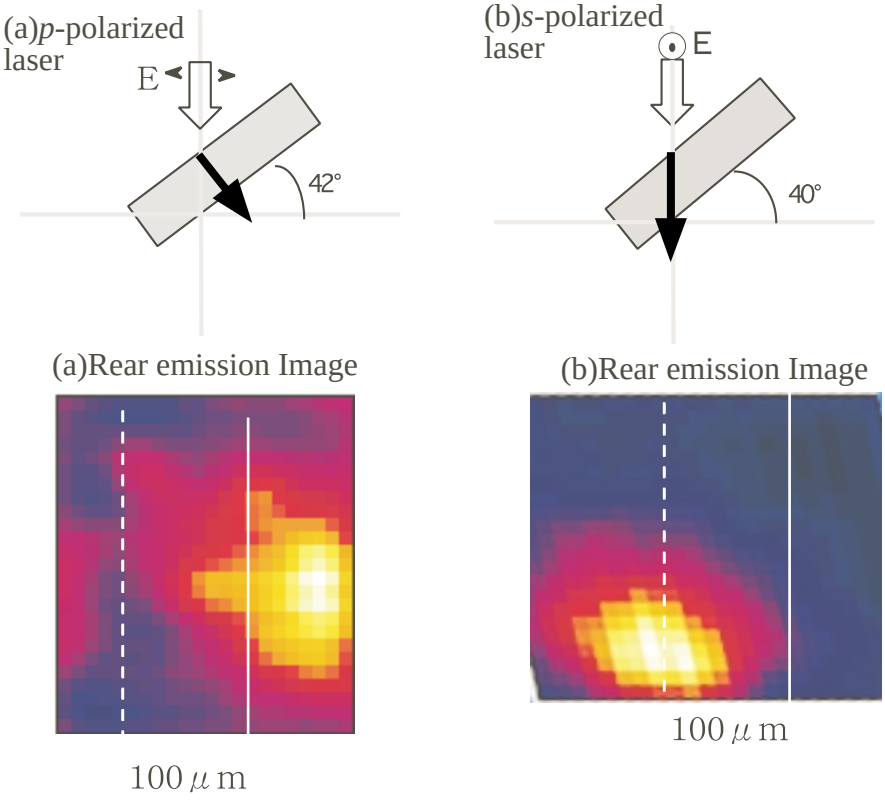

Figure B.1: Electron accelerated direction by the p- and s-polarized laser light. The images are 2D visible-ray emission due to a plasma heating of the electrons detected at the rear target side. The solid line shows the target center line and the dotted line shows the laser propagation position at the rear surface.

The images are 2D visible-ray emission due to a plasma heating of the electrons detected at the rear target side by the HISAC system as mentioned in chapter4. The solid line shows the target center line and the dotted line shows the laser propagation position at the rear surface. In the p-polarized light, the emission at the rear face is close to the target center

at the rear surface. On the other hand, in the *s*-polarized light, the accelerated electrons emit the laser propagation direction at the rear surface of the target. In the results, the electron is mainly accelerated to the target normal direction by the *p*-polarized light due to the brunel absorption and the laser propagation direction by the *s*-polarized light due to the J×B acceleration in the ultra-intense laser-plasma interactions.

Reference

[1] F. Brunel, Phys. Rev. Lett. **59**, 52 (1987).

[2] E. G. Gamaly, Phys. Fluids **5**, 3765 (1993).

Acknowledgments

The author would like to express gratitude to Professor H. Azechi for his excellent guidance throughout his research at the Course of Science and the Institute of Laser Engineering, Osaka University, Osaka, Japan.

He wishes to thank to former-Professor Y. Kato , the director of the Advanced Photon Research Center, at Kansai Research Establishment, Japan Atomic Energy Research Institute(JAERI), who strongly impressed on me the interest and mission of this study.

He would like to acknowledge Professor T. Yamanaka, the director of the Institute of Laser Engineering (ILE) for the encouragement of this study.

He is deeply grateful to Lecture R. Kodama at the Institute of Laser Engineering, for his invaluable advice and continuous encouragement throughout this investigation.

He is indebted to Professor S. Kinoshita at the Course of Science, Professor K. Mima and Associate Professor Y. Kitagawa at the Associated Course of Science.

His grateful thanks are to Professor H. Takabe, Associate Professors K. A. Tanaka, H. Fujita, T. Norimatsu, Associate Researcher K. Nagai, Dr. E. Yoshida, Dr. N. Izumi, Dr. Y. Sentoku, Dr. K. Takahashi(JAERI), Dr. M. Heya and all the members of the Mt, Target fabrication, Laser operation and Computer groups.

He would like to thank to Associate Professor. P. A. Norreys (Rutherford Appleton Laboratory, U.K.), Lecture N. C. Woolsey (Univ. York, U.K.), Lecture K. Krushelnick, Dr. M. Zepf, Mr. M. Santala(Imperial college, Univ. London, U.K.).

He would like to specially acknowledge the fellow at ILE, K. Sawai, K. Suzuki, S. Nakata, T. Kamino, J. Kou, M. Mori, T. Koase, H. Setoguchi, T. Miyakoshi, T. Iwatani, H. Toyama, M. Tanpo, F. Otani, Y. Murakami and Y. Miyake.

He is grateful to everyone who provided assistance during various stages of this research.

Publication Record

Paper

1. **H. Habara**, R. Kodama, Y. Sentoku, N. zumi, Y. Kitagawa, K. A. Tanaka, K. Mima and T. Yamanaka, "*Study of Ion Acceleration in Ultra-intense Laser-plasma Interactions with Neutron Spectroscopy*", To be accepted to Phys. Rev. Lett.

2. **H. Habara**, R. Kodama, M. Mori, K. Sawai, K. Suzuki, C. Kamino, K. Kitagawa and T. Yamanaka, "*Pulse Shaping with Spectral Control of a Chirped Pulse in a Glass Amplifier System*", To be submitted for Applied Optics B.

3. **H. Habara**, R. Kodama, N. Izumi, Y. Sentoku, K. A. Tanaka, Y. Kitagawa, K. Mima and T. Yamanaka, "*Fast Ion Generation in Ultra Intense Laser Interactions with Plasmas*", To be published to proceedings of SPIE, 1999.

4. P. A. Norryes, R. Allot, R. J. Clarke, D. Neely, S. J. Rose, M. Zepf, M. Santala, A. R. Bell, K. Krushelnick, A. E. Dangor, N. C. Woolsey, R. G. Evans, **H. Habara**, and R. Kodama, "*Guided Conical Compression Experiments Relevant to the Fast Ignitor Scheme*", Submitted to Plasma Phys. Controlled Fusion.

5. Y. Kitagawa, R. Kodama, K. Takahashi, M. Mori, M. Iwata, S. Tuji, K. Suzuki, K. Sawai, K. Hamada, K. A. Tanaka, T. Fujita, T. Kanabe, H. Takabe, **H. Habara**, Y. Kato and K. Mima, "*30-TW laser plasma interactions at ILE, Osaka*", Fusion Engineering and Design 44, 261(1998).

6. M. Mori, K. Kitagawa, R. Kodama, **H. Habara**, M.I wata, S. Tuji, K. Suzuki, K. Sawai, K. A. Tanaka, Y. Kato and K. Mima, "*Ultra intense glass laser system and laser-plasma interactions*", Nuclear Instruments and Methods in Physics research A 410, 36'(1998).

7. K. A. Tanaka, R. Kodama, N. Izumi, K. Takahashi, M. Heya, H. Fujita, Y. Kato, Y. Kitagawa, K. Mima, N. Miyanaga, T. Norimatsu, Y. Sentoku, A. Sunahara, H. Takabe,T. Yamanaka, T. Koase, T. Iwatani, F. Ohtani, T. MIyakoshi, **H. Habara**, M. Tanpo, S. Tohyama, F. A. Weber, T. W. Barbee. Jr., and L. B. DaSilva, "*Studies of ultra-intense laser plamsa interactions for fast ignitor*", Bull. Amer. Phys. 44 , 93 (1999). will also appear in Phys. Plasmas.

8. **H. Habara**, R. Kodama, K. Sawai, K. Suzuki, M. Mori, S. Tsuji, K. Hamada, M. Iwata, K. Tanaka1, Y. Kitagawa, H. Fujita, Y. Kato, "*Development of a Short Pulse Intense Laser with a Ti:Sapphire Laser Frontend system coupled to Nd:Glass Amplifiers*", Proceedings of Opt-quamtum device research conferernce, Electronics society, OQD-97-24, 24 (1997).

Conference Presentations

1. **H. Habara**, R. Kodama, N. Izumi, K. Takahashi, M. Mori, Plasma measurement group, GMII and PWM laser group, Target group, K. A. Tanaka, K. Kitagawa, "*Neutron Spectroscopy for Fast Ion Generation in Ultra Intense Short Pulse Laser Interactions with a Solid Target*", Asia Science seminar on High-Power Laser Matter Interactions, Institute of Laser Engineering of Osaka University and Japan Society for the Promotion of Science (JSPS), Osaka, 7-17th February 1999.

2. **H. Habara**, R. Kodama, N. Izumi, Y. Sentoku, K. A. Tanaka, Y. Kitagawa, K. Mima and T. Yamanaka, "*Neutron Spectroscopy for Study of Ion Acceleration in Ultra Intense Laser Interactions*", 29th Annual Anomalous Absorption Conference, Pacific Grove, California, 14-18th June 1999.

3. P. A. Norreys, **H. Habara**, et al., "*Relativistic Laser-Plasmas and Guided Conical Compression Experiments Relevant to the Fast Ignitor Scheme for ICF*", The 1st International Conference, Inertial Fusion Sciences and Applications (IFSA), University Bordeaux 1, Bordeaux, France, 12-17th September 1999.

4. K. A. Tanaka, **H. Habara**, et al., "*Study of Relativistic Laser Plasmas Related to Fast Ignition at Osaka*", The 1st International Conference, Inertial Fusion Sciences and Applications (IFSA), University Bordeaux 1, Bordeaux, France, 12-17th September 1999.

5. **H. Habara**, R. Kodama, N. Izumi, Y. Sentoku, K. A. Tanaka, Y. Kitagawa, K. Mima and T. Yamanaka, "*Fast Ion Generation in Ultra Intense Laser Interactions with Plasmas*", International Forum on Advanced High Power Lasers and Applications (AHPLA), The International Society for Optical Engineering(SPIE), Osaka University, Japan, 1-5th November 1999.

6. **H. Habara**, R. Kodama, K. Sawai, H. Katuyama, M. Mori, K. Suzuki, Y. Kitagawa and Y. Kato, "*Development of short pulse intense laser using Ti:Sapphire laser coupled with Nd:glass amplifier*", The 43rd Spring Meeting, 1998, The Japan Society of Applied Physics and Related Societies, Toyo University, Tokyo, 1996.

7. **H. Habara**, R. Kodama, K. Sawai, M. Mori, S. Tuji, K. Suzuki, K. Habara, Y. Kitagawa, Y. Kato, "*Development of short pulse intense laser using Ti:Sapphire laser cou-*

pled with Nd:glass amplifier(2)", The 57th Autumn Meeting, 1996, The Japan Society of Applied Physics and Related Societies, Kyusyu Sangyou University, Fukuoka, 1996.

8. **H. Habara**, S. Tsuji, R. Kodama, M. Mori, M. Iwata, k. Suzuki, K. Hamada, K. Sawai, K. A. Tanaka, K. Kitagawa and Y. Kato, "*Short pulse intense laser interactions I: energetic particle measurement*", The 57th Annual Meeting, The Physical Society of Japan, Meijou University, Nagoya, 1997.

9. **H. Habara**, R. Kodama, M. Mori, K. Sawai, K. Suzuki, S. Nakata, K. Kitagawa and Y. Kato, "*Pulse shaping with spectral control in short pulse intense laser*", The 58th Autumn Meeting, 1997, The Japan Society of Applied Physics and Related Societies, Akita University, Akita, 1997.

10. **H. Habara**, R. Kodama, M. Mori, K. Sawai, K. Suzuki, S. Nakata, K. Kitagawa and Y. Kato, "*Pulse shaping with spectral control in short pulse intense laser (II)*", The 45th Spring Meeting, 1998, The Japan Society of Applied Physics and Related Societies, Tokyo Technology University, Tokyo, 1998.

11. **H. Habara**, R. Kodama, N. Izumi, M. Mori, T. Sonomoto, T. Matsushita, H. Asatsu, T. Koase, Y. Sentoku, K. A. Tanaka, Y. Kitagawa and K. Mima, "*Fundamental study for Fast Ignitor using 60TW short pulse laser:Energetic particle measurement*", 1998 Autumn Meeting, The Physical Society of Japan, Ryukyu university, Okinawa, 1998.

12. **H. Habara**, R. Kodama, N. Izumi, Y. Sentoku, K. A. Tanaka, Y. Kitagawa, T. Yamanaka and K. Mima, "*Ultra intense laser plasma interactions relevant to Fast Ignitor (7)Neutron spectroscopy in Sub ps laser plasma interaction*", The 59th Annual Meeting, The Physical Society of Japan, Hiroshima University, Hiroshima, 1999.

13. **H. Habara**, R. Kodama, N. Izumi, Y. Sentoku, K. A. Tanaka, Y. Kitagawa, K. Mima and T. Yamanaka, "*Fundamental study for Fast Ignitor (7)Neutron spectroscopy*", 1999 Autumn Meeting, The Physical Society of Japan, Iwate University, Iwate, 1999.

14. **H. Habara**, R. Kodama, H. Setoguchi, T. Koase, H. Toyama, Y. Sentoku, M. Mori, K. Sawai, K. Suzuki, C. Kamino, K. A. Tanaka, Y. Kitagawa, K. Mima and T. Yamanaka, "*Jet Formation inside a solid target in an ultra intense laser interaction*", The 16th Annual Meeting, The Japan Society of Plasma Science and Nuclear Fusion Research, Miyagi Prefectural Hall, Miyagi, 1999.